

MODELLING OF ELECTROMAGNETIC SCATTERING AT INFRARED WAVELENGTHS BY PRISTINE ICE CRYSTALS

Jawad Shaker

Supervised by: Dr. David Bebbington



A thesis submitted for the degree of Doctor of Philosophy
Department of Computer Science and Electronic Engineering
University of Essex

Date of Submission: Tuesday 17th September, 2019

Dedication

To my family and friends who supported me throughout this PhD journey.

Abstract

Cirrus clouds have a large effect on the atmospheric system and radiative budget of earth as they have a huge influence in all scales of weather processes and climate. Cirrus clouds are composed of non-spherical ice crystals with various shapes and cover about 30%-40% globally. The appropriate geometric models (applied mathematics and computational geometry) and incident coordinate systems determine the shapes of ice crystals [1]. The shapes include but not limited to: hollow columns, dendrites, bullet rosettes and capped columns. The scattering solution however in the infrared's part of the spectrum is a complex problem. There are established methods that have been used to solve scattering methods such as Mie, T-matrix and Rayleigh theories. These methods are not efficient at infrared wavelengths due to size parameter, which typically can be in order of 100 or more that leads to intensive computation. In this work, a new approach based on physical optics is presented in which the scattering by smooth prismatic dielectric ice crystals which are electrically large is evaluated. In this method, the total scattered amplitude in any direction can be evaluated by application of the reaction theorem to a volume interval in principle from a knowledge of the internal field distribution. This integral in turn can be converted to an integral over the equivalent surface current distribution. The method enables the evaluation of the total surface field. The scattered field solution of the proposed physical optics method (PO) has been compared with ray launching geometrical optics (RL-GO). Overall, the proposed method shows a good agreement when the size of the scatterer is large compared to the wavelength. The proposed method has a good potential to be applied for ice crystals with rough surface structure.

Acknowledgements

First and foremost, I would like to express my sincere gratitude to almighty God for giving me a chance to do a PhD and complete this PhD thesis. I would like to thank everyone who helped to complete this thesis.

A special gratitude goes to my parents, Alaa Shaker and Suzan Khayyat, for helping me financially and keeping me motivated to finish my PhD journey. Also, I am thankful for having wonderful siblings: Abdulrahman, Jawan and Jilan.

I would like to express a deep gratitude to my supervisor, Dr. David Bebbington, who gave me the chance to start this journey and introduced me to the field of electromagnetic wave propagation and scattering. He supported me tremendously and unconditionally offered me his wealth of experience, and outstanding guidance at all stages of this work. I am very grateful that he accepted me as his PhD student. I believe that without him my thesis would have been very different.

I greatly acknowledge the financial support from my sponsor throughout all my academic studies starting from the Bachelors until the PhD.

I am thankful to all of my colleagues in the School of Computer Science and Electronic Engineering for the enjoyable atmosphere and for their help.

Acronyms and abbreviations

CZT- Chirp-Z Transform

DDA- Discrete Dipole Approximation

EM - Electromagnetic

EMTs - Effective Medium Theories

FDTD - Finite Difference Time Domain

FEM - Finite Element Method

FFT - Fast Fourier Transform

GO - Geometrical Optics

GTD - Geometrical Theory of Diffraction

IN - Ice Nucleating

IWC - Ice Water Content

MoM - Method of Moment

PO - Physical Optics

PSD - Particle Size Distribution

RL-GO - Ray Launching Geometrical Optics

RTDF - Ray Tracing with Diffraction of Facets

TE - Transverse Electric

TM - Transverse Magnetic

UTD - Uniform Theory of Diffraction

Contents

Dedication	i
Abstract	i
Acknowledgements	ii
1 Introduction	1
1.1 Motivation	5
1.2 Thesis outline	6
2 Background and literature review	9
2.1 Cirrus clouds	9
2.2 Microphysical and macrophysical properties and formation	11
2.3 Single ice crystal properties	13
2.4 The cirrus clouds problem in climate research	18
2.5 Dielectric properties of ice crystals	21
2.6 Fraunhofer Diffraction	25
2.6.1 Fraunhofer diffraction equation	26
2.6.2 Examples of Fraunhofer diffraction	30
2.7 Fresnel Equations of Reflections	33
2.8 Geometrical and Uniform Theories of Diffraction	35

2.8.1	The Geometrical Theory of Diffraction	35
2.8.2	Uniform Theory of Diffraction	36
2.9	Physical optics	37
2.9.1	Physical optics approximation	38
2.9.2	Uniform asymptotic physical optics method (UAPO)	41
2.9.3	UAPO solution for diffraction by dielectric wedge	41
2.10	The Reaction Theorem	46
3	Physical optics and ray-tracing approach to scattering by 2D dielectric wedge	48
3.1	Introduction	48
3.1.1	Internal diffractive effects	51
3.1.2	Internal field reconstruction	51
3.1.3	The internal diffractive effects in a lossy medium	53
3.2	Implementation and results of physical optics method	54
3.2.1	Results of the implementation	56
3.3	Ray-tracing approach to scattering by a wedge	68
4	2D physical optics and ray-tracing approach to scattering by a prism	72
4.1	Methodology and implementation	72
4.2	Results	79
4.2.1	Lossy prism analysis	82
4.3	Green's function method for scattering by a dielectric prism	84
4.3.1	Implementation of Green's function method for scattering by a dielectric prism	86

4.3.2	Results	89
4.3.3	Comparisons between Physical Optics and Green's Function results	92
5	Ray-tracing and physical optics approach to scattering by a 2D Hexagonal form ice crystal	94
5.1	Methodology	94
5.2	Results	102
6	Physical optics and ray-tracing method for scattering by 3D ice crystals	106
6.1	Introduction to the method	106
6.1.1	Equation of a plane passing through three points	106
6.1.2	Cartesian to polar coordinate conversion	109
6.1.3	The intersection of a plane with a line	110
6.1.4	Fast rotation by orthogonal shearing	111
6.2	Methodology of 3D shape construction and ray-tracing	116
6.2.1	Facets construction by rotation matrix	116
6.2.2	Refraction and reflection	120
6.2.3	High-level explanation of the PO method	122
6.2.4	Flowchart of the 3D ray-tracing and PO by dielectric prism	126
6.2.5	3D ray-tracing and physical optics by a dielectric prism algorithm .	129
6.2.6	Results	133
6.3	3D ray-tracing and physical optics method for scattering by dielectric hexagonal prism ice crystal	145
6.3.1	Flowchart	145
6.3.2	Algorithm	148

6.3.3	Results	152
6.4	3D ray-tracing and physical optics method for scattering by bullet shape ice crystals	157
6.4.1	Flowchart	157
6.4.2	Results	159
6.5	Transformation of the volume integral to surface integral form	162
6.6	Scattering by a hexagonal prism results and comparisons	170
6.6.1	Problem statement	170
6.6.2	Solution approach	171
6.6.3	Numerical results	173
7	Conclusion and future work	184
8	Appendices	205
8.1	Rotational matrix facet construction	205
8.2	PO results for 3D triangular prism	223
8.3	Publications	224

List of Figures

2.1	Cirrus Clouds [2]	10
2.2	Geometrical shapes of ice particles present in [3]	15
2.3	An illustration of the geometry of Fraunhofer diffraction [4]	25
2.4	Diffraction by a single slit (a) wide slit (b) narrow slit [5]	30
2.5	Diffraction by circular aperture [6]	31
2.6	Diffraction by rectangular aperture [6]	32
2.7	Light rays at a boundary of the surface (a) parallel to the incident plane and (b) normal to the incident plane [7]	33
2.8	The reflection generated by a surface that conducts perfectly where (a) illus- trates parallel polarisation and (b) illustrates perpendicular polarisation [8].	40
2.9	Geometry of the problem [9]	42
2.10	Geometry of the problem [9]	43
2.11	Total field by UAPO method [9]	45
3.1	Incident wavefronts along the air-dielectric interface	49
3.2	The rotation of incident angle by the angle of the wedge	52
3.3	The truncated incident field by the wedge	57

3.4	The S and P polarisations transmission coefficient vs. the angle when $n_1 = 1$ and $n_2 = 1.33$	58
3.5	The transmitted field from the first face of the wedge	59
3.6	Received field at the second face of the wedge	60
3.7	Reflection coefficient vs. angle when $n_1 = 1.33$ and $n_2 = 1$	61
3.8	The reflected field from the second surface of the wedge (surface B)	62
3.9	Shifted to face A of the wedge	63
3.10	Reflected field from face A of the wedge	64
3.11	The transmitted field to the second surface (face B) of the wedge	65
3.12	Reflected field from the second surface (face B) of the wedge	66
3.13	Flowchart of the ray-tracing method (the numbers are mapped to the line numnber in the algorithm used for the implementation)	69
3.14	Result of the ray tracing method by the dielectric wedge	71
4.1	Ray-tracing and physical optics by the prism flowchart 1 (the steps are mapped to the algorithm used for the implementation)	73
4.2	Ray-tracing and physical optics by the prism flowchart 2 (the steps are mapped to the algorithm used for the implementation)	74
4.3	Result of the ray-tracing method for the prism	79
4.4	PO solution of the total incident field to the bottom facet of the prism . .	80
4.5	PO solution of the total field in the first reflection inside the prism	80
4.6	PO solution of the total field in the second reflection inside the prism . . .	81
4.7	PO solution of the total field in the third reflection inside the prism	81
4.8	Average path length (μm) vs. angle of incidence (degree) vs. position of the incident field angle to the prism	82

4.9	Average path length (μm) vs. the incident field angle (degree)	83
4.10	propagation of rays from X_i to X_j	86
4.11	Green's function implementation flow chart	88
4.12	Ray-tracing by a dielectric prism	90
4.13	FFT of the Green's function for S-polarization	91
4.14	FFT of the Green's function for P-polarization	91
4.15	Physical optics method vs. Green's function (P-polarisation)	93
4.16	Physical optics method vs. Green's function (S-polarisation)	93
5.1	Flowchart of the ray-tracing method by the hexagonal ice crystal (the steps are mapped to the algorithm used for the implementation)	95
5.2	Flowchart of PO method by the hexagonal ice crystal (the steps are mapped to the algorithm used for the implementation)	96
5.3	Result of the ray-tracing method for the hexagonal ice crystal	103
5.4	PO solution of the total field in the first reflection in hexagonal ice crystal	103
5.5	PO solution of the total field in the second reflection in hexagonal ice crystal	104
5.6	PO solution of the total field in the third reflection in hexagonal ice crystal	104
6.1	Spherical coordinate system	109
6.2	Rotation by orthorgonal shearing	112
6.3	labelling the facets of the hexagonal prism shape	118
6.4	Triangular prism facets	119
6.5	Labelling bullet crystals facets	119
6.6	Incident and refracted ray	120
6.7	Incident and reflected ray	121

6.8	Incident field at the bottom facet of the hexagonal prism ice crystal	123
6.9	Refracted and reflected fields inside the hexagonal prism ice crystal	124
6.10	High-level flowchart of PO by dielectric prism	126
6.11	3D ray-tracing by a dielectric prism (the steps are mapped to the algorithm used for the implementation)	127
6.12	3D PO by a dielectric prism (the steps are mapped to the algorithm used for the implementation)	128
6.13	Single ray-tracing by a dielectric prism	134
6.14	Single ray-tracing by a dielectric prism	134
6.15	Multiple ray-tracing by a dielectric prism	135
6.16	Multiple ray-tracing by a dielectric prism	135
6.17	Triangular prism facets	136
6.18	Incident field to the bottom facet of the dielectric prism	137
6.19	First order of reflection inside the dielectric prism	138
6.20	Second order of reflection inside the dielectric prism	139
6.21	Third order of reflection inside the dielectric prism	140
6.22	Fourth order of reflection inside the dielectric prism	141
6.23	Fifth order of reflection inside the dielectric prism	142
6.24	Total incident field in prism	143
6.25	Total incident field in prism	143
6.26	Field of 1st order of reflection in prism	143
6.27	Field of 1st order of reflection in prism	143
6.28	Field of 2nd order of reflection in prism	143
6.29	Field of 2nd order of reflection in prism	143

6.30	Field of 3rd order of reflection in prism	144
6.31	Field of 3rd order of reflection in prism	144
6.32	Field of 4th order of reflection in prism	144
6.33	Field of 4th order of reflection in prism	144
6.34	Field of 5th order of reflection in prism	144
6.35	Field of 5th order of reflection in prism	144
6.36	3D ray-tracing by a hexagonal prism ice crystal (the steps are mapped to the algorithm used for the implementation)	146
6.37	3D PO by a hexagonal prism ice crystal (the steps are mapped to the algo- rithm used for the implementation)	147
6.38	Single ray-tracing by a 3D hexagonal prism ice crystal	153
6.39	Multiple ray-tracing by a 3D hexagonal prism ice crystal	153
6.40	The incident field by hexagonal prism	154
6.41	The incident field by hexagonal prism	154
6.42	Field of 1st order of reflection in hexagonal prism	154
6.43	Field of 1st order of reflection in hexagonal prism	154
6.44	Field of 2nd order of reflection in hexagonal prism	154
6.45	Field of 2nd order of reflection in hexagonal prism	154
6.46	Field of 3rd order of reflection in hexagonal prism	155
6.47	Field of 3rd order of reflection in hexagonal prism	155
6.48	Field of 4th order of reflection in hexagonal prism	155
6.49	Field of 4th order of reflection in hexagonal prism	155
6.50	Field of 5th order of reflection in hexagonal prism	155
6.51	Field of 5th order of reflection in hexagonal prism	155

6.52	3D ray-tracing by a bullet ice crystal flowchart	157
6.53	3D PO by a bullet ice crystal flowchart	158
6.54	Bullet ice crystal	159
6.55	Multiple ray-tracing by a 3D bullet ice crystal	159
6.56	The incident field by bullet ice crystal	160
6.57	The incident field by bullet ice crystal	160
6.58	Field of 1st order of reflection in bullet ice crystal	160
6.59	Field of 1st order of reflection in bullet ice crystal	160
6.60	Field of 2nd order of reflection in bullet ice crystal	160
6.61	Field of 2nd order of reflection in bullet ice crystal	160
6.62	Field of 3rd order of reflection in bullet ice crystal	161
6.63	Field of 3rd order of reflection in bullet ice crystal	161
6.64	Field of 4th order of reflection in bullet ice crystal	161
6.65	Field of 4th order of reflection in bullet ice crystal	161
6.66	Field of 5th order of reflection in bullet ice crystal	161
6.67	Field of 5th order of reflection in bullet ice crystal	161
6.68	Wave vector components in hexagonal prism ice crystal	166
6.69	Wave vector components in hexagonal prism ice crystal	166
6.70	Wave vector components on bullet shape ice crystal	167
6.71	Wave vector components on bullet shape ice crystal	167
6.72	Geometry of the scattering problem	171
6.73	Relative amplitude of the scattered field at $\phi = 0^\circ$. Prism parameters: $n=1.787$, $d=10 \mu m$, $h=20 \mu m$, $\lambda=2 \mu m$, estimated error=0.664%	174

6.74	Relative amplitude of the scattered field at $\phi = 90^\circ$. Prism parameters: $n=1.787, d=10 \mu m, h=20 \mu m, \lambda = 2 \mu m$, estimated error= 3.745%	174
6.75	Relative amplitude of the scattered field at $\phi = 0^\circ$. Prism parameters: $n=1.787, d=20 \mu m, h=20 \mu m, \lambda = 2 \mu m$, estimated error=0.398%	176
6.76	Relative amplitude of the scattered field at $\phi = 90^\circ$. Prism parameters: $n=1.787, d=20 \mu m, h=20 \mu m, \lambda = 2 \mu m$, estimated error=4.46%	176
6.77	Relative amplitude of the scattered field at $\phi = 0^\circ$. Prism parameters: $n=1.787, d=5 \mu m, h=5 \mu m, \lambda = 2 \mu m$	178
6.78	Relative amplitude of the scattered field at $\phi = 90^\circ$. Prism parameters: $n=1.787, d=5 \mu m, h=5 \mu m, \lambda = 2 \mu m$	178
6.79	Relative amplitude of the scattered field at $\phi = 0^\circ$. Prism parameters: $n=1.33, d= 10 \mu m, h=10 \mu m, \lambda = 2 \mu m$, estimated error=2.06%	180
6.80	Relative amplitude of the scattered field at $\phi = 90^\circ$. Prism parameters: $n=1.33, d= 10 \mu m, h=10 \mu m, \lambda = 2 \mu m$, estimated error=0.41%	180
6.81	Relative amplitude of the scattered field at $\phi = 0^\circ$. Prism parameters: $n=1.33, d= 10 \mu m, h=2 \mu m, \lambda = 2 \mu m$. Plane wave incidence direction: $\theta^i=160^\circ, \phi^i=0^\circ$, estimated error=14%	182
6.82	3D scattering pattern obtained with RL-GO method	182
7.1	Rough surface schematic	186
7.2	Rough surface model using Guassian Height Distribution [10]	186
8.1	labelling the facets of the hexagonal prism shape	205
8.2	Triangular prism facets	210
8.3	Labelling bullet crystals facets	214

8.4	Relative amplitude of the scattered field at $\phi = 0^\circ$. Prism parameters: $n=1.787$, $d=10\ \mu m$, $h=10\ \mu m$, $\lambda=2\ \mu m$, normal incidence	223
8.5	Relative amplitude of the scattered field at $\phi = 0^\circ$. Prism parameters: $n=1.787$, $d=15\ \mu m$, $h=5\ \mu m$, $\lambda=2\ \mu m$, normal incidence	223

1 — Introduction

Computational electromagnetics has gained widespread use in weather radar, remote sensing, bio-medical diagnosis, meteorology and astrophysics. In polarimetry, satellite radiometer and other sensors are used to radiate electromagnetic (EM) waves with unique polarisations to the atmosphere or earth surface in order to predict, deduce or interpret the properties of objects or targets within the surrounding environment.

Having knowledge of electromagnetic field propagation characteristics is essential in the analysis and planning of optical systems and antennas. The models of propagation prediction based on ray-tracing are the most employed techniques in modern radio communication systems [11]. The ray-based models allow calculation of the magnitude and phase of the received electromagnetic field and also the delay of each ray, which is due to the mechanisms of propagation [11]. The latter are often complex and can generally be attributed to the phenomena of reflection, diffraction, transmission and scattering. It is well known that when the dimension of the systems are large in terms of electromagnetic wavelength, the diffraction contributions due to material discontinuities cannot be negligible and calculated accurately. By using methods such as Finite Element Method (FEM) and Finite-Difference Time-Domain (FDTD) [12], [13], it is possible to obtain reliable solutions for scattering problems. These techniques unfortunately have a drawback when the frequency increases, the computations become intractable or inefficient at high frequencies. In addition, it is

very hard to understand the physical aspects of the propagation mechanisms in this kind of approach where the FDTD and FEM methods are used [14].

In order to understand the radiation of the atmosphere system and its climate, having knowledge of the properties of scattering and absorption in the atmosphere system has to also be taken into account. The ice crystals represent a large number of cloud particles. They are non-spherical in shape and are irregular in structure. This study was motivated by the variety of ice crystal sizes and shapes. To achieve a reliable modelling for non-spherical ice-crystals in cirrus clouds, basic scattering, polarisation and absorption data are required. Furthermore, the polarisation and absorption data is needed to interpret bidirectional reflectance observations, heating rates from the space, air and ground. In addition, scattering and absorption data is needed for the development of remote sensing techniques to infer cloud optical depth, temperature and the size of ice crystals [15], [1].

Cirrus clouds are distributed globally and present in all latitudes. These clouds have a huge influence on climate and weather processes on all scales and have a huge effect on the radiative budget of the earth and its atmosphere system. They cover about 30% - 40% globally, which is a very high percentage. They are composed of non-spherical ice crystal with various shapes and sizes. The ice crystal shapes can be defined by incident coordinate systems and appropriate geometric models. These shapes include: the complex bullet rosettes, hollow columns, aggregates, dendrites, capped columns and hexagonal and plates (which is the simplest form). However, the exact solution of light scattering by the nonspherical ice crystal remains unfeasible due to proper coordinate systems cannot be defined to solve the basic electromagnetic equations that are derived from Maxwell's equations [16].

Ice crystals are very large compared to the infrareds wavelength in a sense that they are dielectric objects that have angular facets. One method of tackling the problem is when the wave enters the ice crystal and reflects from the inside. However, some of the wave will go through, and some of the wave will reflect. There are many possible ways to solve an electromagnetic problem [17]. One method is to solve the electromagnetic problem is to satisfy the boundary condition. Therefore, the set of functions can represent waves and separate functions that are orthogonal to each other. The solution is made up of a summation of possible solutions. Then, the combination of possible solutions that meet the boundary condition can be found [17].

Various studies have proved that light that is scattered by ice crystal contains scattering and absorption inclusions. It was computed by a combination of ray-tracing and Monte-Carlo techniques. It was also observed that the internal part of an ice crystal might internally scatter. This is due to the fact that the soluble particle that is trapped inside the crystal may not go into a solution that is going to change the refractive index of the crystal [18], [19].

However, the scattering solution in the infrared region of the spectrum is a complex problem. There are established methods that have been used to solve scattering methods, such as Mie, T-matrix and Rayleigh theories which are mentioned in [20]. These methods are not so efficient at infrared wavelengths due to size parameter, which typically can be in order of 100 of EM propagation wavelength or more, that leads to intensive computation. In this work, a new approach based on physical optics is presented in which the scattering by prismatic dielectric ice crystals which are electrically large is evaluated. In this method, the total scattered amplitude in any direction can be evaluated by application of the re-

action theorem to a volume integral in principle from a knowledge of the internal field distribution. This integral, in turn, can be converted to an integral over the equivalent surface current distribution. The method enables the evaluation of the total surface field by considering the internally transmitted and multiplying the reflected and diffracted contributions, which are obtained by the application of FFT and non-linear rescaling of the spatial frequency domain on each order of reflection, which meet the boundary conditions.

This thesis focuses on the development of a new approach that is based on physical optics method. The approach allows the study scattering by electrically large smooth dielectric ice crystal where it can be extended further in future to consider surface roughness and internal scatterers. In this method, the total scattered amplitude in any direction is evaluated by application of the reaction theorem to a volume interval in principle from a knowledge of the internal field distribution. This integral in turn can be converted to an integral over the equivalent surface current distribution. The method enables the evaluation of the total surface field.

1.1 Motivation

There are many asymptotic approaches to analyse scattering from ice crystals. One of the approaches is to assume that they are randomly oriented and the behaviour of the whole system can be observed. This does not require a full understanding of the properties of individual crystals as we are treating the ice crystals as a bulk. As far as the scattering by individual crystals is concerned, the most simplistic approach is the use of the ray-tracing method. Ray-tracing is relatively good for ice crystals that are much larger than the wavelength but they do ignore diffractive effects and have a limited analysis for the scattering problem. When scatterers are moderate in size, they are time consuming to analyse the scattering in an exact method, such as the T-matrix approach [20]. What is needed is to incorporate more of the behaviour of the scattering that depends on physical scattering methods and the electromagnetic response of the crystal.

In many literatures [21], [17], [18], [22], monte-carlo and ray-tracing techniques were used to study scattering in ice crystals. The problem with these methods is that they are statistical use and doesnt have strong physical bases. What needed to be done is to study the physical scattering by a single ice crystal and build up through a database of many crystals and different shapes. As a starting point, the wedge diffraction is considered. Scattering by a wedge is a problem that has been tackled for a long time and is relatively straightforward to deal the impenetrable wedge problem. As for the penetrable dielectric wedge, the wave can be scattered by the vertex of the wedge and can also pass through, which makes it more complicated [21], [17], [18], [22].

The approach taken in this thesis is based on the physical optics method and this by definition will take into account the diffractive effect and also the refractive effects. The proposed method is applied on homogeneous (smooth) ice crystals shapes. In this approach, the scattered field entirely depends on the field distribution internally to the crystal. Hence, the motivation of this work is to create a physical optics solution of scattering by dielectric ice crystals which operates faster than the existing methods such as method of moment (MoM) and T-matrix [20]. the speed will be comparable to that in ray-tracing solution. The advantage of the physical optics method is that it includes reflection, refraction and diffraction effects unlike the ray tracing which only includes reflection and refraction effects. Hence, this research is useful in modeling the scattering by ice crystals as the method can be helpful in the studies that are related to climate and weather observations. The ice crystals in cirrus clouds play a major part in weather processes.

1.2 Thesis outline

The remainder of this chapter describes the layout of the thesis, which is organised into a further six chapters.

Chapter 2 starts with background information about cirrus clouds and its microphysical properties and formation. In addition, it includes a description of the cirrus cloud problem in climate research and dielectric properties of ice crystals. The Fraunhofer diffraction is explained with the equations in both cartesian and polar coordinates and further examples of diffraction are illustrated. This chapter also includes a description of many conventional methods to generate solutions in scattering problems.

Chapter 3 presents the physical optics (PO) and ray-tracing approach to scattering by dielectric wedge. The classical wedge is studied as a 2D problem. The approach is presented and compared in terms of the phase variations per reflection for both the PO and ray-tracing. The result of this chapter shows an agreement between the ray-tracing and PO in terms of phase shift in each reflection after the plane wave incident on the wedge.

Chapter 4 presents the physical optics (PO) and ray-tracing approach to scattering by dielectric prism. The prism here is studied as a 2D problem. The approach is presented and compared in terms of the phase variations per reflection for both the PO and ray-tracing. The result of this chapter shows an agreement between the ray-tracing and PO in terms of phase shift in each reflection after the plane wave incident on the prism. In addition, the result of PO was compared with the Green's function method and an agreement between results were achieved. the work for this chapter has been published in PIERS (Progress in Electromagnetic Research Symposium) conference Shanghai 2016.

Chapter 5 presents the physical optics (PO) and ray-tracing approach to scattering by dielectric hexagonal ice crystals. The hexagon here is taken as a 2D problem. The approach is presented and compared in terms of the phase variations per reflection for both the PO and ray-tracing. The result of this chapter shows an agreement between the ray-tracing and PO in terms of phase shift in each reflection after the plane wave incident on the hexagonal ice crystals. this chapter has been published in PIERS (Progress in Electromagnetic Research Symposium) conference Singapore 2017

Chapter 6 represents the 3D modelling of the Physical Optics (PO) and ray-tracing approach to scattering by dielectric ice crystals in various shapes. The ice crystal shapes

include: hexagon, bullet and prism. The implementation and results for the 3D modeling are shown in this chapter. Furthermore, the total scattered field in any direction is evaluated by the application of the reaction theorem to a volume interval in principle from a knowledge of the internal field distribution. The results are compared with ray launching geometrical optics (RL-GO). This chapter shows the an agreement between PO and RL-GO in the far field scattering results. The work of this chapter has been accepted to be published in the Journal of Electronics and Optoelectronics.

Finally, Chapter 7 highlights the main contributions of the thesis; certain limitations of the work are identified, and areas for possible further study are suggested.

2 — Background and literature review

2.1 Cirrus clouds

The ten core types of cloud can be categorised as being either low, mid or high clouds [23]. Cirrus is an example of a high cloud which are made of ice crystals. Furthermore, there are various primary types of cirrus clouds including cirrus, cirrocumulus and cirrostratus. Cirrus clouds are typically wispy, threadlike, white feathery clouds composed of ice crystals that are often said to take the form of hair curls. Cirrus cloud structure is described, but more detailed descriptions are offered in [24] and [25]. The most commonly occurring cirrus cloud is a cirrostratus. Composed of ice crystals, cirrostratus often forms in sheets spanning hundreds or even thousands of miles and their translucent, milky appearance can sometimes create the impression that the sun and moon have halos. In contrast, cirrocumulus have small white flakes that give the appearance of being fleecy [23].

Cirrus clouds are worthy of further investigation because of their radiative contribution. This contribution is largely governed by the scattering and absorption properties of the ice crystals in the clouds [26]. Cirrus clouds normally form in the upper troposphere at

altitudes of at least 6 km. On occasions, cirrus clouds can produce optical phenomena including colourful arcs, halos and sun dogs (parhelia). Moreover, there are times when cirrus clouds are undetectable to the human eye or ‘optically thin’. At the global level, cirrus clouds account for approximately 30% of all high-level cloud cover, but this increases to 60-80% in the tropics [27], [28], [20], [29]. Meanwhile, [30] stated that cirrus accounts for a quarter of all high-level cloud cover, whereas [31] indicated that cirrus is present for approximately 40% of the time between January and July in regions of the world found between 60°N and 60°S. Therefore, cirrus performs a notable function in terms of atmospheric coverage. When attempting to model cirrus cloud, allowance must be made for several factors including their size, shape, the number distributions of ice crystals and how these relate to other variables, including air pressure, temperature, water content and the processes by which ice crystals form and alter over time. Furthermore, in order to gain a thorough appreciation of the radiative effects of cirrus cloud it is necessary to have a grasp of cloud microphysics as well as the ability of small particles in the atmosphere to scatter light [26].



Figure 2.1: Cirrus Clouds [2]

2.2 Microphysical and macrophysical properties and formation

Other than their scattering properties, crystal aspect ratios and the roughness of the surface, the most important macrophysical qualities of cirrus clouds are the ice particle size distributions (PSD), the ice water content (IWC) and the size spectral moments (IWC and median diameter) [23]. These have been extensively researched in the empirical literature. For instance, Korolev et al. [32] made detailed observations of continental stratified cirrus clouds above eastern Europe at temperatures ranging between -30 and -50°C .

In order to develop a thorough appreciation of the microphysics, it is also necessary to appreciate the intricacies of how ice particles form. For instance, an understanding of the development pathways that ice particles follow in clouds is required, and while a great deal is known about certain mechanisms, there remain considerable gaps in our knowledge [26].

Homogenous ice nucleation typically occurs at very low temperatures and involves the clustering of water molecules until the result is the formation of a bulk solid. It is possible for micrometer-sized pure water droplets to maintain a liquid form down to a temperature of -41°C , but at this stage homogenous nucleation takes place. However, the work in [33] noted that metastable bulk liquid water has been observed at temperatures as low as -46°C . Studies of the structure and conditions during the formation of water clusters from vapour have been made using molecular dynamics [34] and laser-based spectroscopy or electron diffraction [35]. Meanwhile, the work in [36] undertook an extensive review of cold small water clusters, revealing that only the larger clusters have a well ordered lattice structure

in their interior, and even they have a surface that is disordered. This is significant because it indicates that an ordered lattice structure is only possible after a threshold has been reached in terms of the number of molecules comprising the bulk [26].

The heterogeneous nucleation process is not well understood and involves an ice nucleating (IN) particle which acts as a third agent [37], [38]. Ice nucleation particles also comprise of aerosols and mineral dust [39]. In addition, they differ in terms of their nucleation efficiency, abundance and concentration. It is by reflecting on the abundance of natural and anthropogenic particles in the atmosphere that the importance of IN altered cloud microphysics becomes apparent. For instance, it has been estimated that the flux of mineral dusts is 1,000-3,000Tg yr⁻¹ [40]. Once airborne, these particles can remain aloft for several weeks and travel many thousands of miles before being released from the atmosphere. There are numerous pathways that have been identified: contact nucleation, immersion and (vapour) deposition mode nucleation. Contact nucleation occurs when an IN causes a droplet to freeze; immersion involves an IN being in contact with the liquid phase of the water, and deposition mode nucleation occurs when water molecules attach to the surface of the IN during the vapour phase and form an ice crystal [26].

IN exerts considerable influence over the nucleation and freezing kinetics of water. It has been observed that mineral dust, such as feldspar, acts as a highly effective ice nucleator and is able to raise the temperature at which droplets freeze by several degrees [41]. The cell membrane proteins of biological ice nucleators enable small droplets to freeze at temperatures between -2°C and just less than 0°C in the case of *Pseudomonas Syringae* [42]. In addition, the work in [43] noted that steroids are highly effective, while [39] observed that ice nucleation behaviour can be altered by organic molecules. However, it is important

to note that the formation of clouds and the distribution of particles will be influenced by the presence of any IN.

What effect the shape or nucleation material have on the macroscopic manifestation of ice crystals has yet to be established by researchers. This exerts considerable influence over their radiative qualities.

2.3 Single ice crystal properties

The radiative and bulk properties of clouds are governed by the distribution and shapes of ice crystals [44], [45]. The range of shapes (habits) vary from very simple hexagonal prisms to highly complex geometries including needles, columns, rosettes and aggregates. It is the humidity and temperature at the time of formation that determines the size, shape and number of ice crystals [46]. Shapes are likely to be more complex at the bottom of clouds or in clouds that are relatively dense as many factors play a role in determining the complexity such as humidity and wind velocity [20]. Ukichiro Nakaya was among the first to examine the relationship between the shape of atmospheric ice crystals, supersaturation and temperature [47]. This relationship is depicted in the Nakaya crystal habit diagram which was subsequently modified by [48] and [49]. Meanwhile, [50] provided a classification of 80 variants of crystal shapes which was later been updated by Kikuchi [51] who identified 121 unique shapes.

A recent study which involves direct and indirect observations of shapes and sizes focused on the irregularity of the ice crystal particles [52]. It was found from the molecular structure

of the ice that the form should be in a shape of plates or hexagonal columns, with an assumption that the growth condition is homogeneous. The actual form is not ideal due to the real atmospheric condition which is not homogeneous. Fluctuations of pressure, ambient temperature and wind velocity, in addition to the splitting and aggregation of particles can result in irregularities which introduce more complex irregular shapes of ice crystals. Recent analysis show a variety of ice crystal structures as shown in the figure below [53], [54]. There are 78 classified crystal particle shapes. These are several drawing of the shapes and these are assumed to be free from impurities [53], [55].

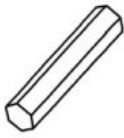

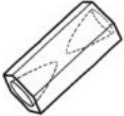

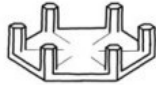

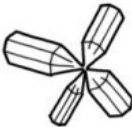






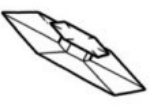



				
Simple Prisms	Solid Columns	Sheaths	Scrolls on Plates	Triangular Forms
				
Hexagonal Plates	Hollow Columns	Cups	Columns on Plates	12-branched Stars
				
Stellar Plates	Bullet Rosettes	Capped Columns	Split Plates & Stars	Radiating Plates
				
Sector Plates	Isolated Bullets	Multiply Capped Columns	Skeletal Forms	Radiating Dendrites
				
Simple Stars	Simple Needles	Capped Bullets	Twin Columns	Irregulars
				
Stellar Dendrites	Needle Clusters	Double Plates	Arrowhead Twins	Rimed
				
Fernlike Stellar Dendrites	Crossed Needles	Hollow Plates	Crossed Plates	Graupel

Figure 2.2: Geometrical shapes of ice particles present in [3]

The size and complexity of ice crystals and mesoscopic surface structures determine the light scattering properties of individual crystals [26]. Climate models require information about the radiative properties of clouds and these details can be obtained by measuring the light scattering properties of individual crystals during the scattering phase function. The phase function $p(\overrightarrow{\Omega_{inc}}, \overrightarrow{\Omega_{sca}})$ sets out the likelihood of an approaching photon along $\overrightarrow{\Omega_{inc}}$ being scattered into $\overrightarrow{\Omega_{sca}}$, whereby the scatterer is at the hub of the coordinate system. Having established this, it can be applied to represent the scattering properties of a collection of random particles with a phase function that depends on $\cos(\theta)$ alone. the scattering angle $\cos(\theta)$ is equivalent to $\overrightarrow{\Omega'_{sca}} \cdot \overrightarrow{\Omega_{inc}}$. In an attempt to clarify this in a relatively simple manner, the asymmetry parameter g is given as [26]:

$$g = \langle \cos(\theta) \rangle = \frac{1}{2} \int_{-1}^1 p(\cos(\theta)) \cos(\theta) d \cos(\theta) \quad (2.1)$$

The asymmetry parameter is an indication of the amounts scattered forwards and backwards expressed as a ratio. Knowledge of this value is important when it is necessary to have an appreciation of the amount of radiation reflected back into space. A cloud that appears to be bright when viewed from space will have a relatively low value, whereas a cloud that appears to be transparent will have a relatively high value [26].

The value assigned to g will fall within the range of -1 (fully backwards) and +1 (fully forwards). Furthermore, g is routinely applied in climate models as a measure of cloud forcing [56].

A measure that is commonly applied in energy-balance calculations is the single-scattering

albedo:

$$\omega = \sigma_s / (\sigma_a + \sigma_s) \quad (2.2)$$

where σ_s is the scattering coefficient and σ_a is the absorption coefficient.

The biggest issue faced is when obtaining phase functions for atmospheric particles. Spherical particles (e.g. droplets) do not pose a significant problem because Maxwell's equations can be separated and [57] arrived at a precise solution. However, particles that are not spherical present more of a problem and several methods have been proposed including Rayleigh scattering, Mie theory, analytical models grounded in Maxwell's equations, geometrical optics, and numerical methods based on discretisation in terms of time or space [53]. The choice of methodology will be determined by the size of the particle relative to the scattered wavelength (i.e. size parameter):

$$x = 2\pi r / \lambda \quad (2.3)$$

where λ is the wavelength and r is the average length of a particle. Researchers in the empirical literature assign their own meaning to the size parameter. For instance, r could refer to height or diameter, whereas for geometries that are not uniform, the diameter d is deemed to be the furthest distance between the points and $r = d/2$ [26].

The intention of these methods is to confirm whether or not a particle is small in comparison to the wavelength (usually determined as $r < \lambda/10$). If this is the case, the selected method would be Rayleigh scattering on a dipole. In contrast, if the particle is large in comparison to the wavelength, the selected methodology would be geometrical optics with ray-tracing

in order to generate estimates of scattering phase functions [58], [59], [60].

The scattering properties of an ensemble can be determined by utilising the resulting phase functions. This approach has been explained in detail in [61] and [62]. The scattering phase function for the ensemble is estimated by employing a Monte Carlo integration [63] that orientates the ensemble crystals randomly.

Regardless of the methodology selected, it is necessary to represent a single crystal and it can be particularly problematic to include surface effects. It is also crucial that the surfaces are shapes that are related to the atmospheric humidity, temperature and particle dynamics [26].

2.4 The cirrus clouds problem in climate research

Due to the high-altitude cirrus clouds that involve their radiative, thermodynamic and microphysical properties, there problems have been identified from this aspect which are unsolved in climate research [64], [65], [66]. There were many projects such as The International Cirrus Experiment (ICT) and the First International Satellite Cloud Climatology Project (ISCCP) which cover the ice clouds physics from both theoretical and experimental points of views [54], [67]. The cirrus clouds can affect the balance of the energy in the Earth-atmosphere system which depends upon the global distribution of greenhouse-versus-albedo effect of this cloud type. Hence, an in-depth knowledge of the extent of the interaction of cirrus cloud with solar radiation is important of climate research. Furthermore, an improved computation of the radiative transfer at a variety of wavelengths is

required for a detailed study of the optical properties from satellite radiance measurements and global determination of cloud cover [68], [69], [70].

There are many studies on the optical properties of cirrus clouds that have been made to improve the understanding and have knowledge about the single scattering by a hexagonal-shaped ice crystals. Studies by Coleman and Liou and by Takano and Liou describe the scattering of hexagonal-shaped ice crystals in geometrical optics by using the ray-tracing technique [71], [72]. Their study was restricted to hexagonal columns or plates. Furthermore, Rockwitz developed a model with the ray-tracing technique which considers the convex particles bound by plane surfaces and has been applied only for a horizontal oriented hexagonal column [73]. However, Macke et al. has extended the research by considering more irregular shapes and concave ice particles [53], [69].

There are methods found in literature which contribute to the scattering by ice crystals and generally can be applied to compute light scattering by non-axisymmetric particles. The methods vary from exact methods, such as the T-matrix method [74] and semi-exact methods, such as the Finite Difference Time Domain method (FDTD) [75] and the Discrete Dipole Approximation method (DDA) [76]. A discrete dipole approximation can be employed to numerically calculate wave propagation [76]. Given that particles are indicated as dipoles on a numerical grid with $a < \lambda/10$ spacing, the limitations of the computational resources effectively constrain the solvable particle sizes at an early stage.

These methods, namely T-matrix, DDA and FDTD, are considered the most efficient and can be readily applied to arbitrary particle morphologies. These methods are very demanding but have a limitation which is that they cannot be readily used when the

scatterer is much larger than the wavelength.

If particles are deemed to be an intermediate size, diffraction will come into play and hybrid methods are employed.

The most appropriate methods for scatterers that are much larger than the wavelength are the Physical Optics or Geometrical Optics approximation. In regards to the Geometric Optics approximation, the light scattered can be divided into two parts: the transmitted or reflected by scatterer, and the external diffracted light. Methods were improved and was used by combining ray-tracing and diffraction contributions. An example of this would be ray-tracing with diffraction of facets (RTDF) [77] and also in [75], [78] and [79].

The computation methods that use a separate ray-tracing and diffraction contribution are still widely used. For instance, the work in [63] used an external diffraction, which is by Kircchoff approximation to model diffraction on the projected cross-section.

Hesse et al. [11] implemented a method that approximates the light scattering by absorbing faceted particles which are large compared to the wavelength. It was done by adding approximating reflection and diffraction. This method was done for smooth hexagonal prism and was extended further to slightly rough surfaces. The method was claimed to be computationally fast. In this method, the facets of the particle are treated as independent diffracting apertures. While there is a strong absorption, two main contributions to the scattered field are needed to be evaluated. These contributions are the externally diffracted field and the reflected field. The evaluation was done separately for each contribution using Jones calculus (which includes phase tracing) and then added. then, the azimuthally averaged phase functions of scattered intensity are computed.

2.5 Dielectric properties of ice crystals

Ice crystals are described as a complex mixture of ice with air, super-cooled water, or both. The mixing ratio between these elements varies considerably depending upon the external meteorological conditions which are exposed to the ice particles [80]. It is common to use the effective medium theories (EMTs) which are used to estimate the average optical constants of inhomogeneous materials [81]. Many effective medium theories were made for different structures of the medium and with different shapes, sizes and physical properties so that the dielectric properties of a particular ice crystal can be analysed. In order to theoretically treat the properties of such mixtures, it is important to assume that the component is large so their dielectric functions can be assumed. Furthermore, the component has to be small compared to the wavelength so that the quasi-static arguments are made. In order to achieve homogenisation of the composite mixture, it is important to accurately determine the dielectric constant of complex mixture constituent parts by using established theoretical and empirical formulas [80], [81], [82].

Refractive index of ice

The dielectric constant of ice at microwave frequencies is usually expressed by a complex dielectric constant as [83],

$$\epsilon = \epsilon' + i\epsilon'' \quad (2.4)$$

Or the complex index of refraction,

$$N = n' + in'' \quad (2.5)$$

By assuming the time factor ($\exp(-i\omega t)$), both quantities above are related to each other by the following expression [83],

$$N = \sqrt{\epsilon} \quad (2.6)$$

The real part of ϵ is called the relative permittivity, whereas the imaginary part is called the loss factor. On the other hand, the real part of N is the wave velocity (or phase shift), whereas the imaginary part is associated with the attenuation of the wave [83].

Normally, the dielectric behaviour of ice is discussed using the Debye's theory [84], [85]. The theory assumptions lead to the formula called the Debye Dispersion Formula as follows [84], [85],

$$\epsilon = \epsilon_{\infty} + \frac{\epsilon_0 - \epsilon_{\infty}}{1 - i\left(\frac{\lambda_s}{\lambda}\right)} = \epsilon' + i\epsilon'' \quad (2.7)$$

It can be written as [84], [85],

$$\epsilon' = \epsilon_{\infty} + \frac{\epsilon_0 - \epsilon_{\infty}}{1 - \left(\frac{\lambda_s}{\lambda}\right)^2} \quad (2.8)$$

$$\epsilon'' = \frac{(\epsilon_0 - \epsilon_{\infty}) \left(\frac{\lambda_s}{\lambda}\right)}{1 - \left(\frac{\lambda_s}{\lambda}\right)^2} \quad (2.9)$$

Where ϵ_{∞} and ϵ_0 are the infinite and static frequency dielectric constant respectively. The λ_s and λ represent the relaxation wavelength of incident radiation. ϵ' and ϵ'' depend upon two parameters at least. These parameters are the temperature and the wavelength. The above equation agrees with the experimental work proposed in [84] at temperature range of 0-70°C and frequency range upto 10 GHz. However, it failed at higher frequencies. However, Ray [86] has proposed a model for dielectric properties of ice over a high temperature range and large frequency spectrum. Instead of using Debye's formulas for the

module, Ray has used an extension of Debye's theory by Cole [87] modified by a frequency independent conductivity σ , and it was as follows [87],

$$\epsilon' = \epsilon_{\infty} + \frac{(\epsilon_0 - \epsilon_{\infty}) [1 + (\frac{\lambda_s}{\lambda})^{1-\alpha} \sin(\frac{\alpha\pi}{2})]}{1 + 2(\frac{\lambda_s}{\lambda})^{1-\alpha} \sin(\frac{\alpha\pi}{2}) + (\frac{\lambda_s}{\lambda})^{2(1-\alpha)}} \quad (2.10)$$

$$\epsilon'' = \frac{(\epsilon_0 - \epsilon_{\infty}) (\frac{\lambda_s}{\lambda})^{1-\alpha} \cos(\frac{\alpha\pi}{2})}{1 + 2(\frac{\lambda_s}{\lambda})^{1-\alpha} \sin(\frac{\alpha\pi}{2}) + (\frac{\lambda_s}{\lambda})^{2(1-\alpha)}} + \frac{\sigma\lambda}{\sigma_0} \quad (2.11)$$

Where α denotes the spread parameter which takes a value between 0 and 1, $\sigma_0=18.8486 \cdot 10^{10}$. From the experimental data that Ray [86], [87] found as a function of temperature, the parameters ϵ_{∞} , λ_s and α value were fitted.

$$\epsilon_{\infty} = 3.168, \quad \alpha = 0.288 + 0.0052T + 0.00023T^2 \quad (2.12)$$

$$\lambda_s = 9.990288 \cdot 10^{-5} \exp \left[\frac{1.32 \times 10^4}{(T + 237) \times 1.9869} \right] \quad (2.13)$$

$$\sigma = 1.26 \exp \left[\frac{-1.25 \times 10^4}{(T + 273) \times 1.9869} \right] \quad (2.14)$$

$$\epsilon_0 = 2.03168 + 2.5T + 0.15T^2 \quad (2.15)$$

Where T represents the temperature in Celsius. Therefore, the refractive index calculation was made by Sadiku [83] for ice from temperature -20 to 0 °C at the frequency range of 0.6 to 300 GHz. The real part of the refractive index was from 1.78 (300 GHz) to 1.788 (0.6 GHz). The imaginary part of the refractive index was from $2.065 \cdot 10^{-4}$ (300 GHz) to $1.716 \cdot 10^{-2}$ (0.6 GHz).

Zhang et al. [88] studied the refractive index of Ih crystalline ice. The measurements were in the frequency range of 0.25-1.0 THz. The real part of the refractive index of ice crystal increases from 1.787 to 1.793 with the increase in frequency at a temperature of -30°C. The imaginary parts (n'') increases from 0.005 to 0.020. These results were agreed with Matsuoka and co-workers [89].

In ice, frozen water, there are strong covalent bonds between the water molecules which is what makes it solid. Consequently, the refractive index of the ice is much lower, particularly at radio frequencies. Conversely, at infrared/optical frequencies, the differences between ice and water are not so noticable.

In regards to the refractive index of air, the refractive index of air that is near Earth's surface can be assumed to be approximately 1.0003. This value cannot be distinguished with the refractive index of free space (vacuum) which is equal to 1 [90].

2.6 Fraunhofer Diffraction

The Fraunhofer diffraction equation is used in optics to model wave diffraction when the diffraction pattern is considered at a long distance away from the diffracting object (far field region). Furthermore, it models the waves diffraction when it is viewed as a focal plane of an imaging lens [6], [91]. Conversely, the diffraction that occurs in the near field region (near the object) is given by the Fresnel diffraction equation. The Fraunhofer diffraction was named after Joseph von Fraunhofer, although he was not involved in producing this theory [92] [93].

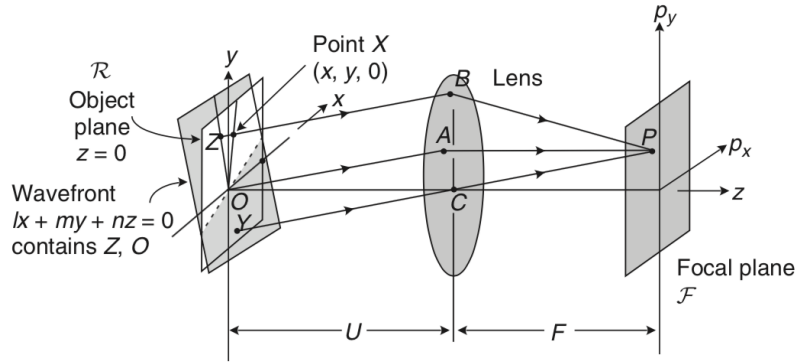


Figure 2.3: An illustration of the geometry of Fraunhofer diffraction [4]

The following sub-section will demonstrate when to apply the Fraunhofer equation and will show the Fraunhofer diffraction patterns for different apertures.

2.6.1 Fraunhofer diffraction equation

When a light beam is partially blocked by an interfered object or obstacle, some of the light gets scattered around the object. The light and dark bands are then often seen at the edge of the shadow. This result is known as diffraction [94]. The Kirchhoff diffraction equation delivers an expression which is derived from the wave equation. It describes the diffracted wave by the aperture [6]. The Fraunhofer diffraction is a simplified version of Kirchhoff's equation of diffraction and is used in modelling diffraction of light when the source of light and viewing plane are effectively at infinity with respect to the diffracting aperture [91].

The Fraunhofer diffraction is applicable when the diffracted wave that is observed in the far field region. The far field region occurs when the distance between the plane in which the pattern occurs and the aperture is large so that the difference in the optical path length from the aperture is less than the wavelength. It occurs when $\frac{W^2}{L\lambda} \ll 1$. Where W is the size of the aperture or the slit (the largest dimension of the aperture), λ is the wavelength and L is the distance of the aperture. Therefore, the far field can be defined as the range of distance that is located which is significantly larger than $\frac{W^2}{L\lambda}$. In this case, the Fraunhofer diffraction equation can be used to model the diffraction [4].

Furthermore, the Fraunhofer equation is applicable when the lens is used to focus the diffracted light [4]. When the plane wave reaches a positive lens and focuses on a point after it hits a lens, the rays have the same phase at the point of focus. Therefore, the light which is diffracted is focused with the lens. The Fraunhofer diffraction can be used to model the diffraction pattern [95].

Several of the analytical solutions of the Fraunhofer equation of different patterns are derived in the next subsections.

2.6.1.1 Cartesian coordinate

Consider that the aperture is in $x'y'$ plane with the origin in the aperture. The aperture is illuminated by a monochromatic wave of wavenumber (k) and wavelength (λ) with complex amplitude $A(x',y')$. Furthermore, the diffracted wave is in the x,y,z plane where m and l are the x,y direction cosines with respect to the origin. The complex amplitude of the diffracted wave is given by the following Fraunhofer diffraction equation as: [4]

$$U(x, y, z) \propto \iint_{Aperture} A(x', y') \exp\left(-j\frac{2\pi}{\lambda}(lx' + my')\right) dx' dy' \quad (2.16)$$

and by substituting the value $k = \frac{2\pi}{\lambda}$ to the equation 2.16 as follows,

$$U(x, y, z) \propto \iint_{Aperture} A(x', y') \exp\left(-jk(lx' + my')\right) dx' dy' \quad (2.17)$$

It can be noted from the above equation that the diffraction pattern form depends upon the direction of viewing only and not the distance. The diffraction pattern changes in size with the distance, but not with the form of diffraction. Furthermore, the Fraunhofer diffraction can be expressed in several equivalent mathematical forms. For example: [96]

$$U(x, y, z) \propto \iint_{Aperture} A(x', y') \exp\left(-\frac{jk(x'x + y'y)}{z}\right) dx' dy' \quad (2.18)$$

It can be noted that the above integral from the equation is the Fourier transform of the aperture function. It has two Fourier transforms for both x and y and it is evaluated at frequencies [97].

$$fx = \frac{x}{\lambda z} = \frac{l}{\lambda} \quad (2.19)$$

$$fy = \frac{y}{\lambda z} = \frac{m}{\lambda} \quad (2.20)$$

Therefore, the equation can be rewritten in terms of Fourier Transform as [97]

$$U(x, y, z) \propto \hat{f}[A(x', y')] f_x f_y \quad (2.21)$$

where $\hat{f}(\cdot)$ represents fourier transform The formulation of Fourier transform is very useful in solving problems that are related to diffraction.

2.6.1.2 Polar coordinates

The polar coordinate is more useful to use rather than the cartesian co-ordinates when the diffracting aperture has a circular symmetry [6]. It can be assumed that a point in the aperture has a coordinate ρ, ω giving:

$$x = \rho \cos \omega \quad , \quad y = \rho \sin \omega \quad (2.22)$$

and

$$x' = \rho' \cos \omega' \quad , \quad y' = \rho' \sin \omega' \quad (2.23)$$

$$\begin{aligned}
U(\rho, \omega, z) &= \int_0^\infty \int_0^{2\pi} A(\rho') \exp[-j \frac{2\pi}{\lambda z} (\rho \rho' \cos \omega \cos \omega' + \rho \rho' \sin \omega \sin \omega')] \rho' d\rho' d\omega' \\
&= \int_0^{2\pi} \int_0^\infty A(\rho') \exp[-j \frac{2\pi}{\lambda z} \rho \rho' \cos(\omega - \omega')] d\omega' \rho' d\rho'
\end{aligned} \tag{2.24}$$

where $A(\rho)$ is the complex amplitude at ρ' and the area $dx dy$ is converted to $\rho \rho' d\rho' d\omega'$. By using the integral form of Bessel Function [98]:

$$J_0(p) = \frac{1}{2\pi} \int_0^{2\pi} \exp(jp \cos \alpha) d\alpha \tag{2.25}$$

It becomes:

$$U(\rho, z) = 2\pi \int_0^\infty A(\rho') J_0\left(\frac{2\pi \rho' \rho}{\lambda z}\right) \rho' d\rho' \tag{2.26}$$

And the integration over ω , in equation 2.24, results 2π and the equation is symmetric circularly. Therefore, there is no dependence of $U(\rho, z)$ on ω . In this instance, the $U(\rho, z)$ is equal to Hankel transform or Fourier-Bessel of the aperture function ($A(\rho, z)$) [6].

2.6.2 Examples of Fraunhofer diffraction

2.6.2.1 Diffraction by single slit of infinite depth

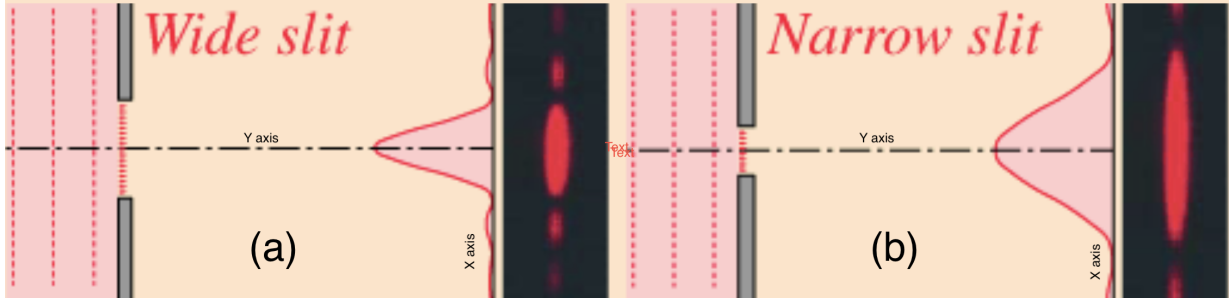


Figure 2.4: Diffraction by a single slit (a) wide slit (b) narrow slit [5]

Considering the width of the slit is W . The Fraunhofer diffraction pattern for a single slit is shown in the figure above where the y-axis represents the intensity (I) and the x axis represents the angle of observation (θ). As it can be seen from the pattern, the intensity is at its maximum at $\theta=0$ from the y axis in Figure 2.4 . This peak is followed by a series of peaks of decreased intensity. Most of the diffracted light intensity is between the first two minima [97]. The angle (α) which is subtended between the two minimum is given as [99]:

$$\alpha \approx \frac{2\lambda}{W} \quad (2.27)$$

From the above equation, It is noticed that when having a larger aperture size, we will have a smaller (α) subtended by the diffraction bands. The central band size at a distance z is given as [99]:

$$d_f = \frac{2\lambda z}{W} \quad (2.28)$$

Where d_f the diffraction pattern width.

2.6.2.2 Diffraction by a circular aperture

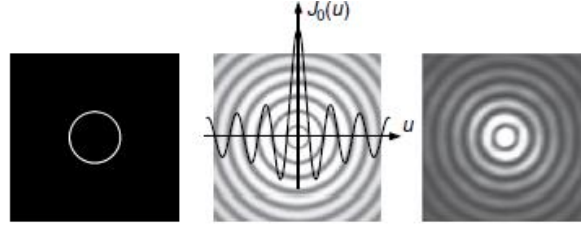


Figure 2.5: Diffraction by circular aperture [6]

The diffraction by circular aperture pattern is also known as the airy diffraction pattern. The airy diffraction pattern is shown in Figure 2.5 above [6]. Most of the light can be seen in the central disc. The angle that subtended by the airy disk (α) is shown as follows [6]:

$$\alpha \approx \frac{1.22\lambda}{W} \quad (2.29)$$

where W is the aperture diameter. The airy disk parameter has significance in imagining a system by limiting the ability of it to resolve the objects that are closely located.

2.6.2.3 Diffraction by rectangular aperture

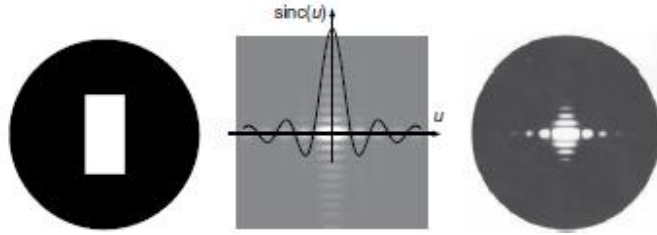


Figure 2.6: Diffraction by rectangular aperture [6]

As can be seen from Figure 2.6, the diffraction pattern by a rectangular aperture is given. In the centre, there is a semi-rectangular peak. In addition, there is a series of vertical and horizontal fringes [6]. In regards to the dimensions of the central band, these are related to the dimensions of the single slit in the same sense that for a single slit that the dimension in the slit is larger in the diffracted corresponding image. Furthermore, the fringes spacing is inversely proportional to the dimension of the slit. If the whole length of the slit is not illuminated by the illuminating beam, the vertical fringes spacing is determined by the illuminating beam dimension [6].

2.7 Fresnel Equations of Reflections

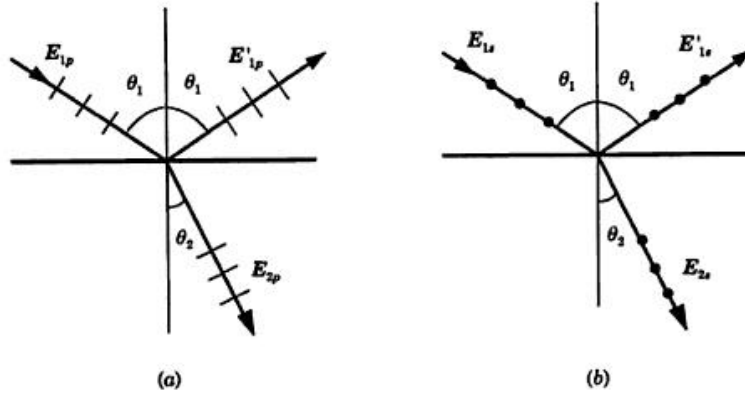


Figure 2.7: Light rays at a boundary of the surface (a) parallel to the incident plane and (b) normal to the incident plane [7]

Considering a plane wave hits onto a boundary of two transparent media. Part of the energy will get refracted to the second medium and part will get reflected to the first medium [100]. The reflected and refracted beams directions are determined by Snell's law which is as follows [100]:

$$\frac{\sin(\theta_1)}{\sin(\theta_2)} = \frac{n_2}{n_1} \quad (2.30)$$

Where θ_1 is the angle from the normal to the boundary of the first medium, θ_2 is the angle of the normal to the boundary of the second medium, n_1 is the refractive index of the first medium and n_2 is the refractive index of the second medium. It is worth mentioning that the relation between the refracted and reflected light intensities depends on the incident angle and the refractive indices of the median [100]. Furthermore, it depends upon the state

of the polarisation of the incident beam. In order to model the polarisation, the incident beam is decomposed into two polarisation components orthogonal to each other [7]. The vibration of the electric field of one component which is perpendicular to the incidence is called p-polarisation. The other component is orthogonal to the plane of incidence is called s-polarisation. S and P components is illustrated in dots and bars as can be seen in Figure 2.7. The reflection and refraction coefficients of s and p-polarisation are found by using Fresnel equations, which are [7]:

$$r_p = \frac{\tan(\theta_2 - \theta_1)}{\tan(\theta_2 + \theta_1)} \quad (2.31)$$

$$r_s = \frac{\sin(\theta_2 - \theta_1)}{\sin(\theta_2 + \theta_1)} \quad (2.32)$$

$$t_p = \frac{2 \sin \theta_2 \cos \theta_1}{\sin(\theta_2 + \theta_1) \cos(\theta_1 - \theta_2)} \quad (2.33)$$

$$t_s = \frac{2 \sin \theta_2 \cos \theta_1}{\sin(\theta_2 + \theta_1)} \quad (2.34)$$

The derivation of the above equations can be found in [101].

2.8 Geometrical and Uniform Theories of Diffraction

Electromagnetic scattering occurs when an object is inserted in the EM propagating path. Therefore, it results in modification in the surrounding space. The ability of solving and describing the scattering problem is the essence to many applications, such as designing antenna to identify radar targets and planning radio links [102]. Also, for the purpose of this thesis, where we need to analyse the scattering by dielectric ice crystals, the electromagnetic scattering and diffraction modeling is needed.

2.8.1 The Geometrical Theory of Diffraction

There are many conventional methods to generate solutions in scattering problems such as the Finite Element Method (FEM) or Method of Moment (MoM). These techniques have a considerable downside which is that the representation of the system is discrete by typically using the cell sizes on the order of one-tenth of the incident field wavelength. Due to the increase of degrees in freedom number with frequency, the computation become unmanageable (if not computer-intensive) [102], [8]. Therefore, the asymptotic methods work more efficiently at high frequencies. One of these methods is called the Geometrical Theory of Diffraction (GTD) which was found by Keller [12]. This theory combines diffraction with the Geometrical Optics (GO), which is a ray oriented framework. It is based on the assumption that the rays can represent waves and these rays represent the travelling direction of EM energy. Furthermore, the wave fields are mathematically characterised by polarisation, magnitude and phase propagation factors [102]. The diffraction depends

upon the obstacle surface geometry on the incident field in proximity to the points which create discontinuities in GO field reflection and incidence of shadow boundaries [12], [13].

The first step of GTD to solve a scattering problem is to divide it into smaller and simpler components. Each component represents a canonical geometry. Therefore the solution would be the sum of each solution from the canonical problem. Consequently, the Geometry Theory of Diffraction allows the solving of a large number of scattering problems by using the relatively small modeling problems solutions. Furthermore, this GTD technique can be combined with numerous techniques to solve scattering problems and obtain hybrid methods [103].

2.8.2 Uniform Theory of Diffraction

The Uniform Theory of Diffraction (UTD) which is a refinement of GTD as the GTD fails in the boundary layers near caustic and shadow boundaries. The UTD was discovered by Kouyoumjian and Pathak in 1974 [104]. The Uniform Theory of Diffraction overcomes the limitation of the GTD. It gives useful asymptotic solutions for the diffracted field calculation [105], [106]. This method has proven that it has good characteristics and it has good real structures with edges [107], [108].

2.9 Physical optics

Physical optics or wave optics is the branch of science that is used to explain a variety of effects including diffraction. The ray approximation of geometrical optics is not applicable to various phenomena including diffraction, interference and polarisation. Therefore, these phenomena are studied using the branch of science known as physical optics or wave optics. However, this does not extend to effects such as quantum noise which is studied with reference to coherence theory [109]. Physical optics is the name of an approximation employed in optics and falls somewhere between geometric optics which makes no allowance for wave effects, and the precise theory of full wave electromagnetism. While physical optics is not a precise physical theory, it has a closer affinity to physical aspects than ray or geometrical optics [109].

Physical optics estimates the field on a surface by utilising ray optics. Having done so, the scattered field is determined by integrating the field over the surface. In some respects there are similarities with the Born approximation in so far as the specifics of the issue are considered a perturbation [109].

This method is widely applied when it is necessary for diffraction effects to be estimated. This approximation can be applied in radio when estimating effects similar to optical effects. Various polarisation, interference and diffraction effects are modelled [109]. However, diffractions reliance on polarisation is not modelled. Moreover, the accuracy of the physical optics approximation is greater when applied in optics than in radio due to the fact that it is a high-frequency approximation.

In terms of radar scattering, the process involves taking the current of a tangent plane for a material with similar properties as the current on the region of a scatterer that is geometrically illuminated. Any regions that are in shadow are deemed to have no current. An integral across these approximate current is then used to arrive at the approximate scattered field. This is of benefit when faced with surfaces with limited reflection (lossy surfaces) and large, smooth convex forms [109].

In order to improve the accuracy of the ray-optics field or current at shadow boundaries or close to the edges, it is necessary to incorporate diffraction or creeping wave calculations [109], [110].

There are a number of limitations when gauging scattered fields using the standard theory of physical optics, including a loss of accuracy when not close to the specular direction. In 2004, the theory was enhanced in a way that provides specific solutions to issues surrounding wave diffraction by conducting scatterers in [111].

2.9.1 Physical optics approximation

The formula for the field scattered at the far zone by an object that conducts perfectly that is lit by means of an electromagnetic wave is as follows:

$$\underline{E}^s = -jk_0\zeta_0 \iint_S (\underline{I} - \hat{R}\hat{R})\underline{J}_S G(\underline{r}, \underline{r}') dS \quad (2.35)$$

where \underline{J}_S represents the current distribution upon the object's surface (S). k_0 represents

the wavenumber and ζ_0 is the impedance of free space. Meanwhile, the green function is given by [8]:

$$G(\underline{r}, \underline{r}') = \frac{e^{-jk_0|\underline{r}, \underline{r}'|}}{4\pi|\underline{r}, \underline{r}'|} \quad (2.36)$$

While \underline{r} represents the position vector at the observation point and \underline{r}' is the position vector at the integration point. \underline{I} refers to the (3x3 identity matrix and \hat{R} is the radiating element's unit vector.

Geometrical optics are utilised for the approximation of the current distribution \underline{J}_S . Importantly, it is only possible to achieve accurate measures if the object is a sufficient distance away from the source for it to be possible to describe the incident field on the basis of rays and wavefronts [8]. It is assumed for the purpose of this approximation that there is no surface current in the shadow region. In contrast, in the illuminated region, any location P on the surface of the object can be established if it is assumed that the way in which the incident electric field is reflected is akin to how it would occur from the infinite plane tangent to the point P at the surface [112].

If there is a perfectly conducting surface S , the following equation can be used to arrive at the surface current distribution:

$$\underline{J}_S = \hat{n} \times \underline{H} = \hat{n} \times (\underline{H}^i + \underline{H}^r) = 2\hat{n} \times \underline{H}^i \quad (2.37)$$

where \hat{n} represents the incidence point's unit vector normal to the surface, while \underline{H}^i repre-

sents the incident magnetic field. It is worthy of note that in the event that a plane wave impinges on a surface that is perfectly conducting, the outcome is for both polarisations (see Figure 2.8 below):

$$\hat{n} \times \underline{H}^i = \hat{n} \times \underline{H}^r \quad (2.38)$$

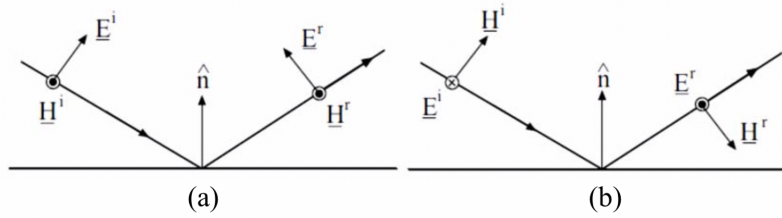


Figure 2.8: The reflection generated by a surface that conducts perfectly where (a) illustrates parallel polarisation and (b) illustrates perpendicular polarisation [8].

When assessing the field scattered from objects of finite conductivity, PO can be applied. When doing so, it is necessary to consider both the magnetic \underline{J}_{mS} and the electric \underline{J}_S surface currents in the radiation integral. As such, equation 2.35 is amended as follows:

$$\underline{E}^s = -jk_0 \iint_S [(\underline{I} - \hat{R}\hat{R})(\zeta_0 \underline{J}_S) + \underline{J}_{mS} \times \hat{R}] G(\underline{r}, \underline{r}') dS \quad (2.39)$$

It is important to note that the observation direction and the surface current's degree of approximation govern how accurate the results produced using the PO method prove to be. Furthermore, the accuracy of the field prediction is compromised when the contributions made by the areas obscured from direct illumination by the incident field are sizeable.

2.9.2 Uniform asymptotic physical optics method (UAPO)

In an attempt to address a series of diffraction problems, numerous uniform asymptotic physical optics methods have been arrived at [113], [114], [115], [116], [117]. Underlying all of these methods is the goal of applying a PO approximation of surface currents that are the same as those resulting from the incident field on a structure. It is the radiation integral (see equations 2.35 and 2.39) that is used to express the scattered field and this involves diffraction contributions as well as geometrical optics [8]. It is possible to establish the diffraction coefficients in closed form by utilising a uniform asymptotic assessment of the radiation integral and the steepest descent approach. These are given in terms of the UTD transition function and are able to offset the GO field discontinuities. However, it is important to note that these methods can only offer an approximation owing to the fact that surface currents in the radiation integral are derived from a PO estimation. Nevertheless, the results produced offer a high degree of accuracy relative to methods that are considered to be more rigorous. In addition, this method offers the advantage of being relatively simple to apply, thereby making it suitable for use in the absence of any precise analytical solutions [8].

2.9.3 UAPO solution for diffraction by dielectric wedge

In this section, some of the initial work of the uniform asymptotic physical optics solution was used to predict the field diffracted by the dielectric wedge taking an assumption that the dielectric wedge is a lossless medium. The work was done with the aid of research and selected theoretical analysis [9], [118].

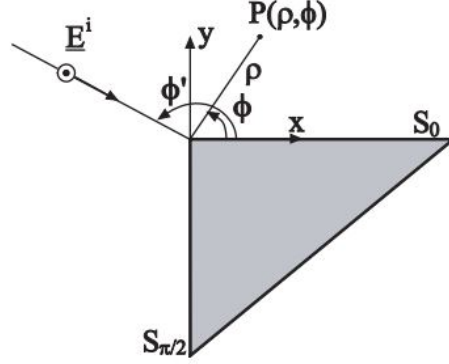


Figure 2.9: Geometry of the problem [9]

The problem is described from the above figure; the field was predicted to be diffracted by a lossless dielectric wedge. The dielectric wedge is illuminated by a normal incident uniform plane wave. This considered problem is divided into two parts: the inner part and the outer part. The inner part concerns the internal of wedge and the outer part is concerning the external of the wedge. In regards to the external part, it is assumed that the magnetic and electric PO surface currents, which are lying on the external faces of wedge, are sources in standard radiation integral [119], [120]. By uniform asymptotic evaluation of resulting integrals results the diffracted field surrounding the wedge in space in terms of transition function of UTD and Fresnel's reflection coefficients. Then, the inner part of the wedge was evaluated by identifying the PO surface current of the internal part of the wedge. After finding the surface currents, the diffracted field in the inner part is evaluated in the same way as the outer part of the wedge [9], [121].

2.9.3.1 Derivation of diffracted field solution

constant, ζ_0 is the characteristic impedance, I is 3x3 identity matrix, R is the vector from the radiating element, r and r' denote the observation and source points. The scattered field of the two surfaces of the wedge in the outer region are contributed separately so that [9]:

$$E_{out}^s = E_{0,out}^s + E_{\frac{\pi}{2},out}^s \quad (2.41)$$

Then the electric and magnetic current surfaces are expressed as [9]:

$$\zeta_0 J_{s,0}^{out} = E_0 (1 - R_0) \sin \varnothing' e^{jk_0 x \cos \varnothing'} z \quad (2.42)$$

$$\zeta_0 J_{ms,0}^{out} = -E_0 (1 + R_0) e^{jk_0 x \cos \varnothing'} x \quad (2.43)$$

From the above equation, R_0 is the Fresnel reflection coefficient which is associated with the surface S_0 . E_0 indicates the incident field by the origin. Then, the integral, which is associated with the outer surface S_0 , can be written as [9]:

$$E_{0,out}^s = z \frac{E_0 [(1 - R_0) \sin \varnothing]}{4\pi j} \int_C \frac{e^{-jk_0 \rho \cos(a \mp \varnothing)}}{\cos a + \cos \varnothing'} \quad (2.44)$$

By a uniform asymptotic evaluation of the above equation, it gives [9]:

$$E_{0,out}^s = z E_0 [(1 - R_0) \sin \varnothing' - (1 + R_0) \sin \varnothing] e^{-\frac{j\pi}{4}} \frac{F_t[2k_0 \rho \cos^2(\frac{\varnothing \mp \varnothing'}{2})]}{\cos \varnothing + \cos \varnothing'} \frac{e^{jk_0 \rho}}{\sqrt{\rho}} \quad (2.45)$$

Where $F_t[x]$ indicates a transition function which is a Fresnel integral. In regards to \mp , the $+$ sign applies when $0 < \varnothing < \pi$ whereas the $-$ sign is used when $\pi < \varnothing < \frac{\pi}{2}$. Then,

the PO surface currents are derived from the relation of the diffracted field with $E_{\frac{\pi}{2},out}^s$ as follows [9]:

$$\zeta_0 J_{s,\frac{\pi}{2}}^{out} = E_0 \left(1 - R_{\frac{\pi}{2}}\right) \cos \varnothing' e^{jk_0 x \sin \varnothing'} z \quad (2.46)$$

$$\zeta_0 J_{ms,\frac{\pi}{2}}^{out} = -E_0 \left(1 + R_{\frac{\pi}{2}}\right) e^{jk_0 y \sin \varnothing'} y \quad (2.47)$$

Which results [9]:

$$E_{0,out}^s = z E_0 \left[\left(1 + R_{\frac{\pi}{2}}\right) \cos \varnothing - \left(1 - R_{\frac{\pi}{2}}\right) \cos \varnothing' \right] \frac{e^{-\frac{j\pi}{4}} F_t[2k_0 \rho \cos^2(\frac{(\frac{3\pi}{2} - \varnothing) \mp (\frac{3\pi}{2} - \varnothing')}{2})]}{2\sqrt{2\pi k_0} \cos(\frac{3\pi}{2} - \varnothing) + \cos(\frac{3\pi}{2} - \varnothing')} \frac{e^{jk_0 \rho}}{\sqrt{\rho}} \quad (2.48)$$

From the above equation, the + sign applies when $\frac{\pi}{2} < \varnothing < \frac{3\pi}{2}$ whereas the - sign is used when $0 < \varnothing < \frac{\pi}{2}$. In regards to the inner region, it follows the same steps as the outer region [9]. The total field result of the UAPO solution from the proposed paper is shown in Figure 2.11.

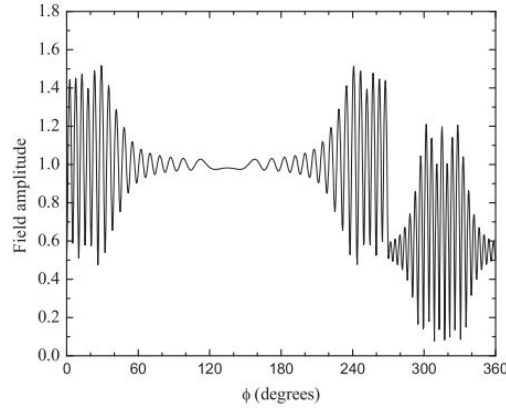


Figure 2.11: Total field by UAPO method [9]

2.10 The Reaction Theorem

The importance of the reaction theorem will become apparent in section 6.5 and onwards where it is used to evaluate the total field on the surface. The reaction theorem is simplified in order to allow the fields of one location to be used in calculation of the mutual impedance in the other location [122]. Reciprocity theorems are listed amongst the most useful methods to solve in field and circuit problems [123]. It can be classified into three types: pure circuit, pure field and mixed. The theorem of the first type (pure circuit) can be expressed in the form:

$$V_{12}I_{11} = V_{21}I_{22} \quad (2.49)$$

Where $V_{12}I_{12}$ are the voltage and current that are transmitted from antenna (source) 1 to antenna (source) 2 and $V_{21}I_{21}$ are the voltage and current that transmits from antenna 2 to antenna 1. The above equation was developed by Rayleigh for networks and lumped elements and was extended by Carson for antennas [124]. It can only be applied to a pair of antennas if both of the antennas have suitable terminals where current and voltage can be defined.

The second type of the reciprocity theorem (pure field), involves electric field and magnetic field intensities. It was derived by Lorentz in the form of surface integrals as follows [124]:

$$\int_{s1} (E_1 \times H_2 - E_2 \times H_1) ds = \int_{s2} (E_2 \times H_1 - E_1 \times H_2) ds \quad (2.50)$$

Where surfaces s_1, s_2 represent the first and second EM source respectively. This method states that the response of a system to a source is unchanged when source and measurer are interchanged. In addition, the second type of reciprocity theorem also represented by Carson [124] is in the form of the volume integral that involves electric current density and electric field intensity as follows,

$$\int_{v_1} J_1 \cdot E_2 dv = \int_{v_2} J_2 \cdot E_1 dv \quad (2.51)$$

Where v_1 and v_2 include source 1 and source 2 respectively. As the terminal voltage and currents are not involved, the second type reciprocity theorems (pure field) can be applied even when no terminals exist.

The name “reaction” was given to the quantity represented by the integrals that appear on the reciprocity theorems of Carson and Lorentz. It was stated that the reaction of antenna 1 on antenna 2 is equivalent to the reaction of antenna 2 on antenna 1 [124], [125].

3 — Physical optics and ray-tracing approach to scattering by 2D dielectric wedge

3.1 Introduction

In this Physical optics method, the analysis will be taken by giving that if the total field is determined in the exterior or interior boundary of the scatterer, then the diffracted field can also be obtained. The motivation for this is an argument that suggests the effect of the internal induced fields by magnetic or electric current can be replaced on the surface. Hence, the entire internal field is cancelled. Thus, it is straightforward to evaluate the far field by integrating the surface currents effects [126], [127].

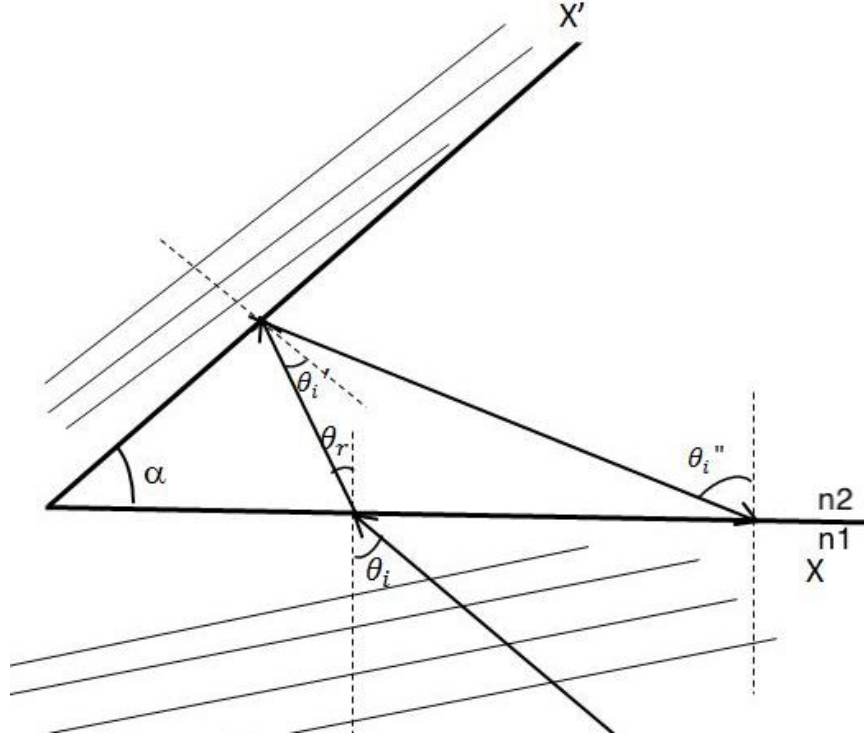


Figure 3.1: Incident wavefronts along the air-dielectric interface

Figure 3.1 shows the incident wavefront along air-dielectric interface. The incident wavefront defines the relationship in the phase among both the air and the dielectric interfaces. The boundary condition here requires that the electric field parallel component is continuous across the boundary. Hence, the field on the interior side of the surface is known. This means that the field that propagates internally is also known until a reflecting surface is known [126], [127].

Since the electric and magnetic fields and flux are known on either side, Fresnel's transmissions and reflection coefficients are obtained. The result is that for each incident plane wave to a wedge, there is a transmitted plane wave with an angle which is given by Snell's

law [126], [127].

$$n \sin \theta = n' \sin \theta' \quad (3.1)$$

where we considered n as the refractive index in the lossless case and hence it is real. It can be said that the Helmholtz wave equation,

$$\nabla^2 \psi - \frac{w^2}{c^2} \psi = 0 \quad (3.2)$$

which has harmonic plane wave solutions as,

$$\psi \propto \exp(j(wt - k.r)) \quad (3.3)$$

Where,

$$k = nk_0 \quad (3.4)$$

From the above equations, ψ is the amplitude, w is the angular frequency, c is the speed of light and k_0 represents the wavenumber of free space. If the problem is considered as 2D, for convenience, then the x-axis is taken along the wedge and y axis is along the normal. Therefore,

$$\sin \theta = \frac{k_x}{|k|} \quad (3.5)$$

Taken with Snell's law, this says – since k scales as n , that the x-components of the wave vectors on either side are equal. These x-components are the Fourier spatial components of the wave along the surface.

3.1.1 Internal diffractive effects

The field in the internal part of the wedge is not infinite in extent. It is limited on one side by the vertex of the wedge and this point can be adopted as a spatial origin. As the incident field can be considered a plane wave with one Fourier component, the actual field that is considered must be multiplied by a step function, the spatial transform is then spread out which accounts as the internal diffraction [126].

3.1.2 Internal field reconstruction

For any wave vector, if the components along the surface are known, the components along the normal direction can also be known. In 2D [126],

$$k_x^2 + k_y^2 = k^2 \quad (3.6)$$

Where: Then the component along the normal can be determined as [126],

$$k_y = \pm \sqrt{n^2 k_0^2 - k_x^2} \quad (3.7)$$

Since the wave is propagating into the medium, the term k_y will be positive solution. When considering k_y in terms of Fourier theory, the general incident field on the interface can be resolved to its Fourier components. By resolving the wavenumber for each component along the surface, the description of the field at all points inside the medium is found when the reflection is not considered. Then, the solution of the field, which propagates successive

reflections, is taken into consideration later.

When the Fourier components along the other side of the wedge are evaluated, the first step of the whole diffraction problem is solved and then the successive wave path between the sides of the wedge can be analysed principally. In order to obtain an efficient solution, the employed Fourier technique, which is used to obtain the FFT, has to have as low dimension as possible. Hence, the iterative form of solution can be obtained. Therefore, the field along the next surface of the wedge can be expressed as that along the previous surface. In principle, the 2D or 3D wavenumbers are exactly the same, it is just that the phases of the each exponential are shifted due to the relative spatial position. Furthermore, when the wave description is reduced to the Fourier components of the surface, there would be a shift in the wavenumber components which is due to the angle of the wedge that is between the two faces [126], [127].

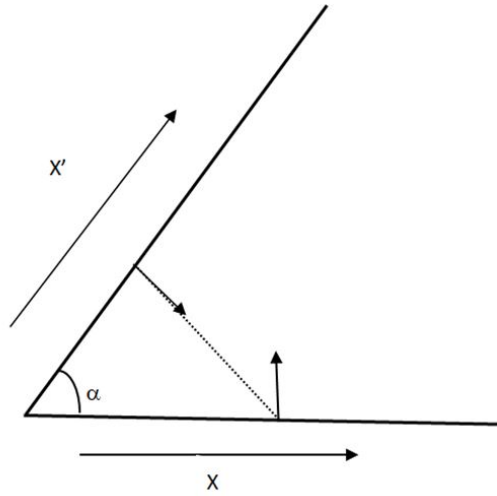


Figure 3.2: The rotation of incident angle by the angle of the wedge

As can be seen from Figure 3.2, the incidence angle is rotated by the angle of the wedge α . If θ is the angle of incidence on the first face then the angle of incidence to the second face is $\theta' = \theta - \alpha$. Then,

$$k'_x = nk_0 \sin \theta' = nk_0 \sin(\theta - \alpha) \quad (3.8)$$

The result comes as a non-uniform shift of the Fourier transform components that are along the previous side of the wedge. The Fourier components in the rotated frame along x' can be obtained by interpolating the components that are evaluated in the x frame.

The above procedure can be continued and it can be expected that there would be a leak in energy at each reflection. The reflected field intensity at each step will decrease progressively such that at some point the remaining reflections can be neglected.

3.1.3 The internal diffractive effects in a lossy medium

If the wedge is considered lossy, the field will get attenuated more quickly which is an advantage. Hence, the field will converge more rapidly. In principle, most of the arguments that are stated earlier in a lossless wedge remain the same. The difference is that the internal refractive index of the wedge is complex. Therefore, the components that are evaluated on the next surface are also complex. This means that the FFT cannot be used directly because that requires real Fourier components. However, the Chirp-Z Transform can be used (CZT). This can be implemented using FFT hence this method is efficient [126].

In this research, the lossless wedge case will be firstly explored. In infrared, ice crystals have a finite but small loss factor. It's effect is likely to be noticeable, particularly when the ice crystals are at least hundreds of wavelengths in diameter.

3.2 Implementation and results of physical optics method

The implementation of the physical optics method was made for a lossless wedge and can be described form Figure 3.1 . When the wave hits the first face of the wedge with an angle θ_i , some of the field will be transmitted with the angle of θ_r and some will be reflected. The angle of transmission θ_r is determined from Snell's law.

$$\sin(\theta_r) = \frac{n_1}{n_2} \sin(\theta_i) \quad (3.9)$$

Then, the angle of incident to the other face (θ'_i), which is normal to the second face of the wedge, is rotated by the wedge angle α . This was found as follows:

$$\alpha + (90 - \theta_r) + (90 - \theta'_i) = 180 \quad (3.10)$$

$$\theta'_i = \alpha + 90 - \theta_r + 90 - 180 \quad (3.11)$$

Therefore,

$$\theta'_i = \alpha - \theta_r \quad (3.12)$$

The same method was used to find the successive angle of incidents for each internal reflection inside the wedge.

$$\theta_i'' = 2\alpha - \theta_r \quad (3.13)$$

$$\theta_i''' = 3\alpha - \theta_r \quad (3.14)$$

\vdots

In regards to the plane wave, each plane wave in the medium has the following representation:

$$k = \begin{pmatrix} k_x \\ k_y \end{pmatrix} = \begin{pmatrix} k \sin \theta \\ k \cos \theta \end{pmatrix} \quad (3.15)$$

where,

$$k = \frac{2\pi}{\lambda} \quad (3.16)$$

and k_x is determined by the spatial frequencies in FFT.

$$|k|^2 = k_x^2 + k_y^2 \quad (3.17)$$

Then,

$$k_y = \sqrt{|k|^2 - k_x^2} = k \cos \theta \quad (3.18)$$

When the field goes to the second face, k_x will be shifted to k_x' and can be found as follows:

$$\theta_i \rightarrow \theta_i' \quad (3.19)$$

$$\sin \theta_i' = \arcsin(\sin \theta_i') \quad (3.20)$$

$$\sin \theta_i' = \arcsin(\alpha - \theta_i) \quad (3.21)$$

Hence,

$$kx' = k' \sin \left(\alpha - \arcsin\left(\frac{kx}{k'}\right) \right) \quad (3.22)$$

where,

$$k' = n_2 k_0 \quad (3.23)$$

It is worth mentioning that when the plane wave enters the wedge, it has to be truncated as the field is only considered not a plane wave itself. Furthermore, the Fresnel equations were used to determine the transmitted field and the reflected field.

3.2.1 Results of the implementation

Suppose a plane wave has a wavelength of $2 \mu m$ and an angle of incidence $\frac{\pi}{4}$ (45°). The truncated wave in the FFT domain is shown in the following figure.

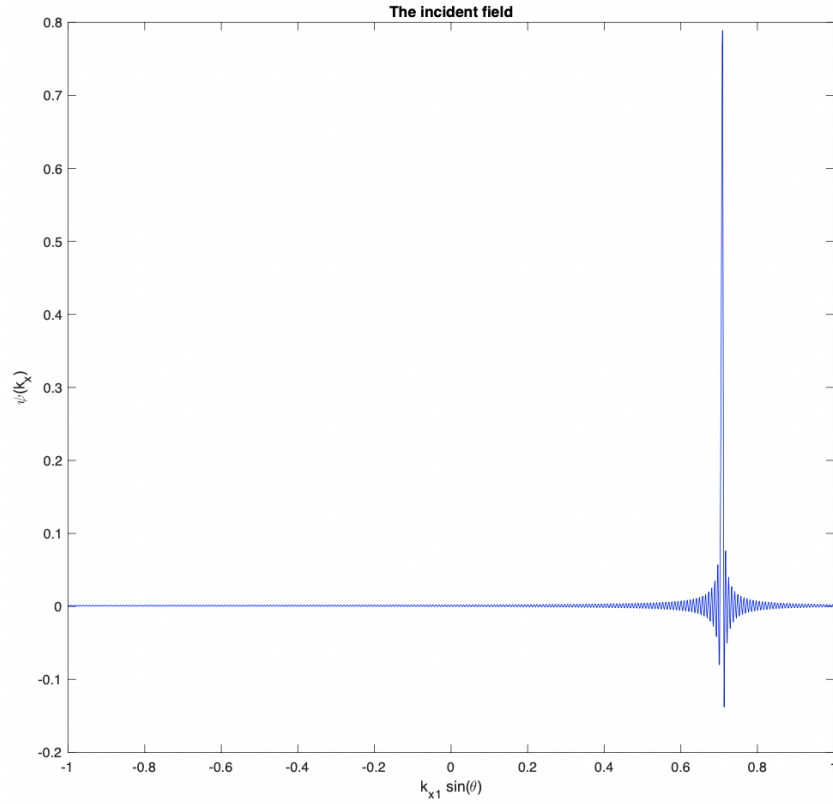


Figure 3.3: The truncated incident field by the wedge

The incident plane wave is travelling from the medium with a refractive index $n_1 = 1$. When the wave hits the first face of the wedge which has a refractive index of $n_2 = 1.33$. Part of the wave is transmitted with the angle (θ_r) and the other part is reflected. The percentage of the transmitted field was calculated by the Fresnel equations. Figure 3.5 shows the transmission coefficients for both parallel and perpendicular case where $n_1 = 1$ and $n_2 = 1.33$.

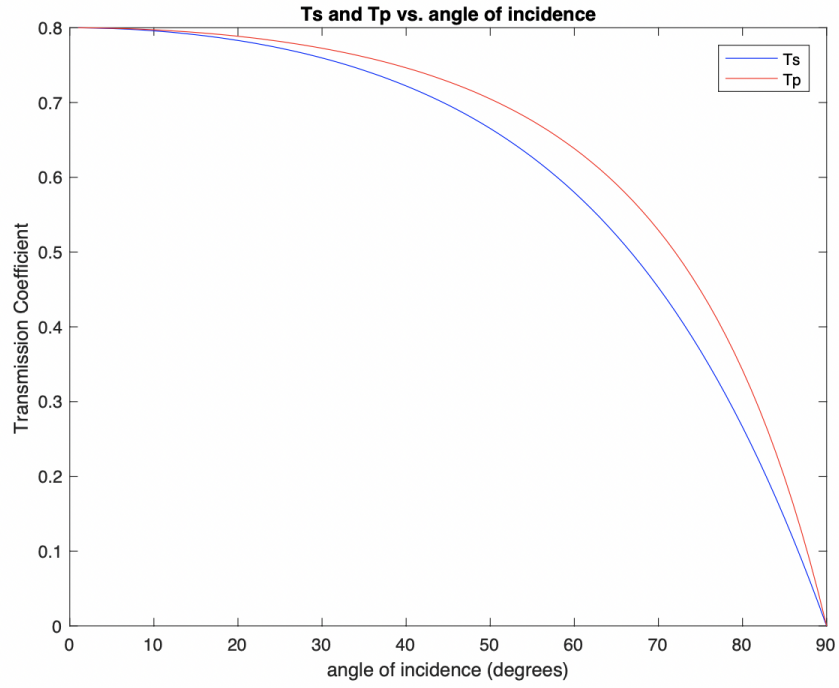


Figure 3.4: The S and P polarisations transmission coefficient vs. the angle when $n_1 = 1$ and $n_2 = 1.33$

The amount of transmitted field (transmittance) can be calculated by the following formula:

$$T = \frac{n_2 \cos \theta_r}{n_1 \cos \theta_i} |t|^2 \quad (3.24)$$

Therefore, the transmitted field from the first face of the wedge in both parallel and perpendicular polarizations is as follows:

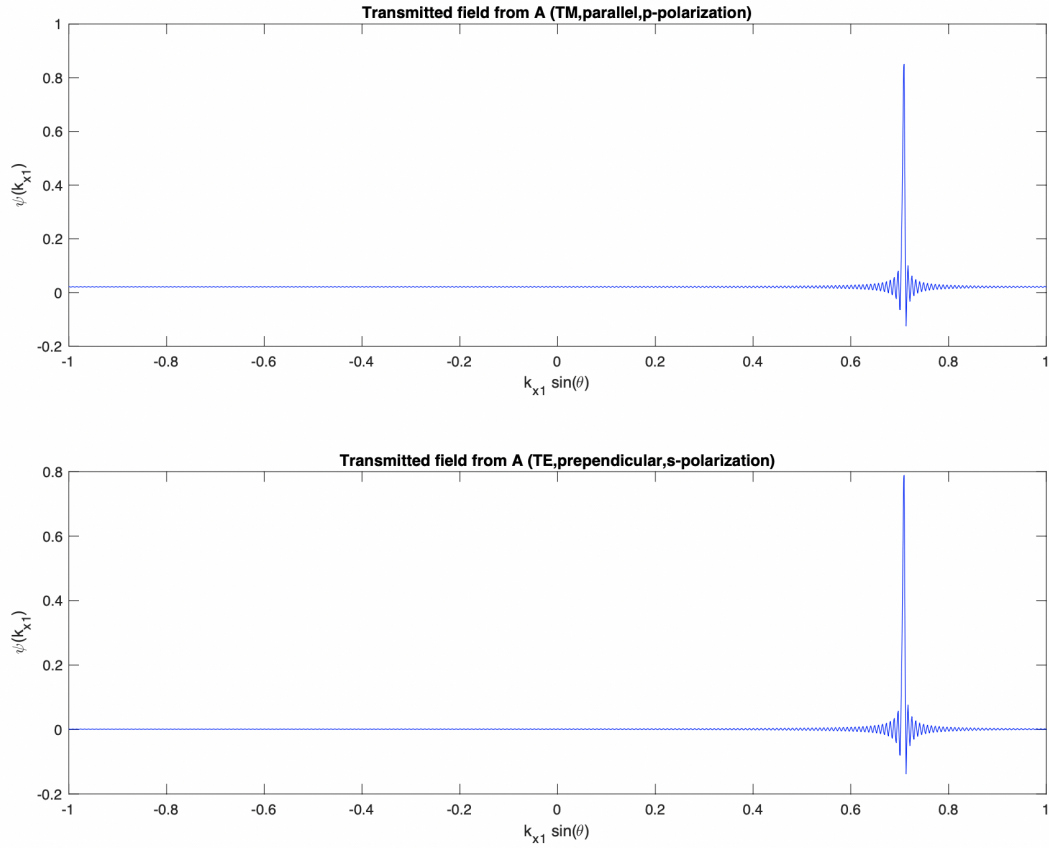


Figure 3.5: The transmitted field from the first face of the wedge

As can be seen from Figure 3.5, the transmitted field of both parallel and perpendicular polarisation are shown. The transmissivity in the parallel case (TM) is 99.73% , whereas the transmissivity is 94.77% in the perpendicular case (TE). Then, the field will shift to the second face of the wedge (face B). The shifted field function was made according to the description in the implementation section. By calling the function, the shifted field, which is at the second face of the wedge, is shown as follows:

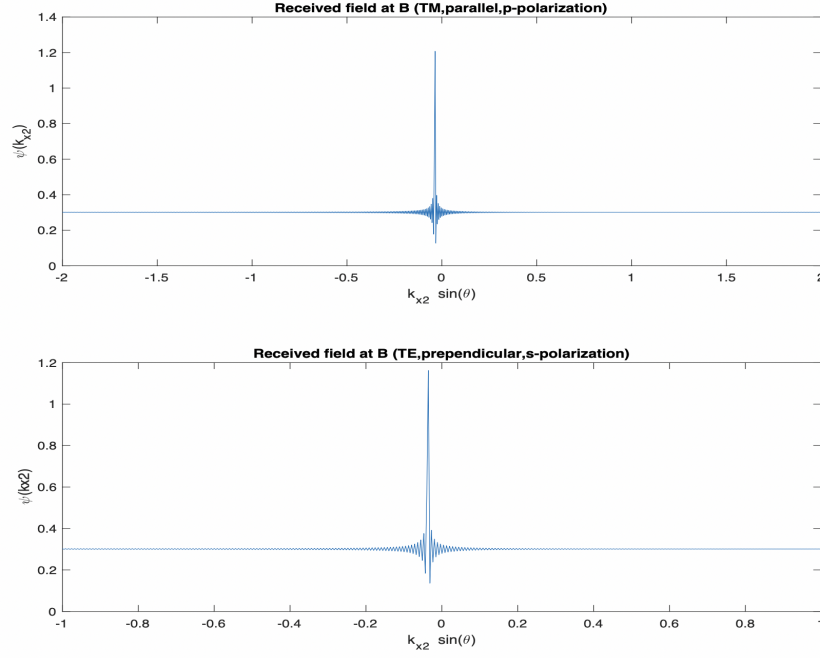


Figure 3.6: Received field at the second face of the wedge

Then, what we are interested in here is to calculate the internal reflections inside the wedge. Therefore, it is important to calculate the internal reflections for each successive bounce (shift) of the internal fields. The first internal reflection was calculated from the second face (B). It was calculated by using the Fresnel equations of reflection. The following description was used to find R_p and the same principle was used for R_s . When calculating the reflections from the inside part of the wedge, the first refractive index $n_1=1.33$ and $n_2=1$ because now the field is inside the wedge.

$$R_p = \frac{n_2 \cos(\theta'_i) - n_1 \cos(\theta'_r)}{n_2 \cos(\theta'_i) + n_1 \cos(\theta'_r)} \quad (3.25)$$

where,

$$k_x'' = n_1 \sin \theta'_i \quad (3.26)$$

$$k_y'' = n_1 \cos \theta_i' \quad (3.27)$$

According to Snell's law,

$$\sin(\theta_r') = \frac{n_1}{n_2} \sin(\theta_i') \quad (3.28)$$

Hence, it is

$$R_p = \frac{n_2 \cos(\theta_i') - n_1(1 - \frac{n_1}{n_2} \sin(\theta_i'))}{n_2 \cos(\theta_i') + n_1(1 - \frac{n_1}{n_2} \sin(\theta_i'))} \quad (3.29)$$

Therefore, it is

$$R_p = \frac{n_2 \frac{k_y''}{n_1} - n_1(1 - \frac{k_x''}{n_2})}{n_2 \frac{k_y''}{n_1} + n_1(1 - \frac{k_x''}{n_2})} \quad (3.30)$$

The reflectivity of both perpendicular and parallel polarisation with respective angles of incidence is shown in Figure 3.7.

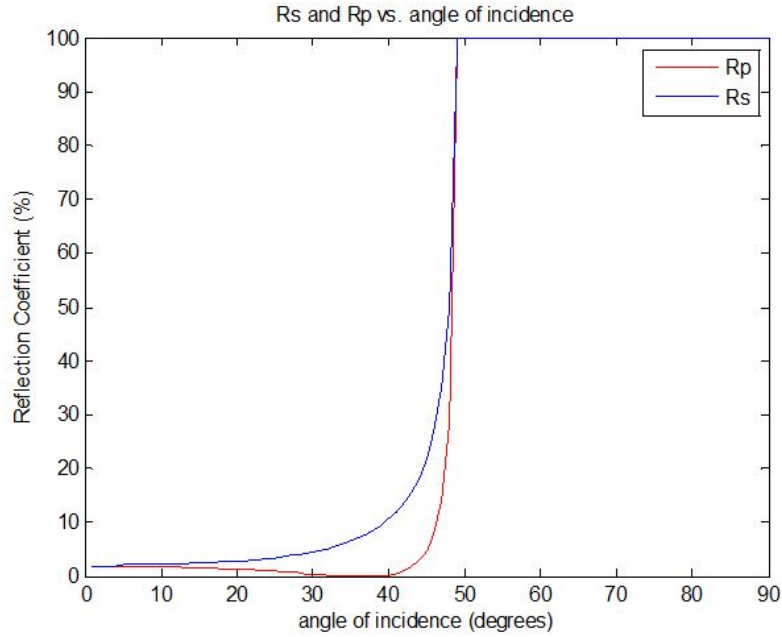


Figure 3.7: Reflection coefficient vs. angle when $n_1 = 1.33$ and $n_2 = 1$

Figure 3.7 shows the amount of field reflected in terms of percentage for both s and p polarization. It shows the critical angle where the field reflection is 100%. Then, the reflection field from the second face of the wedge back to the first face was obtained. The FFT of the reflected field is shown in Figure 3.8.

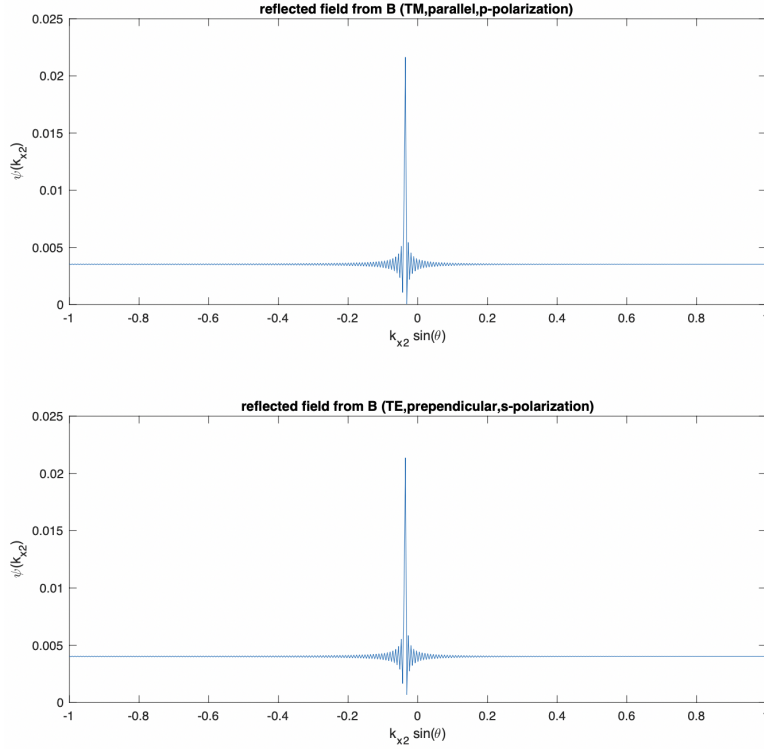


Figure 3.8: The reflected field from the second surface of the wedge (surface B)

Figure 3.8 shows the reflection of the incident field on the second surface of the wedge. It shows that approximately 2% of the total incident field is reflected. Then, the procedure of shifting and reflecting is repeated to find the successive reflected fields to obtain the total field inside the wedge. The total field inside the wedge is the sum of the total field inside. The figures (Fig 3.10 to Fig 3.13) show the successive transmissions and reflections of the fields between the wedge's two surfaces.

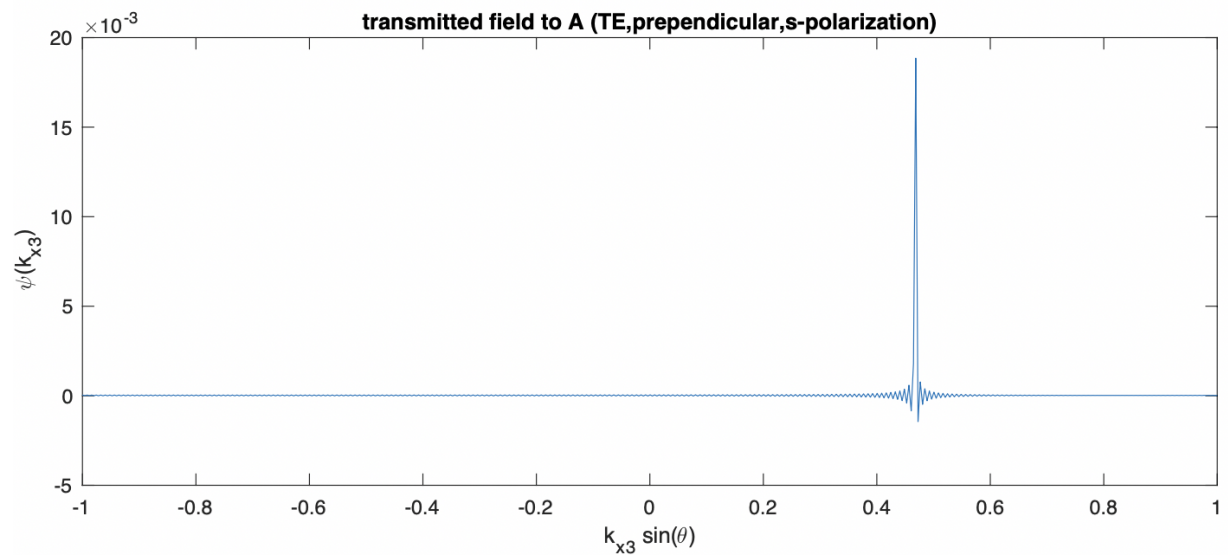
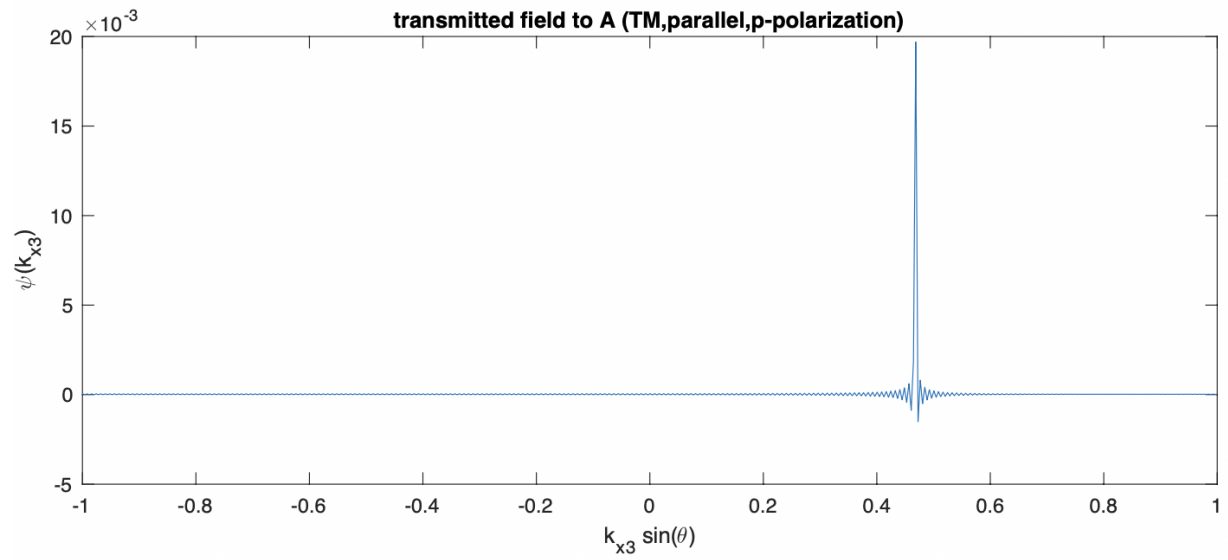


Figure 3.9: Shifted to face A of the wedge

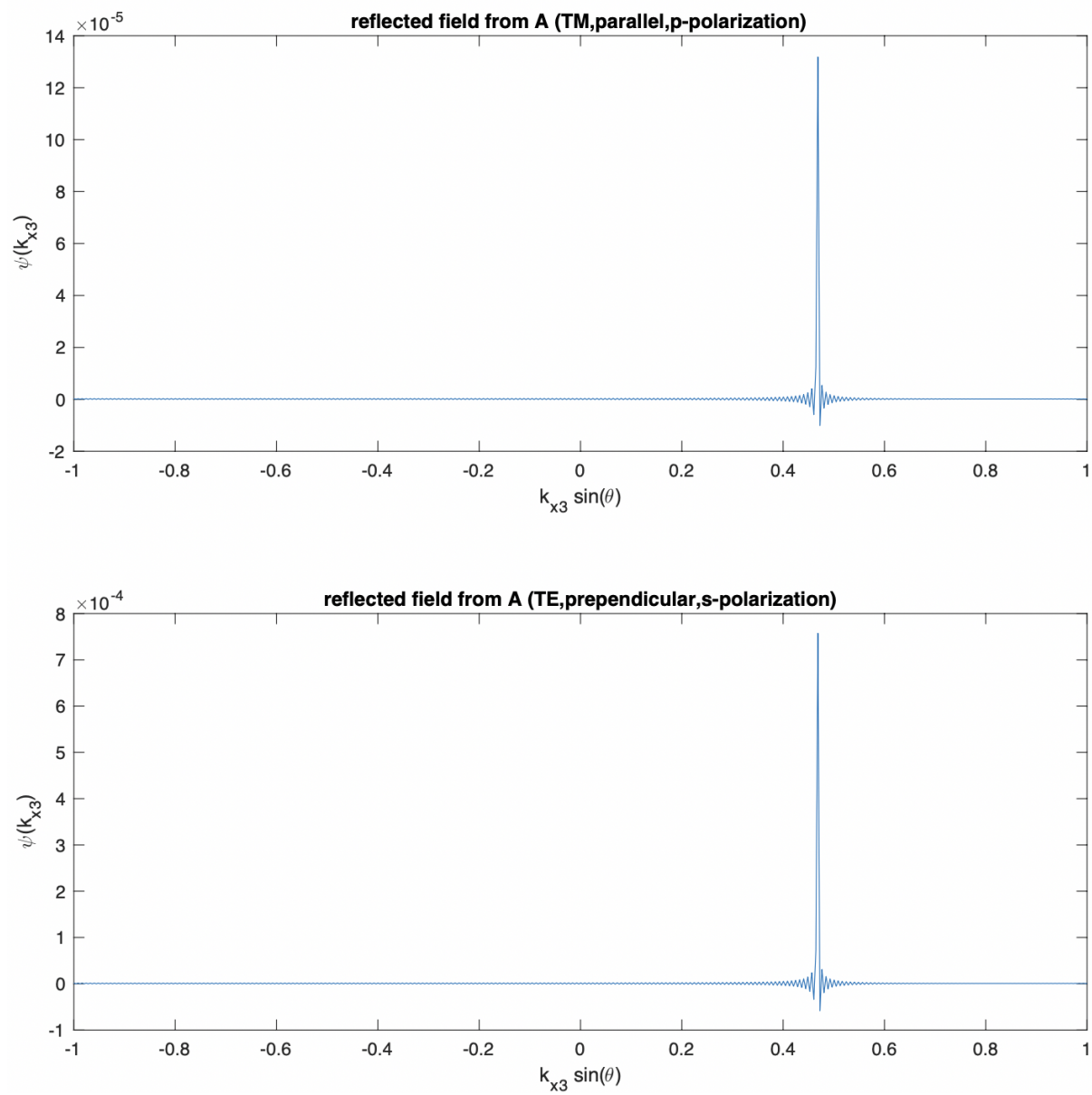


Figure 3.10: Reflected field from face A of the wedge

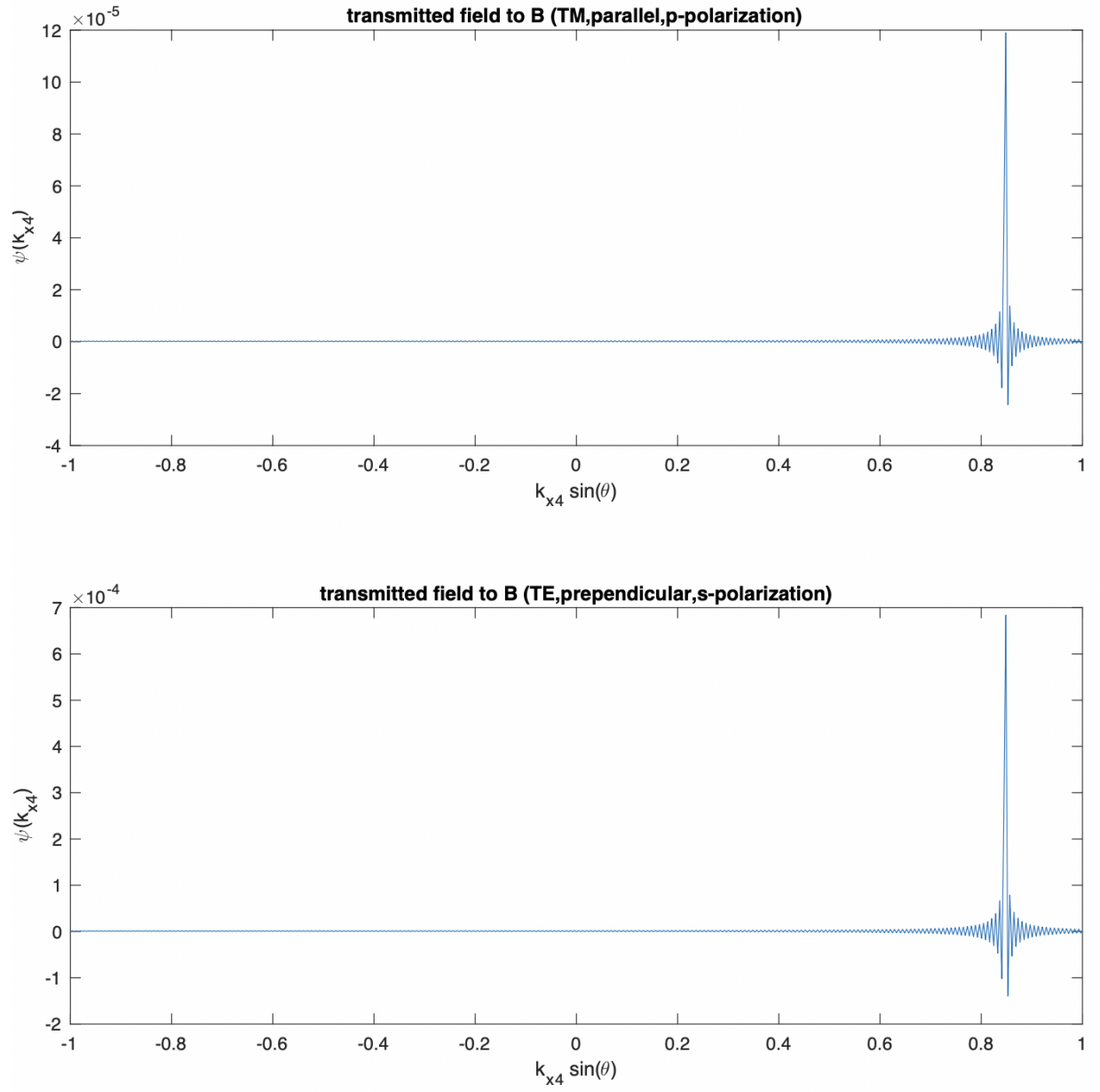


Figure 3.11: The transmitted field to the second surface (face B) of the wedge

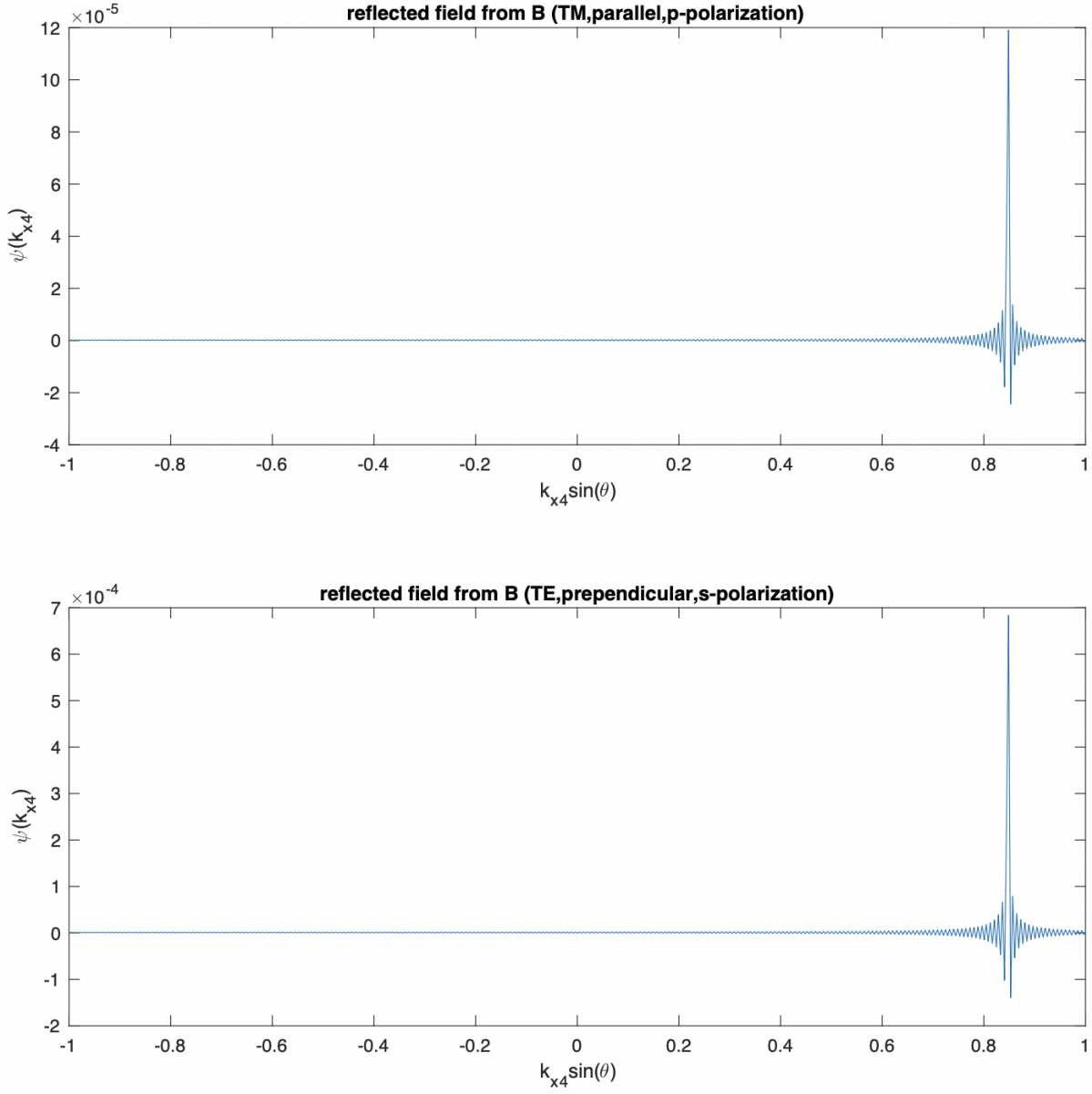


Figure 3.12: Reflected field from the second surface (face B) of the wedge

As can be seen from Figure 3.12, it can be noted that the reflection is by the total internal reflection where the angle of incidence is above the critical angle. From that point, the field will keep reflecting by the total internal reflection along the wedge. Fortunately, the field is very small and it can be neglected when calculating the total field diffracted inside the wedge.

Overall, The figures from Figure 3.8 to Figure 3.12 show the physical optics solution of the total field in multiple reflections inside the wedge. It shows the angular shift on each order of reflection. The angular shift was checked with the ray tracing shifting angles and was observed that there is a match between the angular shifts which proves that the method works. The angular shift was obtained by application of FFT of the field in each reflection.

3.3 Ray-tracing approach to scattering by a wedge

The ray-tracing method was made for scattering by a wedge. The algorithm of the model created and flow chart are shown in the Logarithm 3.1 and Figure 3.13. The result of the model used is shown in Figure 3.14. The parameters that are used for the study is the same parameters used in the physical optics method to compare the results. the parameters used are:

- $n_1=1$
- $n_2=1.3$
- Angle of incidence to the wedge (θ_i) = 45 degrees
- Wedge angle(θ_W) = 30 degrees

The algorithm 3.1 shows a psuedo code of ray-tracing by the wedge which are done by the following steps: firstly, the incident ray slope calculated by giving the angle of incident. then, the refracted angle was calculated using Snell's law. After that, a loop was created for each reflection which includes calculation of the intersection points between the ray and the wedge facets for all reflections. This process is repeated for all ray samples. Also, the algorithm 1 is followed by a flow chart (Figure 3.13) which maps it.

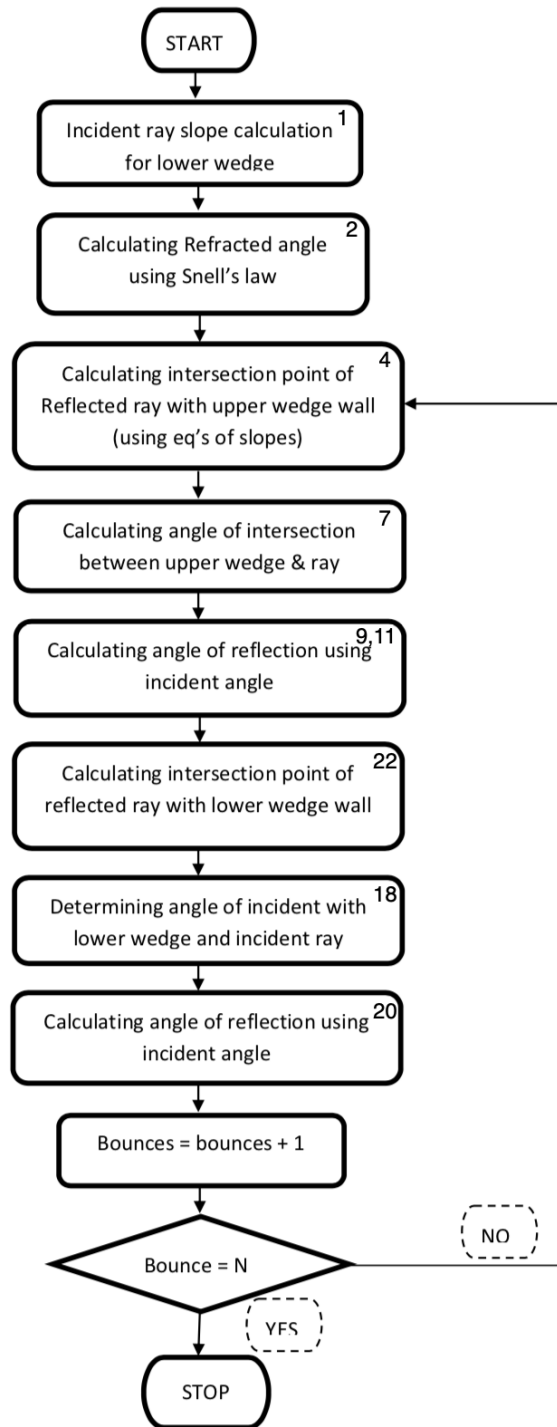


Figure 3.13: Flowchart of the ray-tracing method (the numbers are mapped to the line number in the algorithm used for the implementation)

Algorithm 3.1 The ray-tracing method algorithm

```
1:  $M_i = \tan(\theta_i)$ 
2:  $\theta_r = \arcsin(N1 \times \sin(\theta_i)/N2)$ 
3:  $M_r = \tan(\theta_r)$ 
4:  $PT_i = \text{intersection}(M_r, M_{W1})$ 
5: for  $k = 1 : \text{bounce}$  do
6:    $\theta_{1i} = \arctan(M_r - M_{W2})/(1 + M_r \times M_{W2})$ 
7:   if  $\{\theta_{1i} < 0\}$  then
8:      $\theta_{1i} = |\theta_{1i}|$ 
9:      $\theta_{ir} = -90 + \theta_{1i} - 90 + \theta_W$ 
10:  else
11:     $\theta_{ir} = -\theta_i + \theta_W$ 
12:  end if
13:   $M_r = \tan(\theta_{ir})$ 
14:   $PT_1 = \text{intersection}(M_r, M_{W1})$ 
15:  if  $\{PT_1 < 0\}$  then
16:    break
17:  end if
18:   $\theta_{2i} = \arctan(M_r - M_{W1})/(1 + M_r \times M_{W1})$ 
19:   $\theta_{2i} = |\theta_{2i}|$ 
20:   $\theta_{2r} = \theta_{2i}$ 
21:   $M_r = \tan(\theta_{2r})$ 
22:   $PT_2 = \text{intersection}(M_r, M_{W2})$ 
23:  if  $\{PT_2 < 0\}$  then
24:    break
25:  end if
26:   $PT_1 = PT_2$ 
27: end for
28:  $M_i$  is the slope of the incident ray
29:  $\theta_i$  and  $\theta_r$  is theta of incident and refracted ray respectively
30:  $PT_1$  is the point of intersection between  $M_r$  and  $M_{W1}$  using the formula  $Y = ax + c$ 
    equation of the first line and  $Y = bx + d$  equation of the second line and therefore:  $x =$ 
     $(d - c)/(a - b)$  and  $y = m * x + c$ 
31:  $M_r$  is the slope of the refracted ray
32: bounce is the number of bounces (reflections)
33:  $N1$  and  $N2$  are the refractive indices of medium
34:  $M_{W1}$  and  $M_{W2}$  are the slopes of lower and upper wedge facets
35:  $\theta_{1i}$  and  $\theta_{1r}$  is the ray incident angle to the wedge and the reflected respectively
```

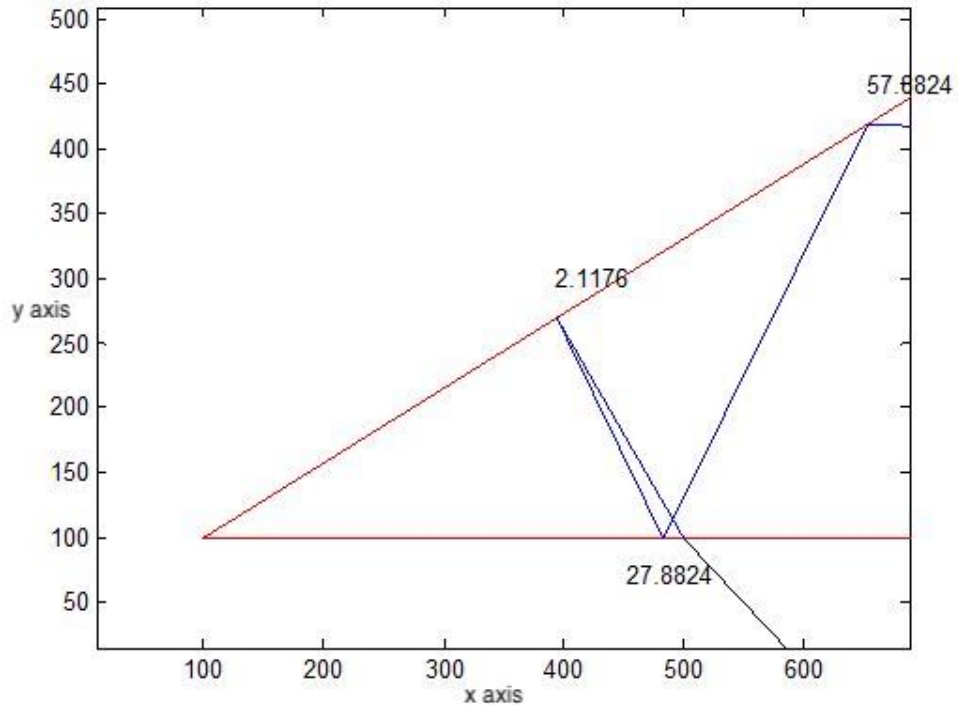


Figure 3.14: Result of the ray tracing method by the dielectric wedge

From Figure 3.14, it can be noted that the angle of incidence, which are to the normal of the wedge surfaces, are the same to the shifted field, that is in the physical optics method (see $\sin(\theta)$ of the field representation at each bounce). It proves that this method is valid for studying the scattering by ice crystals. In summary, this section provides the proof of that the PO is valid by comparing the PO solution of each reflection with ray tracing. The wedge problem was the first step towards achieving PO solution of different ice crystal shapes.

4 — 2D physical optics and ray-tracing approach to scattering by a prism

4.1 Methodology and implementation

The ray-tracing and physical optics method that is used for the prism follows the same principle discussed for the wedge. The difference is that the prism is a closed shape and has one more facet. Therefore, the refracted reflected rays inside will have different directions within the three facets. The ray-tracing is used to track the ray per sample and to map the direction within a number of reflections. The data of the ray-tracing result is stored in addition to Fresnel coefficients. The stored data contributes in FFT shift function as each sample of the ray is tracked, as well as the amount of field reflected from each reflection of the ray inside the prism. The implementation of the ray-tracing and physical optics methods is summarised in the following flow charts which are connected together.

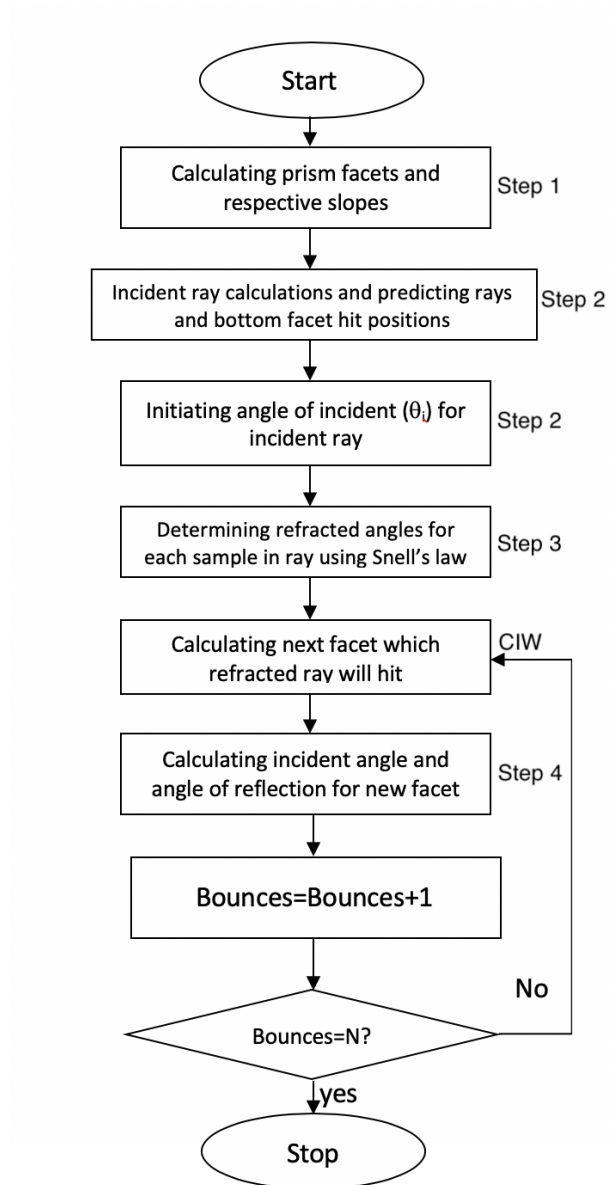


Figure 4.1: Ray-tracing and physical optics by the prism flowchart 1 (the steps are mapped to the algorithm used for the implementation)

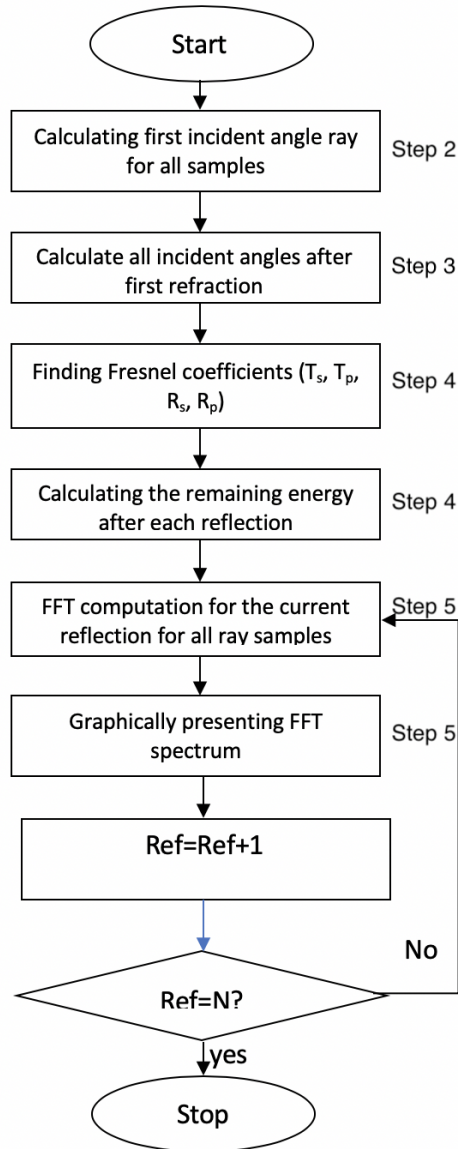


Figure 4.2: Ray-tracing and physical optics by the prism flowchart 2 (the steps are mapped to the algorithm used for the implementation)

The implementation algorithm of ray tracing and physical optics by the prism is divided into five main steps. These algorithms summarise the implementation of the model. The first step of the implementation is to determine the prism facets and edges where each facet intersects with the others. The algorithm of this step is shown as follows:

Algorithm 4.1 Step 1: Predicting the prism edges and its links

```

1: pos1=[x1 y1]
2: pos2=[x2 y2]
3: m1=tan(0)
4: m2=tan( $\pi/3$ )
5: m3=tan( $2\pi/3$ )
6: c=pos1(y1) - m2*pos1(x1) - equation of the the first line of the prism on the left side
7: d=pos2(y2)-m3*pos2(x2) - equation of the second line of the prism on the right side
8: pos3[x3]=(d - c)/(m1-m2) - the  $x$  coordinate position of the intersection between the
   two lines (top vertex of the prism)
9: pos3[y3]=m1*pos3[x3] + c - the  $y$  coordinate position of the intersection between the
   two lines (top vertex of the prism)

```

As can be seen from the algorithm 4.1, pos₁ and pos₂ are the coordinates of the two bottom vertices of the prism. The upper vertex (pos₃) is determined with the help of slopes and intersections equations. m₁, m₂ and m₃ are the known slopes of three prism facets. c and d are the equations of the lines which represents two sides (line) of the prism.

Algorithm 4.2 Step 2: Generating incident rays

```

1: step=1
2: for i=1 to i=rays number do
3:   xi=pos1[x1] + step*i
4:   rayi={xi,pos1[y1]}
5: end for

```

The algorithm above shows the second step of the model development which is the incident ray generation. The ray variable represents the number of samples of incident rays to the bottom facet of the prism. X_i is the x position of the incident ray at angle θ_i to the bottom

facet. The variable Ray_i hold the positions of the i^{th} incident ray to the bottom facet of the prism. The next step is to compute the refraction of the incident ray and its reflections inside the prism. The algorithm is summarised in algorithm 4.3,

Algorithm 4.3 Step 3: Refraction and reflections of rays

```

1: for i=1 to i=rays number do
2:    $m_{incident} = \tan(\theta_i)$ 
3:    $\theta_r = \sin^{-1}(n_1 * \sin(\theta_i) / n_2)$ 
4:    $m_r = \tan(\pi / 2 + \theta_r)$ 
5:    $N_{w_{no}} = \text{CIW}[\theta_r]$ 
6:   for j=1 to j=ref do
7:      $\theta_{1i} = \tan^{-1}((m_r - m_{w_{no}}) / (1 + m_r m_{w_{no}}))$ 
8:     if  $\theta_{1i} < 0$  then
9:        $\theta_{1i} = |\theta_{1i}|$  &  $\theta_{ir} = \theta_{1i} + \theta_{w_{no}}$ 
10:    else  $\theta_{ir} = -\theta_{1i} + \theta_{w_{no}}$ 
11:    end if
12:     $m_r = \tan(\theta_{ir})$ 
13:     $N_{w_{no}} = \text{CIW}[\theta_{ir}]$ 
14:  end for
15: end for

```

From the above algorithm 4.3, $m_{incident}$ is the slope of incident ray in a particular ray sample. θ_r is the refracted ray angle. m_r is the slope of the refracted ray. $N_{w_{no}}$ is the next facet in which the ray will hit and is determined by the CIW (Crystal Incident Wall) function which calculates the next prism facet (wall) in which the ray will hit within the limits of the prism. ref variable represents the number of reflections used in the model. θ_{1i} is the next incident angle inside the prism and θ_{1r} is the angle of reflection inside the prism. The CIW subroutine is shown in the following algorithm.

Algorithm 4.4 CIW subroutine

```
1: for j=1 to j=rays do
2:   for i=1 to i= $w_{no}$  do
3:      $c = \text{prism}_{pt}(y_i) - (m_{w_{no}} \times \text{prism}_{pt}(x_i))$ 
4:      $d = \text{pos}(y_j) - (m_j \times \text{pos}(x_j))$ 
5:      $X = (d - c) / (m_{w_{no}} - m_j)$ 
6:      $Y = (m_{w_{no}} \times X) + c$ 
7:     if  $X \geq \text{prism}_{pt}(x_i)$  &  $X \leq \text{prism}_{pt}(x_{i+1})$  &  $Y \geq \text{prism}_{pt}(y_i)$  &
        $Y \leq \text{prism}_{pt}(y_{i+1})$  then
8:       inter_wall = i
9:       break
10:    end if
11:  end for
12: end for
```

w_{no} is the number of facets the prism has. $\text{Prism}_{pt}(x_i)$ and $\text{prism}_{pt}(y_i)$ are the positions of i^{th} edge of the prism. $\text{pos}(x_j)$ and $\text{pos}(y_j)$ are the positions of j^{th} ray sample. X, Y represent the predicted intersection points of j^{th} reflection with i^{th} facet. Y_limit represents the maximum limit of Y in which prism edges are. Then, the next step is to compute the Fresnel coefficient to calculate the percentage of field refracted at the incident and the reflected field in the prism. The algorithm 4.5 below demonstrates the steps followed.

Algorithm 4.5 Step 4: Fresnel coefficients calculation

```
1: for i=1 to i=R do
2:   for j=1 to j=ref do
3:      $th_j = R_{ij}(th)$ 
4:      $[r_s \ r_p \ t_s \ t_p] = \text{fresnel}(th_j)$ 
5:   end for
6:    $t_{s_{pow}} = \text{Pow}_I \times t_s$ 
7:    $t_{p_{pow}} = \text{Pow}_I \times t_p$ 
8:    $pow\_s_0 = t_{s_{pow}}$ 
9:    $pow\_p_0 = t_{p_{pow}}$ 
10:  for j=1 to j=ref do
11:     $pow_{sj+1} = r_{s_{powj}} \times pow_{sj-1}$ 
12:     $pow_{pj+1} = r_{p_{powj}} \times pow_{pj-1}$ 
13:  end for
14: end for
```

As can be seen from the above algorithm, R represents the number of ray samples taken in the model. ref is the number of reflections to be taken. $R_{ij}(th)$ is the j^{th} incident angle of the i^{th} ray. Fresnel is a function to compute the transmission and reflection coefficient at given refractive index and angle of incidence. Pow_i is the initial percentage of the field. $t_{s_{powj}}$ and $t_{p_{pow}}$ are j^{th} t_p and t_s which represent the transmission coefficient and computes how much of the field is transmitted as a percentage. $r_{s_{powj}}$ and $r_{p_{pow}}$ are j^{th} r_s and r_p which represent the reflection coefficient and computes how much of the field is reflected as a percentage. Then, the final step is to compute the FFT which follows the same principle as discussed for the wedge.

Algorithm 4.6 Step 5: FFT analysis

```
1: for i=1 to i=ref do
2:   for j=1 to j=R do
3:      $thj = R_{ij}(th)$ 
4:   end for
5:   FFT shift function with the aid of ray tracing results and fresnel coef calculations
6: end for
```

4.2 Results

The ray-tracing and physical optics results were made in a lossless case. The assumptions taken for the model are the angle of incidence to the bottom facet of the prism ($\Theta_i=50^\circ$), the refractive index outside the prism ($n_1=1$), and the refractive index of the prism ($n_2=1.787$). The ray-tracing result and PO results are shown in the following figures.

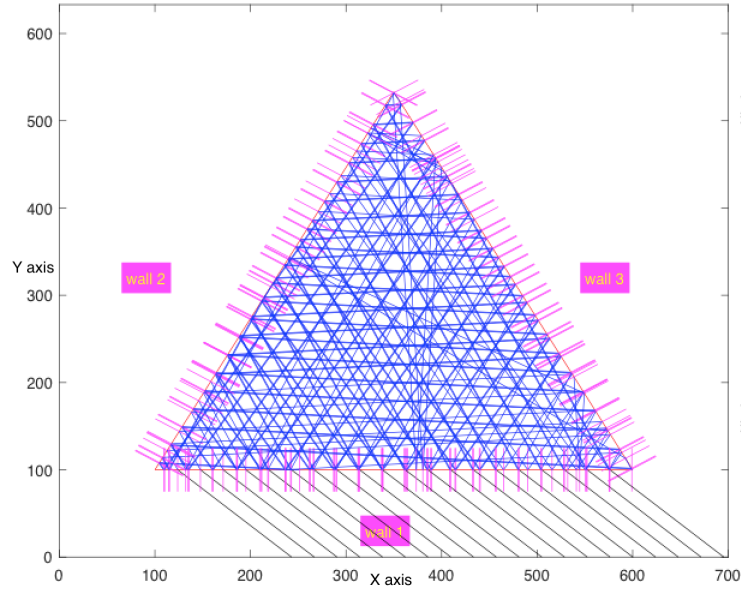


Figure 4.3: Result of the ray-tracing method for the prism

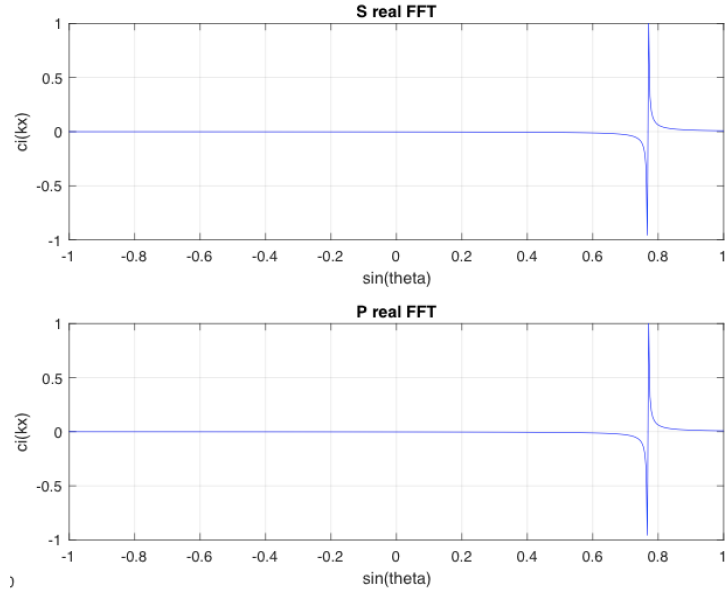


Figure 4.4: PO solution of the total incident field to the bottom facet of the prism

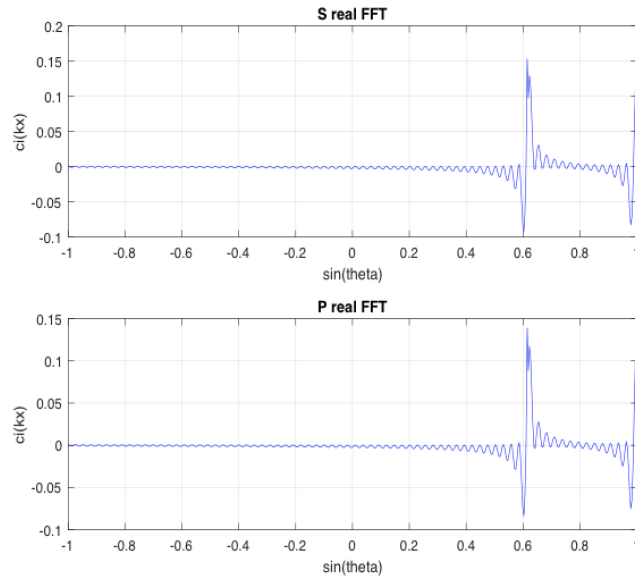


Figure 4.5: PO solution of the total field in the first reflection inside the prism

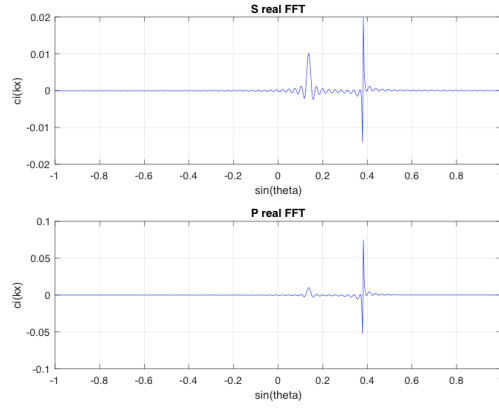


Figure 4.6: PO solution of the total field in the second reflection inside the prism

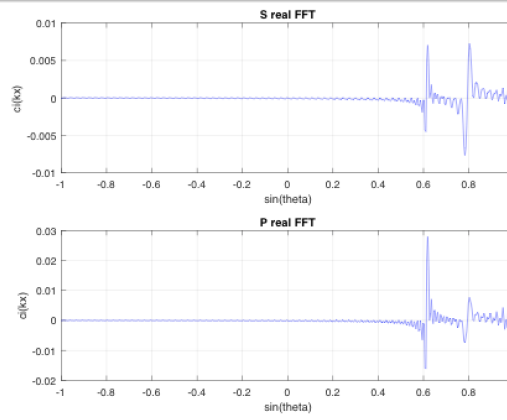


Figure 4.7: PO solution of the total field in the third reflection inside the prism

From Figure 4.3, the ray-tracing solution is presented and the data of each angle of reflection and angle of refraction to the inside the prism is obtained. The figures from Figure 4.4 to Figure 4.7 show the physical optics solution of the total field in first, second and third order of reflection respectively. It shows the angular shift on each order of reflection. The angular shift was checked with the ray tracing shifting angles and was observed that there is a match between the angular shifts which proves that the method works. The angular shift was obtained by application of FFT of the field in each reflection.

4.2.1 Lossy prism analysis

The lossy prism analysis is done by considering the attenuation of the wave due to absorption (imaginary part of the refractive index). The attenuation is directly proportional to the path length that the wave travels inside the ice crystal and here we are considering the prism shape. The average path length computation was done in order to establish the number of reflections which should be considered in this model.

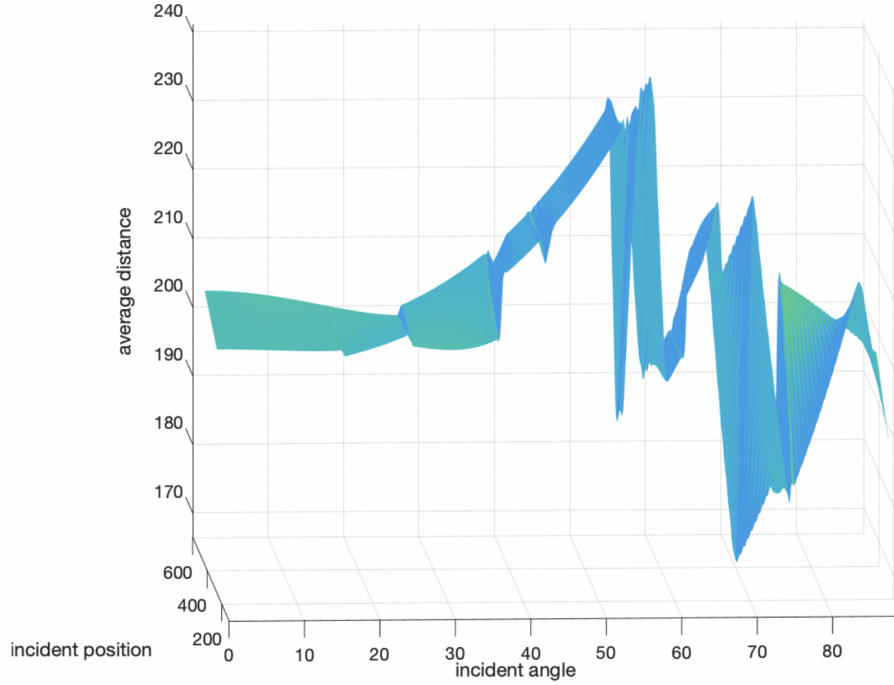


Figure 4.8: Average path length (μm) vs. angle of incidence (degree) vs. position of the incident field angle to the prism

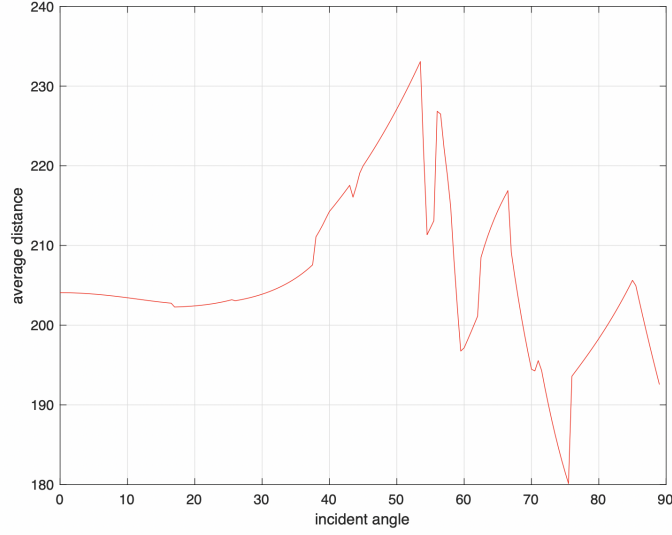


Figure 4.9: Average path length (μm) vs. the incident field angle (degree)

Figure 4.2.1 and Figure 4.9 show the average path length of field per reflection. It shows that the maximum path length is about $225 \mu m$ and the minimum is approximately $196 \mu m$. Therefore, the average attenuation can be calculated as follows,

Considering the propagation factor is $\exp(ik_0nr)$ where r represents the path length. Then,

$$\text{the phase factor} = \exp(in'k_0r) \quad (4.1)$$

where n' is the real part of the refractive index.

$$\text{the amplitude} = \exp(-k_0n''r) \quad (4.2)$$

where n'' is the imaginary part of the refractive index. The attenuation is calculated as

follows,

$$attenuation \ (dB) = 4.6 \ (k_0 r \ n'') \ dB \quad (4.3)$$

By considering $\lambda=1 \text{ um}$ and the imaginary part of the refractive index (n'')= 0.012 according to [90]. The attenuation with the minimum path length is as follows,

$$attenuation \ (dB) = -4.6 \left(\frac{2 \pi}{1 \times 10^{-6}} \times 196 \times 10^{-6} \times 0.012 \right) \approx -68 \ dB \quad (4.4)$$

When the maximum path length is considered, the attenuation becomes,

$$attenuation \ (dB) = -4.6 \left(\frac{2 \pi}{1 \times 10^{-6}} \times 225 \times 10^{-6} \times 0.012 \right) \approx -78 \ dB \quad (4.5)$$

4.3 Green's function method for scattering by a dielectric prism

Green's function is the solution of wave equations (Maxwell's) [122]. In mathematics, the Green's function is the impulse response of the differential equation that is defined in a domain with specified boundary conditions. Through the superposition principle for linear operator problems [128], the convolution of Green's function with an arbitrary function $f(X)$ is the solution of the differential equation for $f(X)$. The linear differential operator Green's function is acting on distributions over a subset of the the Euclidean space at a point s . in any solution of [128]:

$$LG(x, s) = \sum \delta(s - x) \quad (4.6)$$

Where δ stands for the Dirac delta function. Green's function property can be used to solve differential equations of the form [128].

$$Lu(x) = f(x) \quad (4.7)$$

From the above equation, the Green's function is not unique if the kernel of L is non-interval. However, in practice, some combination of boundary conditions and/or other externally imposed criteria will result in a unique Green's function. The Green's function can be categorised by the type of boundary conditions it satisfies. In addition, the Green's functions in general are distributions and are not necessarily proper functions [128].

4.3.1 Implementation of Green's function method for scattering by a dielectric prism

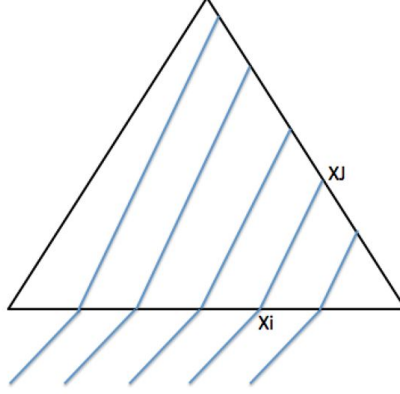


Figure 4.10: propagation of rays from X_i to X_j

As can be seen from the Figure 4.3, the Green's function of the rays travelling from X_{i_i} to X_j can be represented in 2D by the Hankel Function. If X_j on the far wall, and X_i is on the wall with the incident wave [129], [130], then:

$$\psi(XJ) = \int [H_0^1(k_0|X_j - X_i|) \psi(Xi)] dXi \quad (4.8)$$

where ψ represents the amplitude and the term $|X_j - X_i|$ is the distance between each X_j and X_i and calculated by using the distance between two coordinates formula [128]:

$$distance = \sqrt{(y_2 - y_1)^2 + (x_2 - x_1)^2} \quad (4.9)$$

The H_0^1 represents the Hankel function of the first order which is basically a linear combination of the first and second kind of Bessel's functions. Considering the differential

equation [129],

$$z^2 \frac{d^2 y}{dz^2} + z \frac{dy}{dz} + (z^2 - v^2) y = 0 \quad (4.10)$$

The above equation is called the Bessel's equation where v is a real constant. The solutions of the Bessel's equation are known as Bessel's function. $J_v(z)$ and $J_{-v}(z)$ are the basic set of solutions of Bessel's equation for non-integer v . The second solution of Bessel's equation is the Bessel's function of the second kind ($Y_v(z)$) that is independent to $J_v(z)$ and is defined as follows:

$$Y_v(z) = \frac{J_v(z) \cos(v\pi) - J_{-v}(z)}{\sin(v\pi)} \quad (4.11)$$

Hence, the Hankel function can be represented as the linear combination of the first and second kind as:

$$H_v^{(1)} = J_v(z) + iY_v(z) \quad (4.12)$$

$$H_v^{(2)} = J_v(z) - iY_v(z) \quad (4.13)$$

Where $H_v^{(1)}$ and $H_v^{(2)}$ are the Hankel functions of the first and second order respectively.

The coding implementation steps were carried out as shown in Figure 4.3.

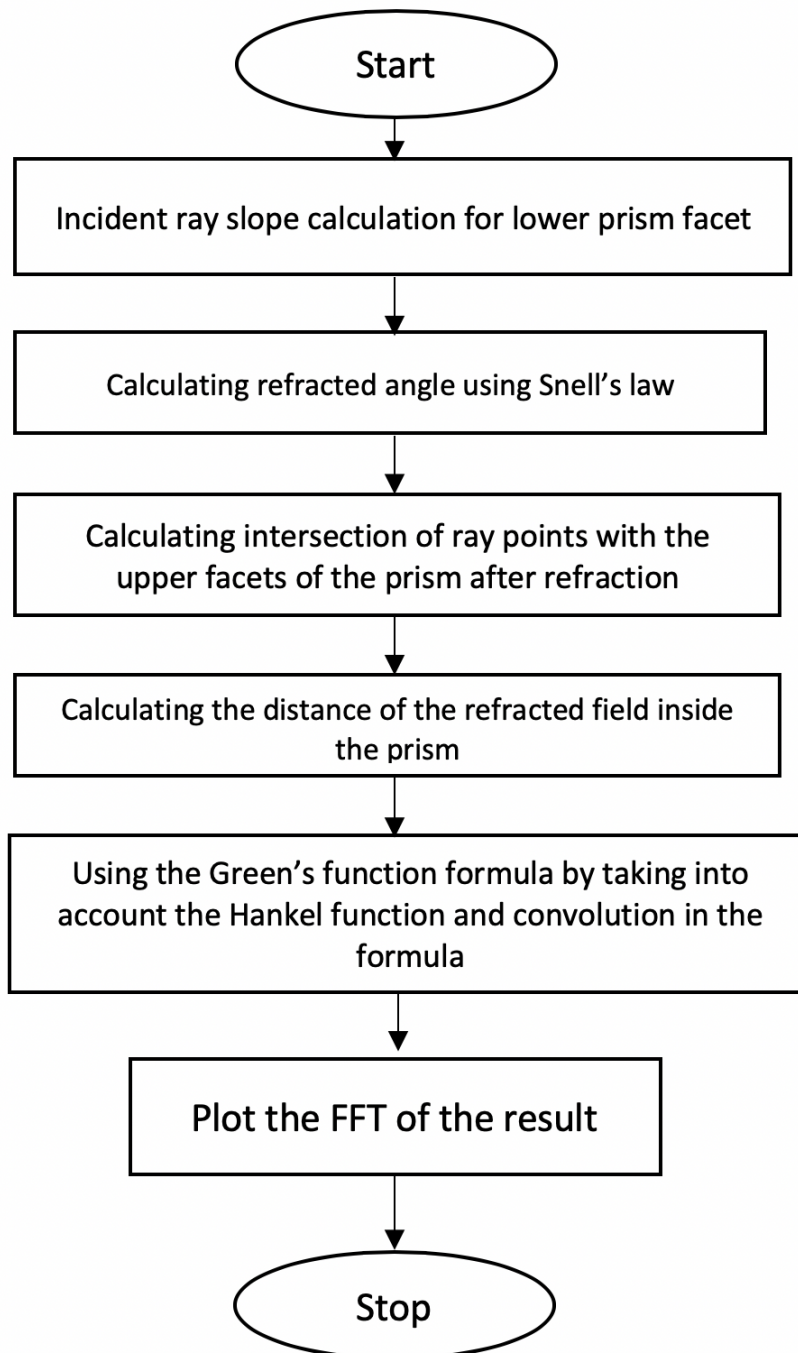


Figure 4.11: Green's function implementation flow chart

The algorithm of the code used was implemented and was as follows:

Algorithm 4.7 Green's function method algorithm

```

1: for j=1 to j=samples do
2:    $Pt_j$ =coordinatesJ %where  $Pt_j$  is the coordinates of intersection in the upper two
   facets
3:    $H=0$  %  $H$  is the whole (Green's function which will be implemented at the end
4:   Total distance=0; %it is the variable which calculates the distance of the refracted
   ray until it intersects with the upper walls.
5:   for  $i = 1$  to  $i$ =samples do
6:      $Pt_i$ =coordinatesI %where  $pt_i$  is the coordinates of the ray samples at the bottom
     wall (at the incidence from the outside)
7:     Distance=sqrt(( $pt_j(1) + pt_i(1)$ )^2 + ( $pt_j(1) + pt_i(1)$ )^2) %distance between two
     coordinates
8:     Total_distance=Total_distance+distance
9:      $A(j)$ =distance( $j$ ) *  $K$ ;
10:  end for
11:   $H(j)$ =conv(besselh(0,1, $A(j)$ ),psi( $j$ )); %Hankel function, bessel function of the third
   kind , psi( $j$ ) is the incident field to the bottom wall
12: end for

```

4.3.2 Results

The result was made by starting the implementation of the ray-tracing to make sure the concept of ray propagation inside the medium was understood. The ray-tracing data was not used for the Green's function and was used only for problem formulation. The ray-tracing result and Green's function were tested at $n_1=1$ and $n_2=1.3$. The angle of incidence was 46 degrees. Hence, the angle of refraction from outside to inside the prism was 32.95 degrees.

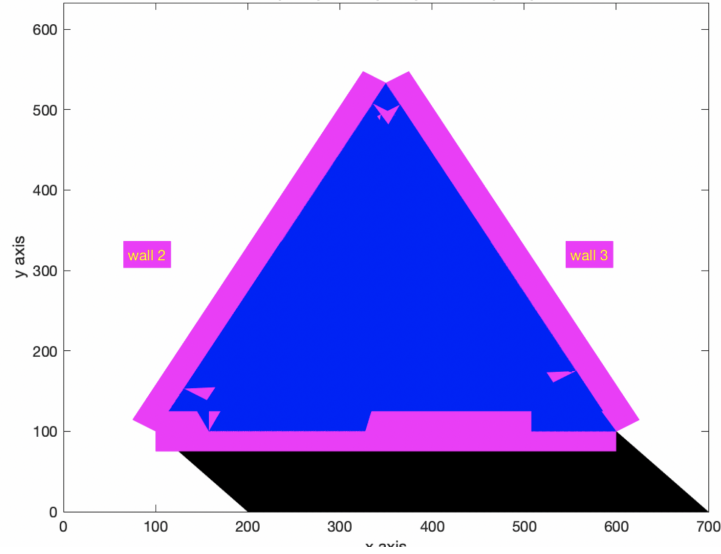


Figure 4.12: Ray-tracing by a dielectric prism

The Figure 4.3 shows the ray-tracing result. The angle of the ray output is shifted by the angle of refraction (angle of the prism on the side wall (wall 2= 60°) -the angle of refraction= 32.96°) = 27.05° . Then, the FFT output was scaled and truncated. In addition, the Fresnel equations were used to compute the transmission coefficients which show the transmitted energy inside the crystal. The FFT output was as follows:

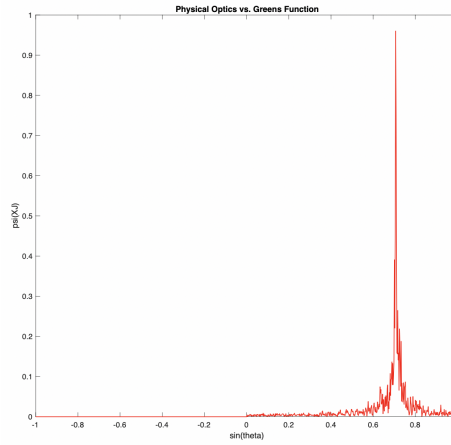


Figure 4.13: FFT of the Green's function for S-polarization

As can be seen from the above, the shifted field has an angle of $\sin(27.05^\circ) = 0.46$ which agrees with the FFT function output of the Green's function shift. For S-polarisation, 95.23% which is nearly 96% of the field is transmitted inside the crystal (prism). The same experiment was made in the P-polarisation case; 99.8% of the field is transmitted inside the crystal as can be seen from the Figure 4.14.

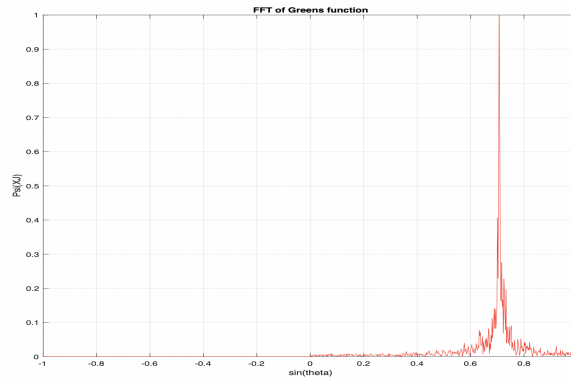


Figure 4.14: FFT of the Green's function for P-polarization

From both figures, it could be concluded that there is a match between the physical optics method and Green's function method as they are both agreeing with the ray-tracing in terms of phase shift.

4.3.3 Comparisons between Physical Optics and Green's Function results

The figures below show the result comparisons between the physical optics and Green's function. The test was taken at $n_1=1$ (outside the prism), $n_2=1.3$ (inside the prism). The angle of incidence from outside the prism is 45° and the angle of refraction is 32.96° . The shift was calculated between the refraction from outside the prism until it hits the second wall and the energy of transmission to the top wall after the first incidence was calculated and displayed in the following figures for both S and P polarisations for both physical optics and Green's function.

From the Figures 4.15 and 4.16, it can be noted that the phase shifts and magnitudes are consistent with each other in both S and P polarisation. It shows that there is an agreement between physical optics and Green's function.

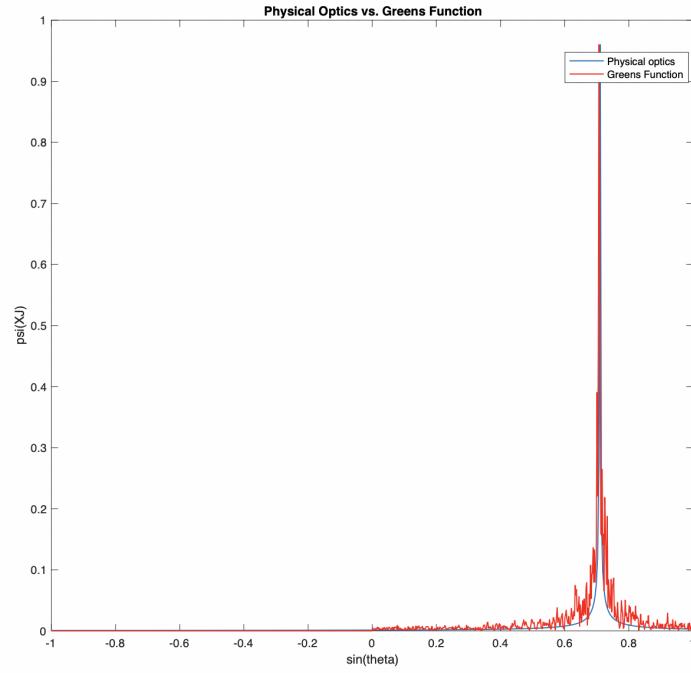


Figure 4.15: Physical optics method vs. Green's function (P-polarisation)

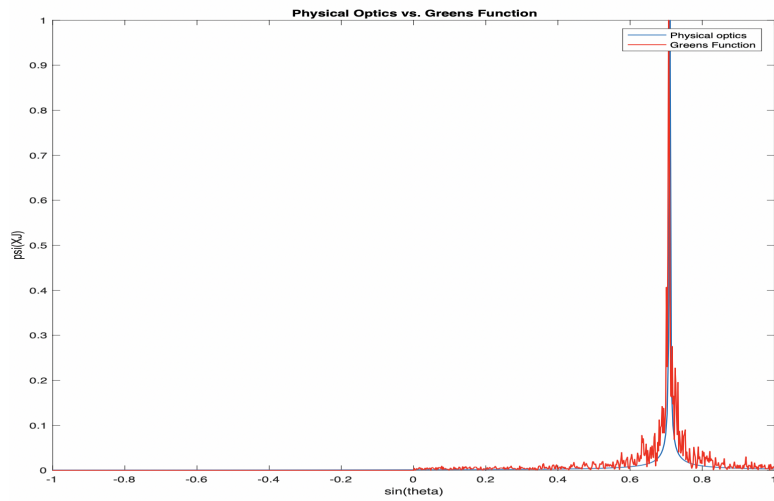


Figure 4.16: Physical optics method vs. Green's function (S-polarisation)

5 — Ray-tracing and physical optics approach to scattering by a 2D Hexagonal form ice crystal

5.1 Methodology

The ray-tracing and physical optics method used for the hexagonal ice crystal follows the same principle discussed for the wedge and prism. The difference is that the hexagonal shape is more complex than the prism as it has more facets. Therefore, the refracted reflected rays inside the hexagon will have different directions within the six facets. The ray-tracing is used to track the ray per sample and to map the direction within a number of reflections. The data of the ray-tracing results are stored in addition to the Fresnel coefficients. The stored data contributes to the FFT shift function as each sample of the ray is tracked as well as the amount of field reflected from each reflection of the ray inside the hexagonal shape ice crystal. The implementation of the ray-tracing and physical optics methods is summarised in the flowcharts in Figures 5.1 and 5.2.

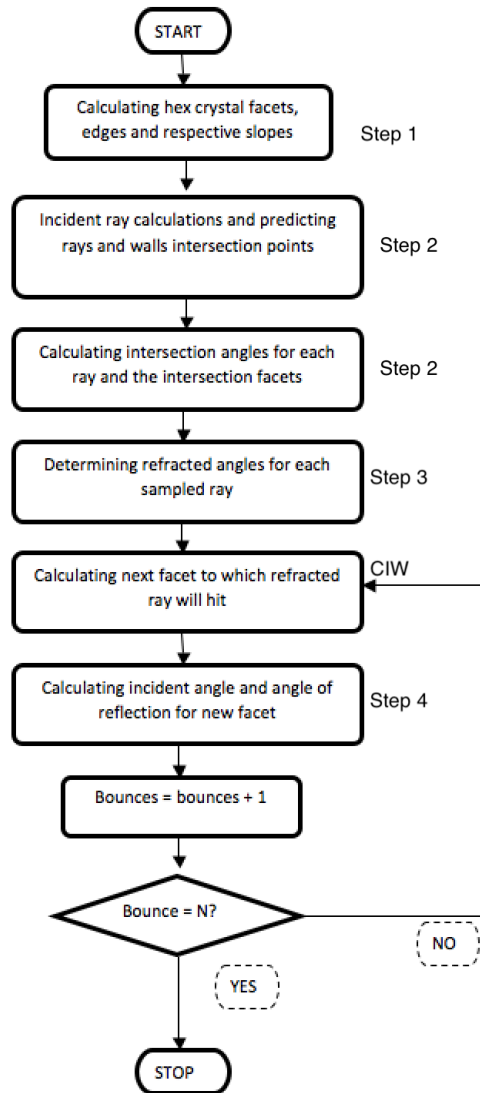


Figure 5.1: Flowchart of the ray-tracing method by the hexagonal ice crystal (the steps are mapped to the algorithm used for the implementation)

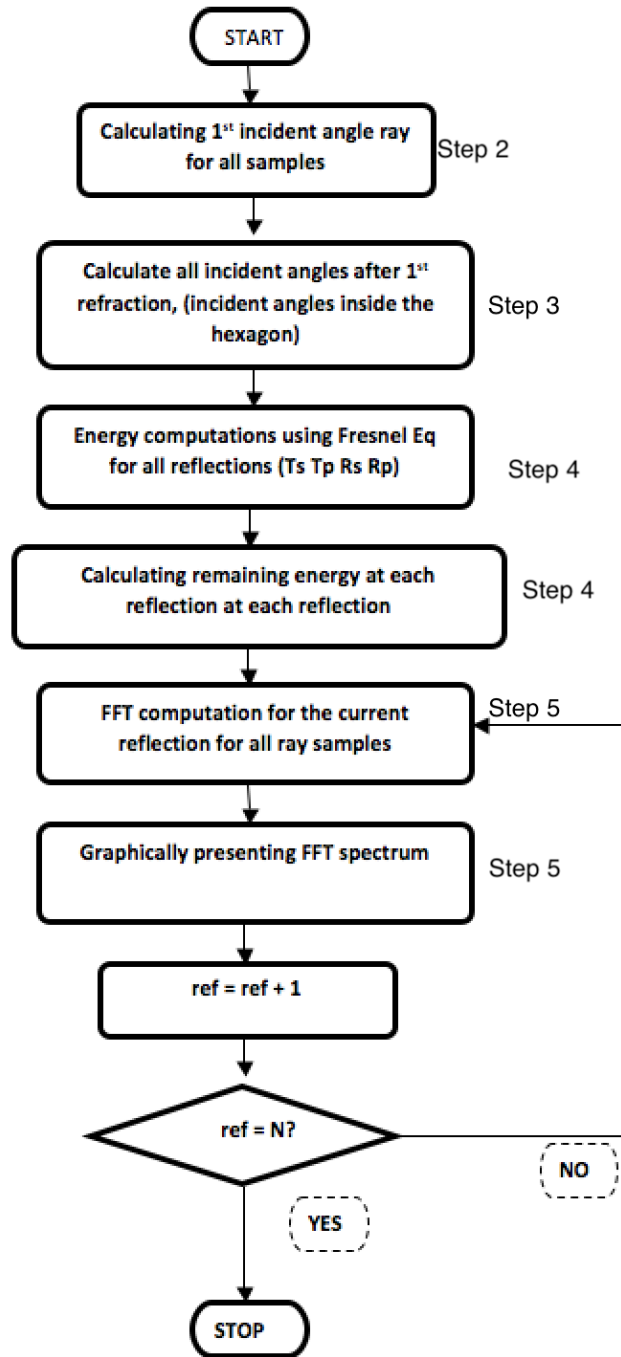


Figure 5.2: Flowchart of PO method by the hexagonal ice crystal (the steps are mapped to the algorithm used for the implementation)

The implementation algorithm is divided into five main steps. These algorithms summarise the model implementation. The first step of implementation is to determine the hexagon facets and edges where each facet intersects with the other. The algorithm of this step is shown as follows:

Algorithm 5.1 Step 1: Predicting hex edges and its links

```

1: for i=1 to i=m-1 do
2:    $X_i = \text{Pos}[\theta_m]_x$ 
3:    $Y_i = \text{Pos}[\theta_m]_y$ 
4:    $X_{i+1} = \text{Pos}[\theta_{m+1}]_x$ 
5:    $Y_{i+1} = \text{Pos}[\theta_{m+1}]_y$ 
6:    $m_i = (Y_{i+1} - Y_i) / (X_{i+1} - X_i)$ 
7:    $\theta_i = \tan^{-1}(m_i)$ 
8:   if  $\theta_i < 0$  then
9:      $\theta_i = \theta_i + 180$ 
10:  end if
11: end for

```

From the Algorithm 5.1, m is the number of edges (facets) in the hexagon. Θ_m is the angle of the m^{th} edge from the hexagonal center position (i.e. $\theta_{1,2,3\dots m} = [0, 60, 120, 180, 240, 300]$). Θ_i and m_i are the angle and slope between the horizontal axis and facet. The next step is to generate incident rays to the hexagonal crystals, which is done as follows,

Algorithm 5.2 Step 2: Generating incident rays

```
1: step=1
2: while rayx < xmax do
3:   c=xmax
4:   d=  $\theta_i$  * rayx
5:   x=(d-c) / tan( $\theta_i$ )
6:   y=x + c
7:   intercept = CIW[tan( $\theta_i$ ),rayx]
8:   if intercept = true then
9:     RAYSk=rayx % where  $k$  is the position of the element in the array starting from
       the first element.
10:     $k = k + 1$ ;
11:   end if
12:   rayx=rayx + step to the next sample
13: end while
```

From the above algorithm, ray_x represents the x th ray sample and x_{max} represents the maximum location of the x axis from where the ray was taken. θ_i is the incident angle with respect to the bottom facet of the crystal. CIW is used here as a function to determine whether the current ray incident sample intersects with any facet in the hexagonal limit. RAYS is the variable which stores all ray samples that will intercept the hexagon. The next step is to calculate the refraction then the reflection angle of the incident ray. The next step algorithm is shown in Algorithm 5.3,

Algorithm 5.3 Step 3: Refraction and reflections of rays

```
1: for i=1 to i=rays do
2:    $m_1 = \text{rays}[w_{no}]$ 
3:    $m_2 = \tan(90 - \theta_i)$ 
4:    $\text{th}_{m_1 m_2} = \tan^{-1}((m_1 - m_2)/(1 + m_1 m_2))$ 
5:   if  $w_{no} > 1$  then
6:      $\text{th}_{m_1 m_2} = 90 - \text{th}_{m_1 m_2}$ 
7:   else
8:      $\text{th}_{m_1 m_2} = \theta_i$ 
9:   end if
10:   $\theta_r = \sin^{-1}(m_1 * \sin(\text{th}_{m_1 m_2})/m_2)$ 
11:   $m_r = \tan(\tan^{-1}(m_{w_{no}}) + \theta_r)$ 
12:   $N_{w_{no}} = \text{CIW}[\theta_r]$ 
13:  for j=1 to j=ref do
14:     $\theta_{1i} = \tan^{-1}((m_r - m_{w_{no}})/(1 + m_r m_{w_{no}}))$ 
15:    if  $\theta_{1i} < 0$  then
16:       $\theta_{1i} = |\theta_{1i}|$  &  $\theta_{ir} = \theta_{1i} + \theta_{w_{no}}$ 
17:    else
18:       $\theta_{ir} = -\theta_{1i} + \theta_{w_{no}}$ 
19:    end if
20:     $m_r = \tan(\theta_{ir})$ 
21:     $N_{w_{no}} = \text{CIW}[\theta_{ir}]$ 
22:  end for
23: end for
```

in the Algorithm 5.3, rays represent the number of ray samples taken in the model. m_1 is the slope for the hex facet represented as w_{no} number. m_2 is the incident ray slope. $\theta_{m_1 m_2}$ is the angle between the facet and the incident ray. θ_r is the refracted ray. m_r is the refracted ray slope. $N_{w_{no}}$ is the next facet that the ray hits after reflection. CIW is the function to check for the next facet the ray sample will hit within the limits of the hexagonal crystal. ref represents the number of reflection needed in the model. $m_{w_{no}}$ is the slope of w_{no} facet. Θ_{ir} is the angle of reflection inside the hexagon.

Algorithm 5.4 CIW subroutine

```

1: for  $j=1$  to  $j=$ rays do
2:   for  $i=1$  to  $i=w_{no}$  do
3:      $c = \text{hex}_{pt}(y_i) - (m_{w_{no}} \times \text{hex}_{pt}(x_i))$ 
4:      $d = \text{pos}(y_j) - (m_j \times \text{pos}(x_j))$ 
5:      $X = (d - c) / (m_{w_{no}} - m_j)$ 
6:      $Y = (m_{w_{no}} \times X) + c$ 
7:     if  $X > \text{hex}_{pt}(x_i)$  &  $X \leq \text{hex}_{pt}(x_{i+1})$  &  $Y >= 0$  &  $Y \leq y_{limit}$  then
8:       inter_wall = i
9:       break
10:    end if
11:  end for
12: end for

```

From the Algorithm 5.4, w_{no} is the number of facets the hexagon has. $\text{hex}_{pt}(x_i)$ and $\text{hex}_{pt}(y_i)$ are the positions of i^{th} edge of the hexagon. $\text{pos}(x_j)$ and $\text{pos}(y_j)$ are the positions of j^{th} ray sample. X and Y represent the predicted intersection points of j^{th} reflection with i^{th} facet. Y_{limit} represents the maximum limit of Y in which the hexagon edges are. Then, the next step is to compute the Fresnel coefficient to calculate the percentage of the field refracted at the incident and the reflected field in the prism. The following steps were taken in the algorithm 5.5.

Algorithm 5.5 Step 4: Fresnel coefficients calculation

```
1: for i=1 to i=R do
2:   for j=1 to j=ref do
3:     thj=Rij(th)
4:     [rs rp ts tp]=fresnel(thj)
5:   end for
6:   tspow=PowI x ts
7:   tppow=PowI x tp
8:   pows0=tspow
9:   powp0=tppow
10:  for j = 1 to j = ref do
11:    powsj+1=rspow x powsj-1
12:    powpj+1= rspow x powpj-1
13:  end for
14: end for
```

As can be seen from the above algorithm, R represents the number of ray samples taken in the model. ref is the number of reflections to be taken. $R_{ij}(th)$ is the j^{th} incident angle of the i^{th} ray. Fresnel is a function to compute the transmission and reflection coefficient at a given refractive index and angle of incidence. Pow_i is the initial percentage of the field. $t_{s_{pow}}$ and $t_{p_{pow}}$ are j^{th} tp and ts which represent the transmission coefficient and computes the percentage of the field that is transmitted. $r_{s_{pow}}$ and $r_{p_{pow}}$ are j^{th} ts and tp which represent the transmission coefficient and computes how much of the field is reflected as a percentage. Then, the final step is to compute the FFT which follows the same principle as discussed for the wedge.

Algorithm 5.6 Step 5: FFT analysis

```
1: for  $i=1$  to  $i = ref$  do  
2:   for  $j = 1$  to  $j = R$  do  
3:      $th_j = R_{ij}(th)$   
4:   end for  
5:   FFT shift function with the aid of ray-tracing results and Fresnel coefficient calculations  
6: end for
```

5.2 Results

The ray-tracing and physical optics results were made in a lossless case. The assumptions taken for the model are the angle of incidence to the bottom facet of the hexagonal ice crystal ($\Theta_i=50^\circ$), the refractive index outside the prism ($n_1=1$) and the refractive index of the hexagonal ice crystal ($n_2=1.787$). The ray-tracing result and PO results are shown in the following figures. Figure 5.3 shows the ray tracing simulation by a hexagonal prism which shows the incident field and the reflected field upto the fourth order of reflection. Figure 5.4 to Figure 5.6 shows the FFT of the field from first order until fourth order of reflection.

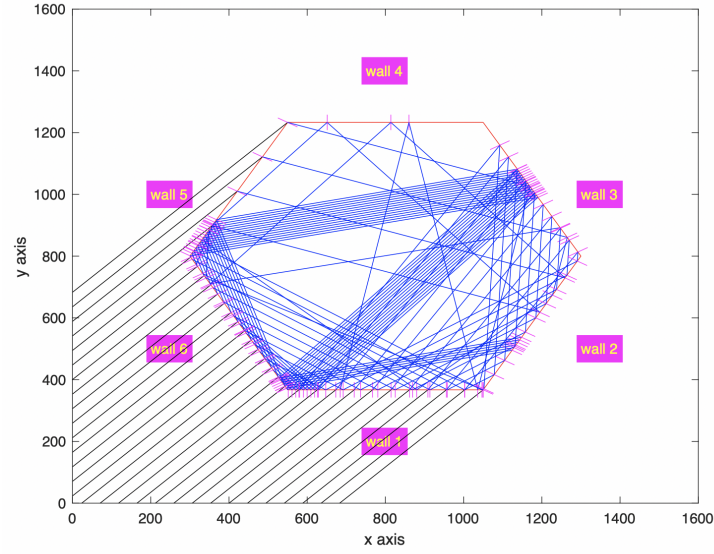


Figure 5.3: Result of the ray-tracing method for the hexagonal ice crystal

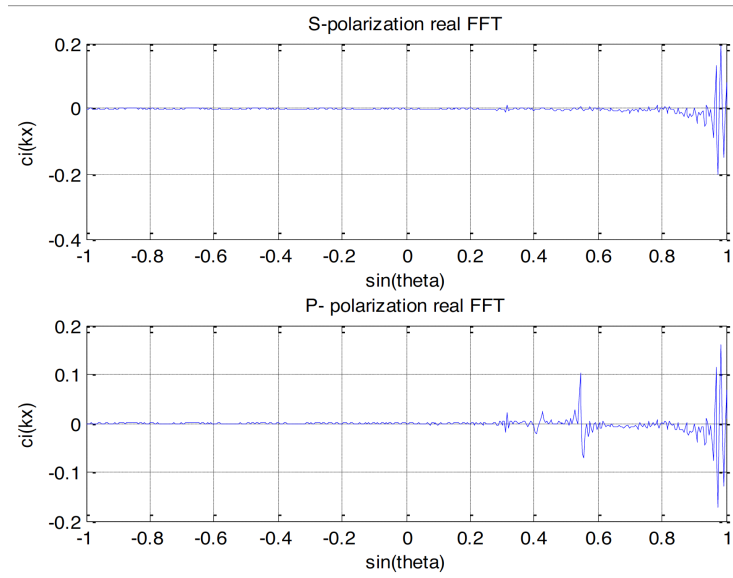


Figure 5.4: PO solution of the total field in the first reflection in hexagonal ice crystal

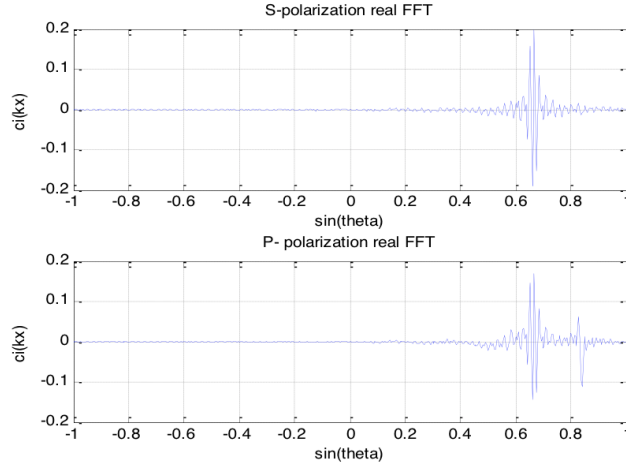


Figure 5.5: PO solution of the total field in the second reflection in hexagonal ice crystal

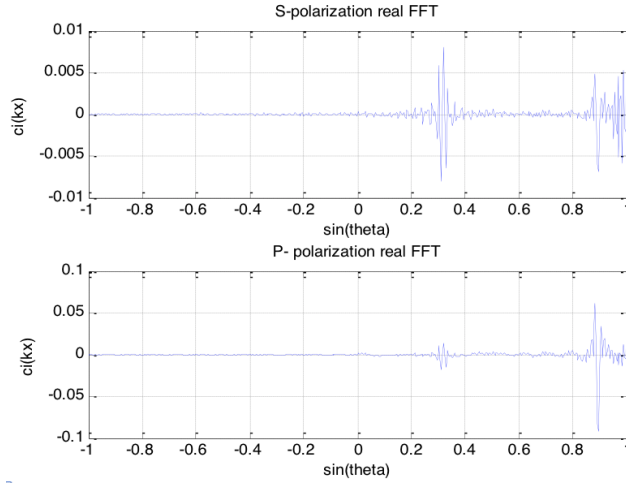


Figure 5.6: PO solution of the total field in the third reflection in hexagonal ice crystal

From Figure 5.3, the ray-tracing solution is presented and the data of each angle of reflection and angle of refraction to the inside hexagon prism is obtained. The figures from Figure 5.4 to Figure 5.6 show the physical optics solution of the total field in first, second and thierd order of reflection repectively. It shows the angular shift on each order of reflection. The angular shift was checked with the ray tracing shifting angles and was observed that there is a match between the angular shifts which proves that the method works.

In summary, this chapter has provided an explanation of the ray-tracing and physical optics method with reference to a two-dimensional hexagon. The ray-tracing and physical optics have a good agreement in terms of phase shift of the field as both agree on the direction of field propagation after successive reflections. The difference between chapter 5 and 4 is that the physical optics and ray-tracing implementation is more difficult in chapter 5 as the hexagon has more facets hence it is more complex to implement than the triangular prism. In the next chapter, the same approach will be employed for solid, three-dimensional ice crystals in order to provide a solution to a scattering problem.

6 — Physical optics and ray-tracing method for scattering by 3D ice crystals

6.1 Introduction to the method

The method explained in the previous chapter is generalised to tackle the problem of scattering by solid ice crystals in three dimensions. The facets of the crystals are considered as planar reflecting surfaces where the Snell's law can be applied. Therefore, we need to apply analytical geometry of three dimensions to determine facet edges as intersections of pairs of planes and vertices. The remainder of this section is concerned with some useful results which are needed for manipulating the geometry of parts of the crystal.

6.1.1 Equation of a plane passing through three points

The equation of a plane passing through three points was used to predict prism wall vectors and constants to get the equation of the walls (planes) [131]. The equation of the plane

that passes through three points is:

$$a(x - x_0) + b(y - y_0) + c(z - z_0) = 0 \quad (6.1)$$

Where x_0, y_0 and z_0 are points in the plane. The vector $\langle a, b, c \rangle$ is perpendicular to the plane. By considering the points that the plane passes through as $P(x_1, y_1, z_1), Q(x_2, y_2, z_2)$ and $R(x_3, y_3, z_3)$ [131]. Then:

$$\bar{v}_1 = \vec{PQ} = ((x_2 - x_1), (y_2 - y_1), (z_2 - z_1)) \quad (6.2)$$

$$\bar{v}_2 = \vec{PR} = ((x_3 - x_1), (y_3 - y_1), (z_3 - z_1)) \quad (6.3)$$

and we have two vectors \bar{v}_1 and \bar{v}_2 sitting in a plane. Hence, the perpendicular vector can be found by simply taking a cross product between \bar{v}_1 and \bar{v}_2 as follows:

$$\begin{vmatrix} i & j & k \\ (x_2 - x_1) & (y_2 - y_1) & (z_2 - z_1) \\ (x_3 - x_1) & (y_3 - y_1) & (z_3 - z_1) \end{vmatrix} \quad (6.4)$$

Hence:

$$\begin{vmatrix} (y_2 - y_1) & (z_2 - z_1) \\ (y_3 - y_1) & (z_3 - z_1) \end{vmatrix} i - \begin{vmatrix} (x_2 - x_1) & (z_2 - z_1) \\ (x_3 - x_1) & (z_3 - z_1) \end{vmatrix} j + \begin{vmatrix} (x_2 - x_1) & (y_2 - y_1) \\ (x_3 - x_1) & (y_3 - y_1) \end{vmatrix} k$$

Therefore: $[(y_2 - y_1)(z_3 - z_1) - (y_3 - y_1)(z_2 - z_1)]i - [(x_2 - x_1)(z_3 - z_1) - (x_3 - x_1)(z_2 - z_1)]j + [(x_2 - x_1)(y_3 - y_1) - (x_3 - x_1)(y_2 - y_1)]k$

$$(z_2 - z_1)]j + [(x_2 - x_1)(y_3 - y_1) - (x_3 - x_1)(y_2 - y_1)]k \quad (6.5)$$

The components of i , j and k represent the perpendicular vector $\langle a, b, c \rangle$

$$[(y_2 - y_1)(z_3 - z_1) - (y_3 - y_1)(z_2 - z_1)]i = a i$$

$$[(x_2 - x_1)(z_3 - z_1) - (x_3 - x_1)(z_2 - z_1)]j = b j$$

$$[(x_2 - x_1)(y_3 - y_1) - (x_3 - x_1)(y_2 - y_1)]k = c k$$

Then, by substituting $\langle a, b, c \rangle$ to the equation of the plane it passes through three points. In addition, by using either P, Q or R coordinates in the equation, the plane equation is implemented. Another method which can be used is that for a parametric equation by giving a directional cosine and a point:

$$P = n(\theta, \phi) + p_0 \quad (6.6)$$

Where n represents a unit vector equivalent to $\langle a, b, c \rangle$. For the bivector form, if p and q are homogenous coordinates of $(1, p_1, p_2, p_3), (1, q_1, q_2, q_3)$ then the bivector is the antisymmetric matrix [131],

$$pq_T - qp_T = \begin{vmatrix} 0 & p_1 - q_1 & p_2 - q_2 & p_3 - q_3 \\ q_1 - p_1 & 0 & q_1 p_2 - q_2 p_1 & q_1 p_3 - q_3 p_1 \\ q_2 - q_1 & q_2 p_1 - q_1 p_2 & 0 & q_2 p_3 - q_3 p_2 \\ q_3 - p_3 & q_3 p_1 - q_1 p_3 & q_2 p_3 - q_3 p_2 & 0 \end{vmatrix} \quad (6.7)$$

6.1.2 Cartesian to polar coordinate conversion

The spherical coordinate system is used to know the direction of ray propagation by giving the incident angles. The spherical coordinate is illustrated in the following figure:

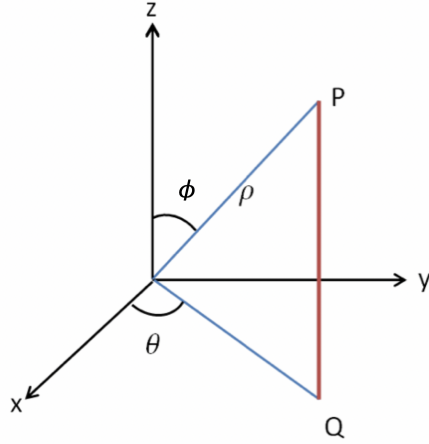


Figure 6.1: Spherical coordinate system

From the figure above, ρ coordinate represents the distance between the segment from the origin P and the origin. Q indicates the projection of P in xy plane. The angle θ is the angle between x -axis and Q . Lastly, the angle ϕ is the angle between z -axis and the segment from the origin P [131]. The spherical coordinates can be represented in terms of Cartesian coordinates as follows:

$$x = \rho \sin\phi \cos\theta \quad (6.8)$$

$$y = \rho \cos\phi \sin\theta \quad (6.9)$$

$$z = \rho \cos\phi \quad (6.10)$$

The above equations were used to calculate and find the direction of rays after refraction and reflections. However, the refraction angle was calculated using Snell's law.

6.1.3 The intersection of a plane with a line

For the ray-tracing method, it is necessary to know the point of intersection to the facets of the crystals of rays. Supposedly we have two points $p(x_0, y_0, z_0)$ and $q(x_1, y_1, z_1)$ where the line passes through these points [131]. The point of intersection with a plane can be found by the following steps: Firstly, the parametric representation of the line has to be found, which is as follows:

$$\bar{r}(t) = (x_0, y_0, z_0) + t(x_1 - x_0, y_1 - y_0, z_1 - z_0) \quad (6.11)$$

Afterwards, the above equation was used to substitute into the plane equation in order to solve it for t . Then, the point of intersection can be found. For instance, if we consider $p(1,0,1)$, $q(4,-2,2)$ and the plane equation is $(x + y + z = 6)$. Then, by using the parametric equation of the line for the two points (p and q) [131], the parametric equation can be rewritten as follows:

$$\bar{r}(t) = (x_0, y_0, z_0) + t(x_1 - x_0, y_1 - y_0, z_1 - z_0) \quad (6.12)$$

$$= (1, 0, 1) + t(3, -2, 1)$$

$$= (1 + 3t, -2t, t + 1)$$

After finding the parametric equation of a line, it can be substituted into the plane wave

equation as follows:

$$x + y + z = 6 \quad (6.13)$$

$$(1 + 3t) + (-2t) + (t + 1) = 6$$

Therefore,

$$t = 2$$

Now plugging t to the parametric equation to get the point of intersection:

$$(1 + 3t, -2t, t + 1) \quad (6.14)$$

Therefore, the point of intersection is:

$$(7, -4, 3) \quad (6.15)$$

The same principle was used to calculate the point of intersection between the prism planes (facets) with the rays.

6.1.4 Fast rotation by orthogonal shearing

In 2D, matrices representing shear operations parallel to an axis are written as,

$$S_x(\lambda) = \begin{pmatrix} 1 & \lambda \\ 0 & 1 \end{pmatrix} \quad (6.16)$$

$$S_y(\mu) = \begin{pmatrix} 1 & 0 \\ \mu & 1 \end{pmatrix} \quad (6.17)$$

Where the first one represents shearing along the x axis by an amount proportional to the y coordinate, as shown in Figure 6.2.

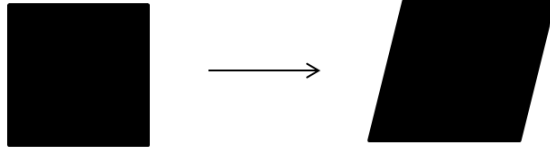


Figure 6.2: Rotation by orthogonormal shearing

In (6.16) and (6.17), λ and μ are the parameters of the respective shears, which make the translation occur in one coordinate only, and be proportional to the other coordinate. For example, in the first case,

$$x' = x + \lambda y \quad (6.18)$$

$$y' = y \quad (6.19)$$

Unlike rotation, reflection and translation, shearing does not preserve shape, but it does preserve area (since the area of a parallelogram is equal to the base times the perpendicular height) [132]. This is clear from the determinant of the matrix, which is always unity regardless of the shear *rates*, λ or μ . What is not so obvious is that a triple product can be combined to produce a rotation matrix. Consider the problem of solving,

$$\begin{pmatrix} 1 & \lambda \\ 0 & 1 \end{pmatrix} \begin{pmatrix} 1 & 0 \\ \mu & 1 \end{pmatrix} \begin{pmatrix} 1 & \lambda \\ 0 & 1 \end{pmatrix} = \begin{pmatrix} \cos \vartheta & -\sin \vartheta \\ \sin \vartheta & \cos \vartheta \end{pmatrix} \quad (6.20)$$

for some arbitrary angle ϑ . Multiplying out the product, this means finding λ and μ such that,

$$\begin{pmatrix} 1 + \lambda\mu & \lambda(2 + \lambda\mu) \\ \mu & 1 + \lambda\mu \end{pmatrix} = \begin{pmatrix} \cos \vartheta & -\sin \vartheta \\ \sin \vartheta & \cos \vartheta \end{pmatrix} \quad (6.21)$$

There are three conditions to be met, but only two variables to solve, so we cannot assume automatically that the problem can actually be solved, because it is possible that we could only satisfy two of the three conditions and the other could be inconsistent. Though it seems surprising, it turns out that there is not a problem and we can always find a solution. The fact that the same matrix is required on each side of the ‘sandwich’ in (6.20) becomes clear as this is necessary to obtain equal diagonal elements [133].

Clearly, to solve (6.20), *necessary* conditions are :

$$\mu = \sin \vartheta \quad (6.22)$$

$$\lambda\mu = \cos \vartheta - 1 \quad (6.23)$$

These equations are easy to solve, but it will also be necessary to establish the value for λ as given by solving the second equation which results in the correct expression for the upper right matrix element as evaluation to $-\sin \vartheta = \mu$. This in fact flows straightforwardly by taking the product of the off-diagonal elements as,

$$\lambda\mu(2 + \lambda\mu) = (\cos \vartheta - 1)(\cos \vartheta + 1) = -\sin^2 \vartheta \quad (6.24)$$

So, if one factor is $\sin \vartheta$ the other is $-\sin \vartheta$. Indirectly, it also follows because the determinant has to be the product of three unit determinants. We can also exploit useful

identities involving trigonometric functions of half angles:

$$\sin \vartheta = 2 \sin \frac{\vartheta}{2} \cos \frac{\vartheta}{2} \quad (6.25)$$

$$1 - \cos \vartheta = 2 \sin^2 \frac{\vartheta}{2} \quad (6.26)$$

$$1 + \cos \vartheta = 2 \cos^2 \frac{\vartheta}{2} \quad (6.27)$$

From these equations, and using (6.22), the second condition, (6.23) immediately gives $\lambda = -\tan(\frac{\vartheta}{2})$. Verifying the consistency of the off-diagonal elements, we have, by substitution,

$$\lambda(2 + \lambda\mu) = -\tan \frac{\vartheta}{2}(1 + \cos \vartheta) = -2 \tan \frac{\vartheta}{2} \cos^2 \frac{\vartheta}{2} = -2 \sin \frac{\vartheta}{2} \cos \frac{\vartheta}{2} = -\sin \vartheta \quad (6.28)$$

So the matrix product (6.24) really *is* a rotation matrix for the correctly chosen values of λ and μ ., something not easy to guess. Note that it is obvious that it is also possible, by similar means, to use a product with different solution values: the same thing, but doing things in a different order like,

$$\begin{pmatrix} 1 & 0 \\ \mu & 1 \end{pmatrix} \begin{pmatrix} 1 & \lambda \\ 0 & 1 \end{pmatrix} \begin{pmatrix} 1 & 0 \\ \mu & 1 \end{pmatrix} = \begin{pmatrix} \cos \vartheta & -\sin \vartheta \\ \sin \vartheta & \cos \vartheta \end{pmatrix} \quad (6.29)$$

6.1.4.1 Application

If we want to rotate an image, moving each pixel by direct rotation is complicated and requires 2D interpolation. The above trick enables the rotation to be achieved by implementing shears in orthogonal directions. In practice, it is better not to try to rotate in this

way by large angles, and this is not a difficult to do it because a 90 degree rotation is trivial, e.g. by transposing an array and reversing one coordinate; so, for example, a 60 degree rotation can be compounded as 90 – 30 degrees. So, it is never necessary to rotate by more than 45 degrees using this process. It is also possible to subdivide the angle, and repeat the whole process. This involves more computation but can mitigate the wrap-around effect, discussed below. The shearing just means that every row or column is translated by a fixed amount proportional to the orthogonal coordinate. This can obviously be achieved by shifting a whole number of pixels and then interpolating by a fractional pixel if the shift is not a whole number of pixels – it is the same for each pixel along the row. But there is also, in theory, a possibly more attractive way, which is to do it in the Fourier domain. This is clear because a uniform shift is formally a convolution of the image with a shifted delta function. It is a basic Fourier theorem that is equivalent in the Fourier domain to multiplying by an exponential with a constant phase gradient:

$$FT(f(x+a)) = F(s) e^{jas} \quad (6.30)$$

One thing to be aware of it is that this operation gives a wrap-around shift – what goes out on the right hand end reappears at the left hand end, so one has to be a little careful to avoid any such aliasing problems; the spatial domain data should be padded at the edges with zeroes. Of course, if the data was going to be Fourier transformed anyway, then to rotate them, the best course is to transform first and then apply the phase factors in the Fourier domain before using them. Since a 2D Fourier transform can be expressed as the product of 1D Fourier transforms, the same reasoning applies to the orthogonal shear, and columns in the spatial Fourier domain.

6.2 Methodology of 3D shape construction and ray-tracing

6.2.1 Facets construction by rotation matrix

Ice crystal shapes consist of facets. These facets can be considered as planes in simulations. For example, the hexagonal prism shape consists of eight facets which can be considered as planes. In order to create each plane, the rotation matrix method was used. In general, the rotation matrix for each access is given by the following formulas:

$$R_x(\theta) = \begin{bmatrix} 1 & 0 & 0 \\ 0 & \cos \theta & -\sin \theta \\ 0 & \sin \theta & \cos \theta \end{bmatrix} \quad (6.31)$$

$$R_y(\theta) = \begin{bmatrix} \cos \theta & 0 & \sin \theta \\ 0 & 1 & 0 \\ -\sin \theta & 0 & \cos \theta \end{bmatrix} \quad (6.32)$$

$$R_z(\theta) = \begin{bmatrix} \cos \theta & -\sin \theta & 0 \\ \sin \theta & \cos \theta & 0 \\ 0 & 0 & 1 \end{bmatrix} \quad (6.33)$$

Based on these matrices, the rotation matrix can be considered with an arbitrary axis and

angle. The following formula shows the rotation matrix with axis \tilde{n} and angle θ .

$$R(\hat{z}, \theta) = \begin{pmatrix} \cos \theta + n_1^2(1 - \cos \theta) & n_1 n_2(1 - \cos \theta) - n_3 \sin \theta & n_1 n_3(1 - \cos \theta) + n_2 \sin \theta \\ n_1 n_2(1 - \cos \theta) + n_3 \sin \theta & \cos \theta + n_2^2(1 - \cos \theta) & n_2 n_3(1 - \cos \theta) - n_1 \sin \theta \\ n_1 n_3(1 - \cos \theta) - n_2 \sin \theta & n_2 n_3(1 - \cos \theta) + n_1 \sin \theta & \cos \theta + n_3^2(1 - \cos \theta) \end{pmatrix} \quad (6.34)$$

In order to create each plane, the above formula was used to set the axis and angles of the plane. In regards to the axis, the z-axis was set. Therefore, the rotation matrix that was used to obtain the planes is as follows:

$$R(\hat{z}, \theta) \equiv \begin{pmatrix} \cos \theta & -\sin \theta & 0 \\ \sin \theta & \cos \theta & 0 \\ 0 & 0 & 1 \end{pmatrix} \quad (6.35)$$

In addition, the angles that the planes follow in the hexagonal prism are given in the table below:

Table 6.1. Angles around z-axis for plane 1 to 6 of the hexagonal prism.

Plane	1	2	3	4	5	6
Angle	-120	-60	0	60	120	180

For planes 7 and 8, we set x-axis as a rotation axis and 90 and -90 degree.

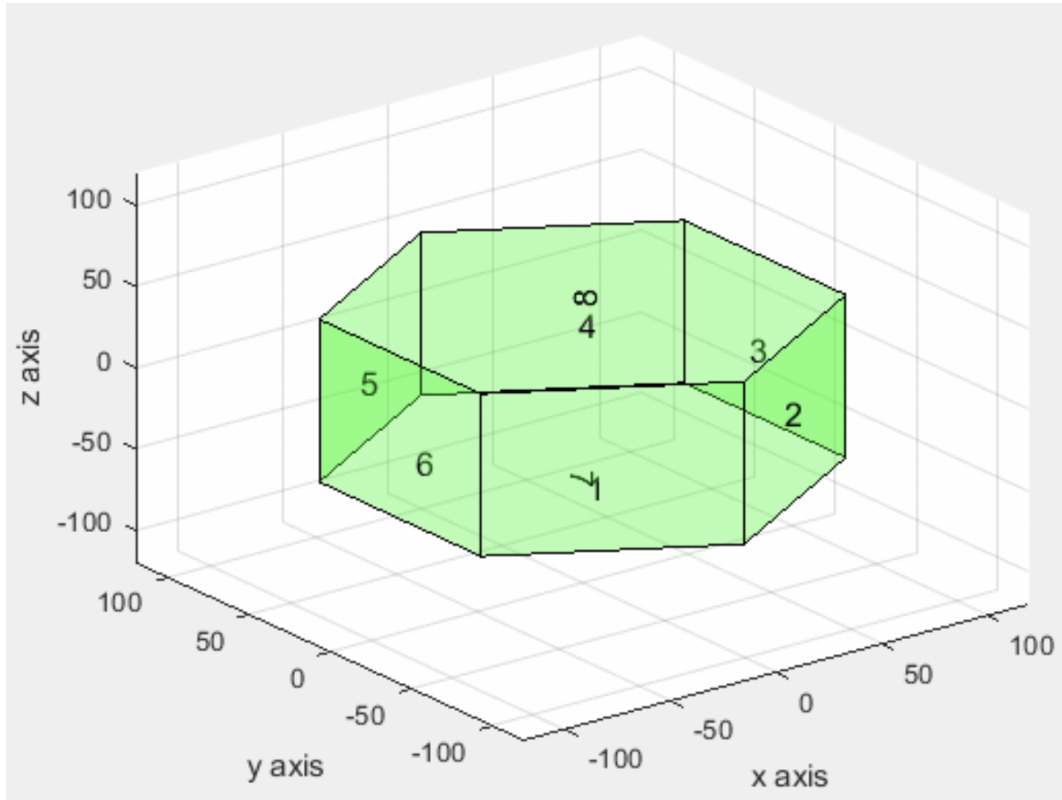


Figure 6.3: labelling the facets of the hexagonal prism shape

Similarly, when the prism and bullet shapes are considered as can be seen from the Figures 6.4 and 6.5.

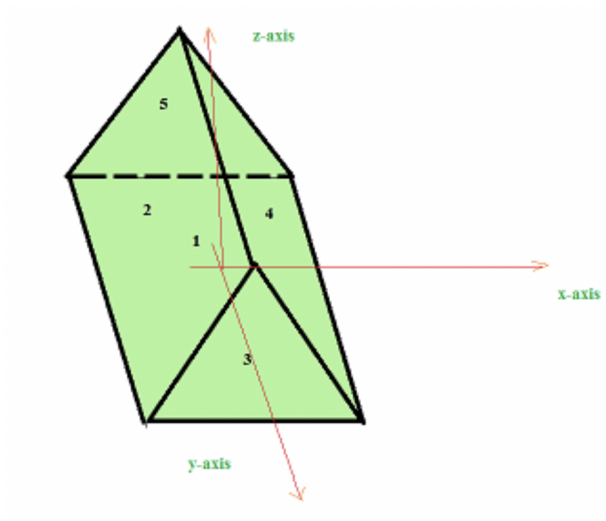


Figure 6.4: Triangular prism facets

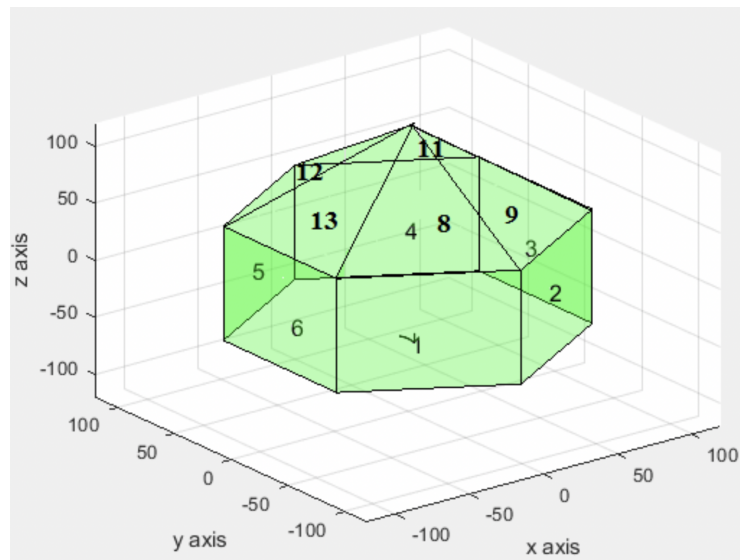


Figure 6.5: Labelling bullet crystals facets

More detailed information regarding the facets construction by rotation matrix can be found in appendix 8.1.

6.2.2 Refraction and reflection

According to Snell's law, the rotation matrix is used in the calculation of reflections for each incident ray. Figure 6.6 shows Snell's law.

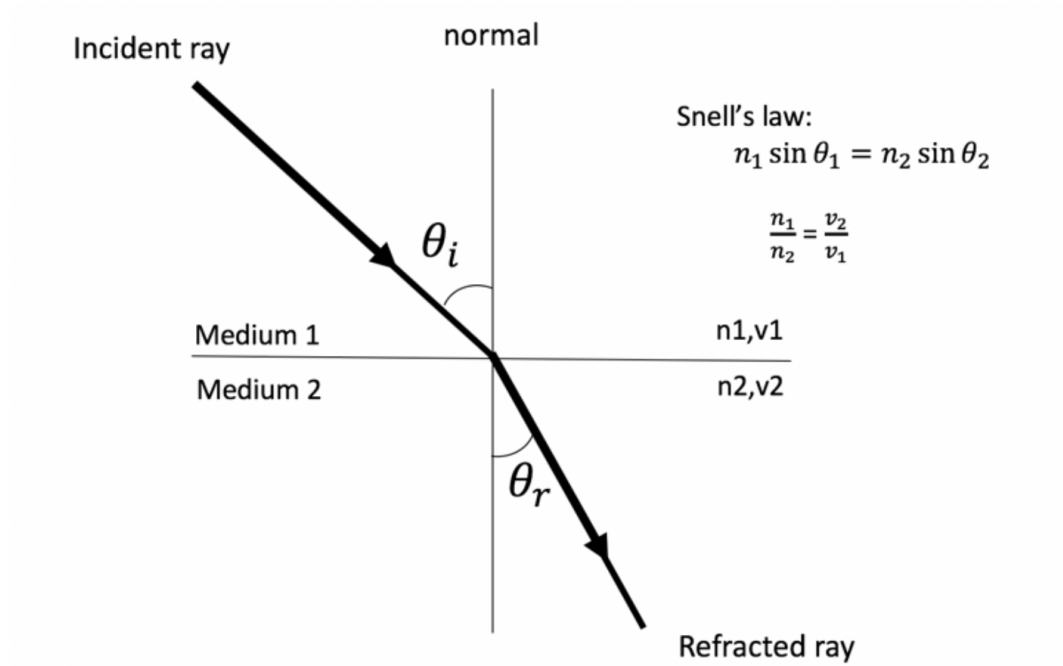


Figure 6.6: Incident and refracted ray

As can be seen from the Figure 6.6, the normal vector of the plane was set as a rotation matrix. The angle between the incidence ray and the normal of the plane is given. For local coordinates of the plane (normal vector can be considered as z-axis in local coordinate), the

formula (6.35) can be used. In this case, the refracted angle from Snell's law is used. Then, once the incidence and refracted angle is obtained, the rotations angle can be calculated using the following formula.

$$\theta = \pi - \theta_i + \theta_r \quad (6.36)$$

By knowing the rotation axis and angle, we can calculate the refraction vector (refraction ray). Then, the refracted ray will be the incidence ray from inside the ice crystals and the reflection vector needs to be found (reflection ray).

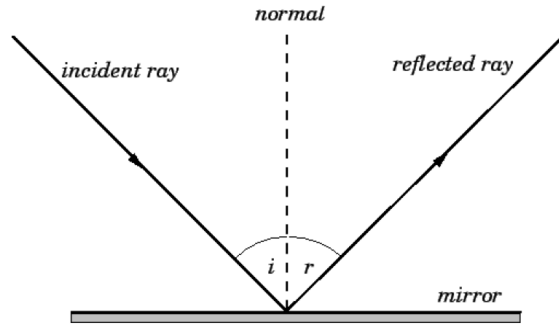


Figure 6.7: Incident and reflected ray

By knowing the rotation axis and angle, we can calculate the refraction vector (refraction ray). Then, the refracted ray will be the incidence ray from inside the ice crystals and the reflection vector needs to be found (reflection ray).

For reflection we can also use formula (6.35). In this case the rotation angle is $\theta = 2\theta_i$ ($\theta_i = \theta_r$).

6.2.3 High-level explanation of the PO method

The essential feature of physical optics method is that an electromagnetic field can be modelled as a plane wave spectrum. Rays are in effect a high frequency approximation where the individual rays can represent the wavefront which is perpendicular to the ray. Figure 6.8 shows the plane wave is modelled as 17 rays incident on the bottom facet of a hexagon as an example. The red lines indicate the incident rays and the red circles denote the intersection points between the incidence and the bottom facet.

The incident field can be expressed as,

$$E_{inc} = E_0 e^{-jk_{red}(r-r_{ref})} \quad (6.37)$$

$$H_{inc} = k_{red} \times \frac{E_{inc}}{\omega \mu_0} \quad (6.38)$$

where E_0 is the amplitude of the electric field, k_{red} is the propagation wave vector of the red line (incident field), r is the observation point, r_{ref} is the reference point defined for zero phase (r_{ref} usually is origin), ω is the angular frequency, and μ_0 is the free-space permeability.

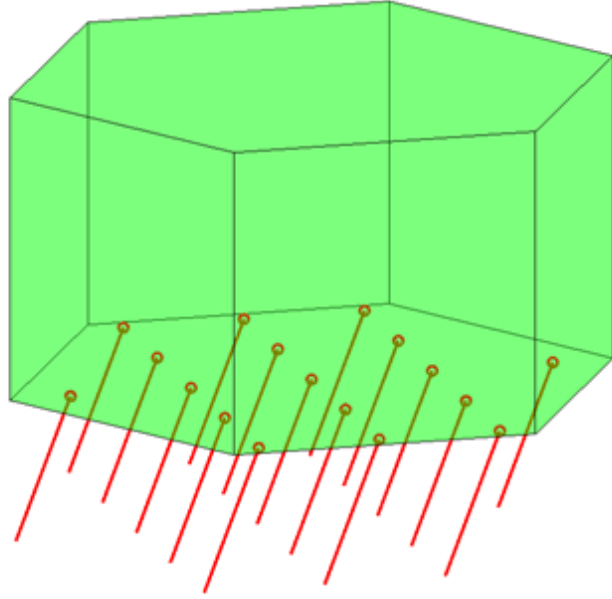


Figure 6.8: Incident field at the bottom facet of the hexagonal prism ice crystal

After each ray is transmitted into the interior of the crystal, it bounces back and forth inside the ice crystal. Figure 6.9 shows the path of a single ray. In this example, the initial transmission and four internal reflections are shown. In practice, it appears that because of transmission and absorption losses it is not necessary to consider more than this number of reflections. It should be emphasised that since the scattered field can be computed from a knowledge of the total internal field, it is not necessary to consider explicitly the partial transmissions that occur with each reflection. Different colours represent the rays after each transmission or reflection, e.g., the blue and pink lines are the first transmitted ray and the second reflected ray in the hexagon. For example, the black line is the ray after one transmission through the bottom facet and one reflection from the top facet. Various circles also denote the intersection points on the facets.

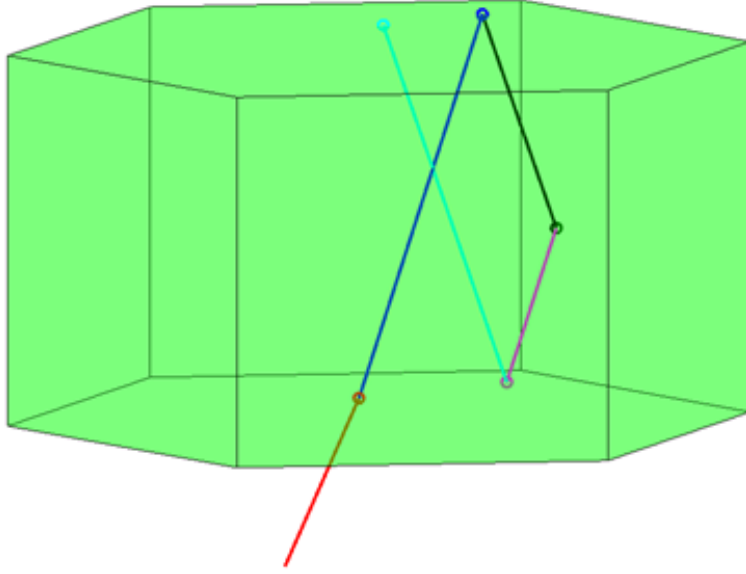


Figure 6.9: Refracted and reflected fields inside the hexagonal prism ice crystal

In order to calculate the scattered fields inside the hexagon, the ray path and reflection/transmission coefficients of different polarised fields needs to be evaluated.

First, the ray path is calculated based on the intersection point, incident, reflection, and transmission angle of a ray with respect to each facet. At each facet, the reflection and transmission angles are calculated based on Snell's law, as shown in Figure 6.6, where n_1 and n_2 are the reflective index of hexagon and air. The ray path is independent of the polarisation of the incident fields. Then, the electric and magnetic fields are decomposed into TE and TM fields with respect to each facet, i.e., $E = E_{TE} + E_{TM}$. The transmission and reflection (Fresnel) coefficients at each facet are computed for TE and TM waves based on the incident, transmission angles, and impedance of both media. The TE and TM waves are defined based on the surface formed by the ray direction and the normal of facet.

For TE wave, the coefficients are,

$$\Gamma_{TE} = \frac{\eta_2 \cos \theta_i - \eta_1 \cos \theta_t}{\eta_2 \cos \theta_i + \eta_1 \cos \theta_t} \quad (6.39)$$

$$\tau_{TE} = \frac{2\eta_2 \cos \theta_i}{\eta_2 \cos \theta_i + \eta_1 \cos \theta_t} \quad (6.40)$$

where θ_i and θ_t are the incident and transmission angles, η_1 and η_2 are the impedance of both media. For the TM wave, the coefficients are

$$\Gamma_{TM} = \frac{\eta_2 \cos \theta_t - \eta_1 \cos \theta_i}{\eta_2 \cos \theta_t + \eta_1 \cos \theta_i} \quad (6.41)$$

$$\tau_{TM} = \frac{2\eta_2 \cos \theta_i}{\eta_2 \cos \theta_t + \eta_1 \cos \theta_i} \quad (6.42)$$

After the ray paths, angles, and Fresnel coefficients are solved, the electric and magnetic fields at any position inside the geometry can be calculated. For example, the electric field at the black circle position on the side facet (in Figure 6.9) is calculated as follows:

1. The electric field E^{red} at the red circle position (inside the hexagon) is written as

$$E^{red} = (E_{TE}^0 \tau_{TE}^0 + E_{TM}^0 \tau_{TM}^0) e^{-jk_{red} \cdot (r_{red} - r_{ref})} \quad (6.43)$$

2. The electric field at the blue circle position (inside the hexagon) is formulated as

$$E^{blue} = (E_{TE}^{red} \Gamma_{TE}^{red} + E_{TM}^{red} \Gamma_{TM}^{red}) e^{-jk_{blue} \cdot (r_{blue} - r_{red})} \quad (6.44)$$

3. the electric field at the black circle position (inside the hexagon) is expression as

$$E^{black} = (E_{TE}^{blue}\Gamma_{TE}^{blue} + E_{TM}^{blue}\Gamma_{TM}^{blue})e^{-jk_{black}\cdot(r_{black}-r_{blue})} \quad (6.45)$$

In the next step, three planes in the xoy, yoz, and xoz directions are selected in the middle of geometry. The intersection points between all the rays associated with each reflection and the three planes are found and the electric fields at these points are also calculated. Then, the 2D-FFT is applied to the electric field associated with each reflection in order to find the propagation direction of all the rays associated with each reflection.

6.2.4 Flowchart of the 3D ray-tracing and PO by dielectric prism

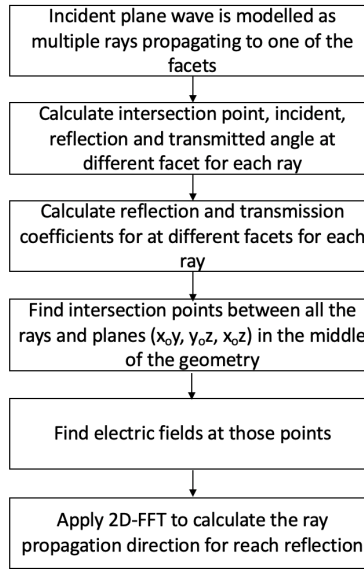


Figure 6.10: High-level flowchart of PO by dielectric prism

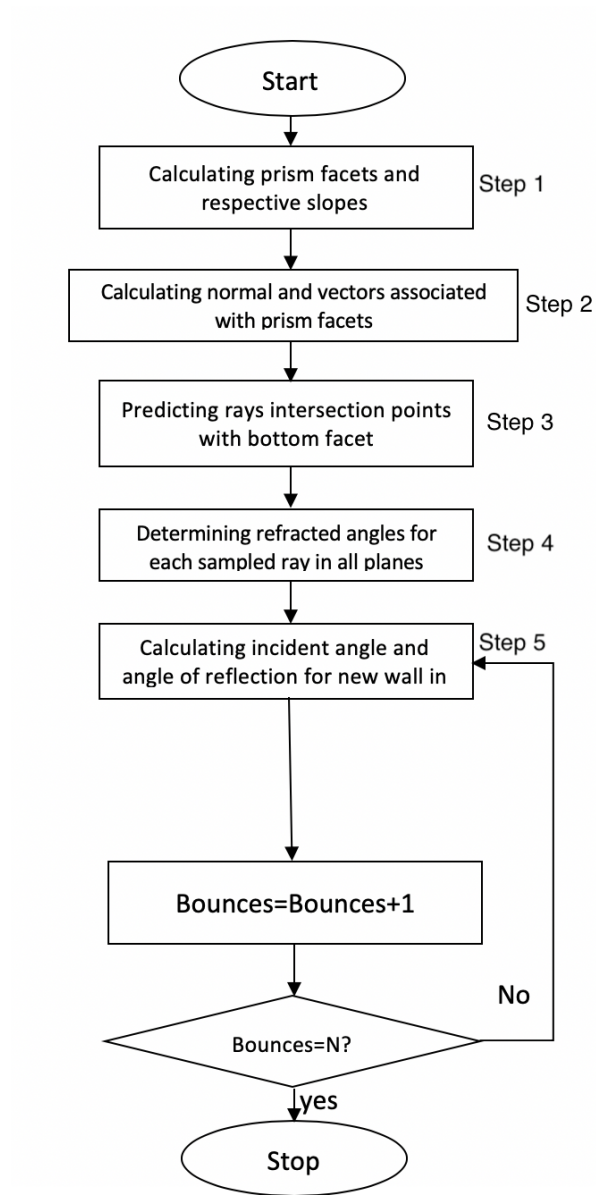


Figure 6.11: 3D ray-tracing by a dielectric prism (the steps are mapped to the algorithm used for the implementation)

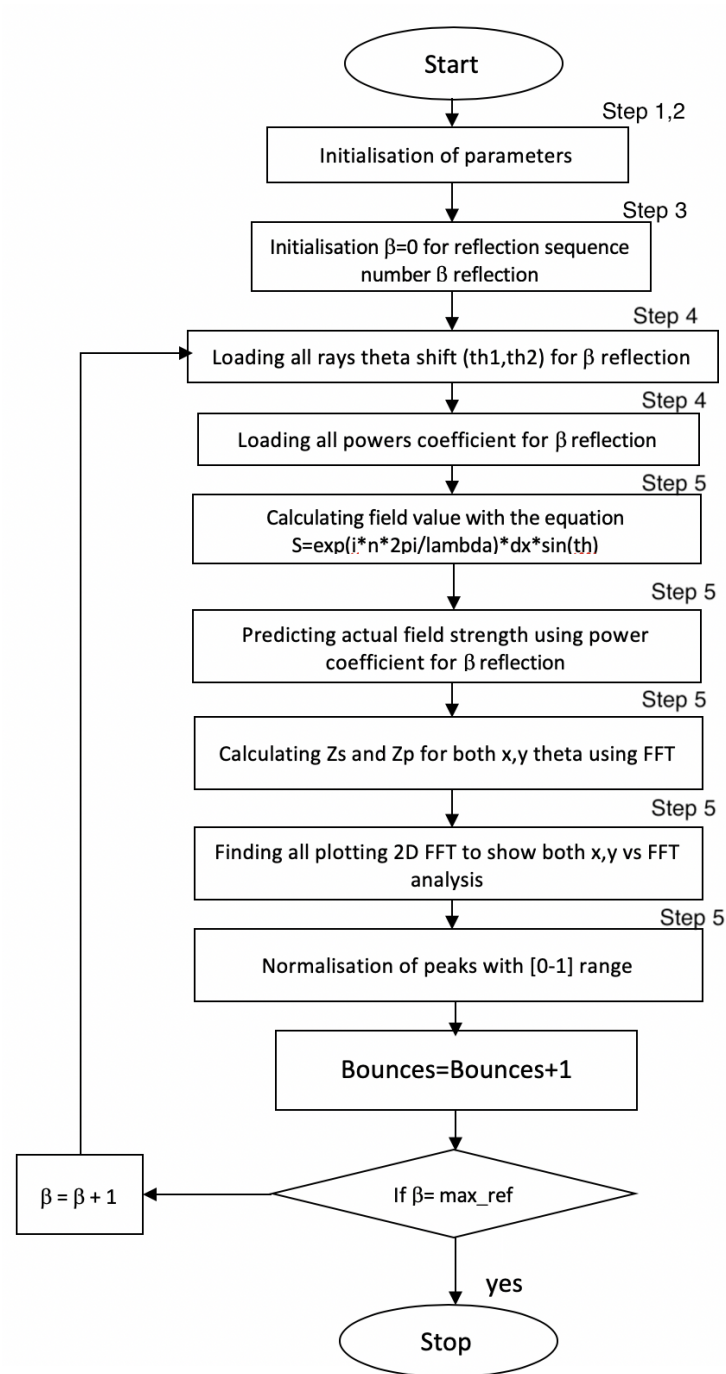


Figure 6.12: 3D PO by a dielectric prism (the steps are mapped to the algorithm used for the implementation)

6.2.5 3D ray-tracing and physical optics by a dielectric prism algorithm

The algorithm of the implementation of the ray-tracing and PO follows several steps: the first step is to implement the planes (prism facets) that the rays intersects with. The method can be solved by finding the plane equations for each facet. Then, the rays are generated and the spherical coordinate systems used to predict the direction of the refracted and reflected rays, whilst taking the intersection points between the planes and lines into account. The main algorithms which show the steps taken to implement the ray-tracing and PO are as follows:

Algorithm 6.1 High-level Pseudo code:

```
1: create_geometry: Generate the geometry
2: define_incident: Define plane wave including propagation direction, number
   of rays (num_ray), and maximum number of reflections that are considered
   (max_num_reflection)
3: for ( doi=1:num_ray)
4:   for ( do j=1:max_num_reflection)
5:     find_intersection
6:     find_inc_ref_trans_angle
7:     find_fresnel_coeff
8:     find_phase_delay
9:   end for
10: end for
11: find_field_at_fft_plane
12: 2d_fft
```

Algorithm 6.2 Step 1: predicting slopes for prism walls

```
1:  $W_A = \{0, 60, 120, 90, 90\}$ 
2: for  $i=1$  to  $i=W_{A_{len}}$  do
3:    $mw_i = \tan(W_{Ai})$ 
4: end for
5:  $WA_i$  represents the horizontal angle of  $i^{th}$  wall
6:  $mw_i$  denotes the slope of  $i^{th}$  wall
```

Algorithm 6.3 Step 2: predicting prism walls vectors and constants

```
1: for  $i=1$  to  $i=W_{pts\_len}$  do
2:    $P_{xyz} = W_{pts}[i, 1]$ 
3:    $Q_{xyz} = W_{pts}[i, 2]$ 
4:    $R_{xyz} = W_{pts}[i, 3]$ 
5:    $PQ_{vector} = Q_{xyz} - P_{xyz}$ 
6:    $PR_{vector} = R_{xyz} - P_{xyz}$ 
7:    $D = \begin{vmatrix} PQ_{vector} \\ PR_{vector} \end{vmatrix}$ 
8:    $a = D_{12} \times D_{23} - D_{22} \times D_{13}$ 
9:    $b = -1 \times D_{11} \times D_{23} - D_{21} \times D_{13}$ 
10:   $c = D_{11} \times D_{22} - D_{21} \times D_{12}$ 
11:   $const_i = -1 \times ((-1P_x a) + (-1P_y b) + (-1P_z c))$ 
12: end for
13: Where P Q R are any three points from the plane
14: a, b & c are the perpendiculars of the plane
15: D is the matrix having two vectors PQ & PR
16:  $Const_i$  is the constant for  $i^{th}$  plane equation
```

Algorithm 6.4 Step 3: generating Rays and sampling points

```
1: k=1
2: for i=1 to i=rays do
3:   x = [ (Posx,d - Posx,I) / rays] x i
4:   for j=1 to j=rays do
5:     y = [ (Posy,d - Posy,I) / rays] x j
6:     z = Posz,I
7:     Raysk={x,y,z}
8:     k=k+1
9:   end for
10: end for
```

11: Where rays is the constant value given by user for number of samples to be taken for evaluating

12: Pos_{x,d} is the maximum value of x plane of bottom wall

13: Pos_{x,I} is the starting value of x plane of the bottom wall

Algorithm 6.5 Step 4: predicting first reflection and refraction of rays

```
1: for i=1 to i=rays do
2:    $\theta_1 = \sin^{-1}(m_1 * \sin(\theta_{i1}) / m_2)$ 
3:    $\theta_2 = \sin^{-1}(m_1 * \sin(\theta_{i2}) / m_2)$ 
4:   p =  $\theta_1$ ;
5:   t =  $\theta_2$ ;
6:   r = c;
7:   x = r * sin(p) * cos(t)
8:   y = r * sin(p) * sin(t)
9:   z = r * cos(p)
10:  dir_vect = pred_vect{[x,y,z],ptxyz}
11:  intercept = CIW[dir_vect,raysi]
12: end for
```

13: θ_1 and θ_2 are the theta's of rays in two different plane

14: m_1 m_2 are the reflective index for mediums

15: p t r are the variables to predict direction vector of ray

16: x y z are the points on the same ray having c distance from first intersection with prism

17: pred_vect is the function to predict direction vector for ray

18: CIW is the function to check whether current ray going to meet with any wall inside the predefined limits, it gives true if ray condition meets and interests any wall in prism limit

Algorithm 6.6 Step 5: predicting multiple reflections in prism

```
1: for i=1 to i =ref do
2:   ref_slope1 = tan-1 (pt1x - pt2x / pt1z - pt2z)
3:   ref_slope2 = tan-1(pt1y - pt2y / pt1z - pt2z)
4:   θ1i = tan-1( (mw - ref_slope1) / (1 + mw * ref_slope1))
5:   θ2i = tan-1( (mw - ref_slope2) / (1 + mw * ref_slope2))
6:   if θ1i < 0 then
7:     θ1i = | θ1i |
8:   end if
9:   if if θ2i < 0 then
10:    θ2i = | θ2i |
11:   end if
12:   θ1r = 180 + θ1i
13:   θ2r = 180 + θ2i
14:   p = θ1r
15:   t = θ2r
16:   r = c
17:   x = r * sin(p) * cos(t)
18:   y = r * sin(p) * sin(t)
19:   z = cos(p)
20:   dir_vect = pred_vect{[x,y,z],ptxyz}
21:   intercept = CIW[dir_vect,raysi]
22: end for
```

23: where ref_slope₁ and ref_slope₂ are the slopes of ray in two different planes
24: m_w is the slope for incident prism wall
25: θ_{1i} and θ_{2i} are the predicted incident angles in two different planes
26: θ_{1r} and θ_{2r} are the reflected angles in two different planes
27: p t r are the variable to predict direction vector of reflected ray at distance c from point of reflection
28: CIW is the function to check whether current ray going to meet with any wall inside the predefined limits, it gives true if ray condition meets and interests any wall in prism limit

6.2.6 Results

The ray-tracing and PO results were made in the lossless case. The imaginary part of the refractive index of ice is so small in practice that it makes an almost negligible difference to the Fresnel coefficients. The main effect of the imaginary part is to attenuate the reflected waves and the transmission losses reduce the amplitude, such that the overall effect when taking into account the finite number of reflections is not changed greatly by ignoring it. The assumptions taken for the model were that the angle of incidence to the bottom facet of the 3D prism ice ($\Theta_i=30^\circ$), ($\Theta_j=30^\circ$) as in 3D have two shifting angles, as discussed in Section 6.1.2, where the spherical coordinate system was used to plot in 3D, the refractive index outside the prism ($n_1=1$) and the refractive index of the prism ($n_2=1.787$). The ray-tracing results are shown in the following figures.

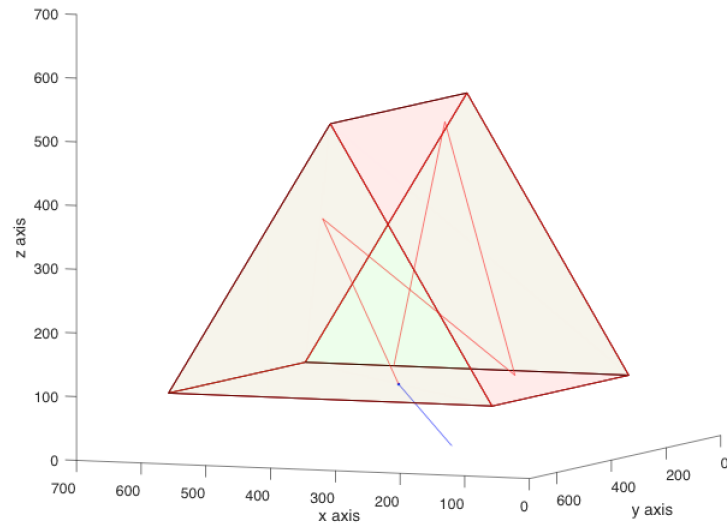


Figure 6.13: Single ray-tracing by a dielectric prism

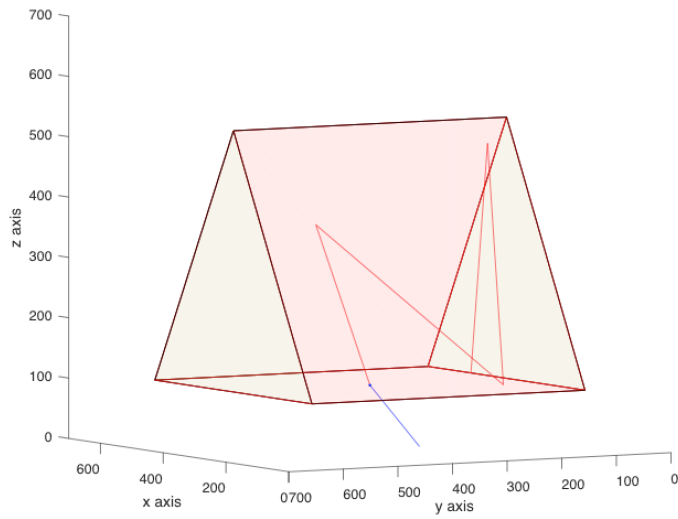


Figure 6.14: Single ray-tracing by a dielectric prism

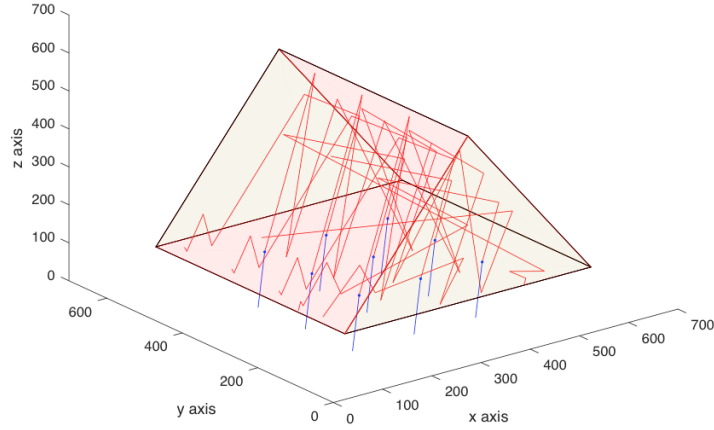


Figure 6.15: Multiple ray-tracing by a dielectric prism

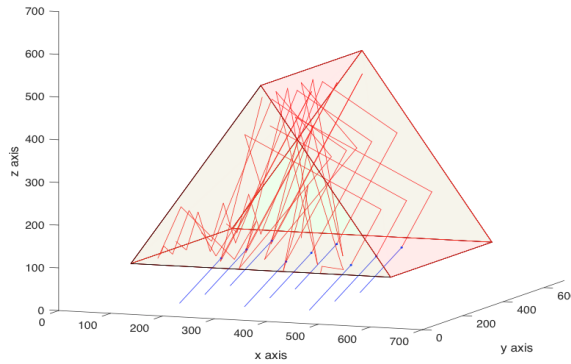


Figure 6.16: Multiple ray-tracing by a dielectric prism

In regards to the PO solution, this could be done by using either the non-linear shift method, which is described in Chapter 3, or by using the orthogonal shearing method. For this implementation, the non-linear shift method is done with respect to two angles (3D), unlike the 2D shift where the shift comes from one direction. The result of the 3D PO can be described by the 2D FFT and contour plot. The contour plots indicate the field at each facet of triangular prism. The facets are divided as follows,

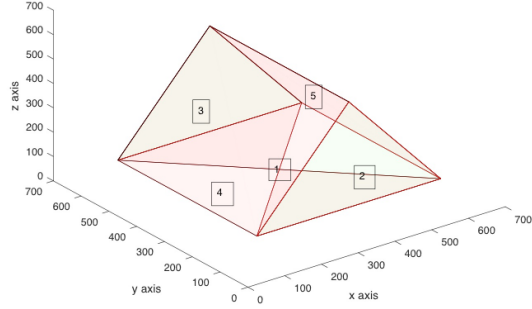


Figure 6.17: Triangular prism facets

The contour plots which show the field at each facet at every stage from incidence to the fifth order of reflection are shown in the following figures. The incident field is at $(\Theta_i=30^\circ, \Theta_j=30^\circ)$ and the refractive index of the triangular prism is 1.787 and 1 outside the prism. The results were as follows.

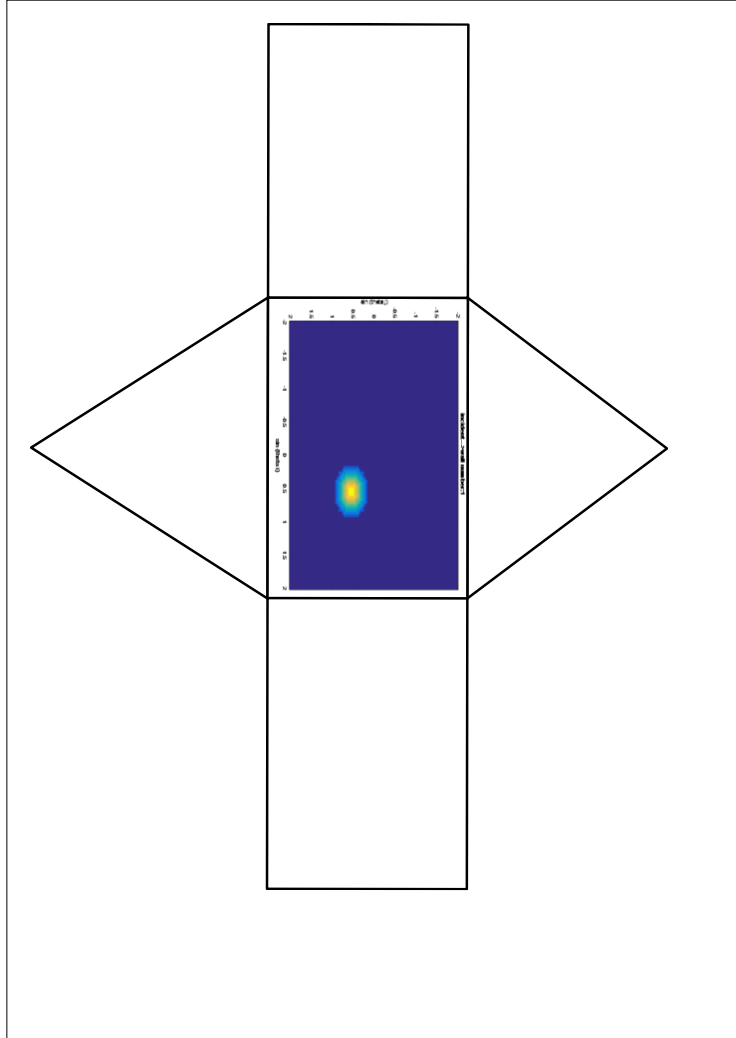


Figure 6.18: Incident field to the bottom facet of the dielectric prism

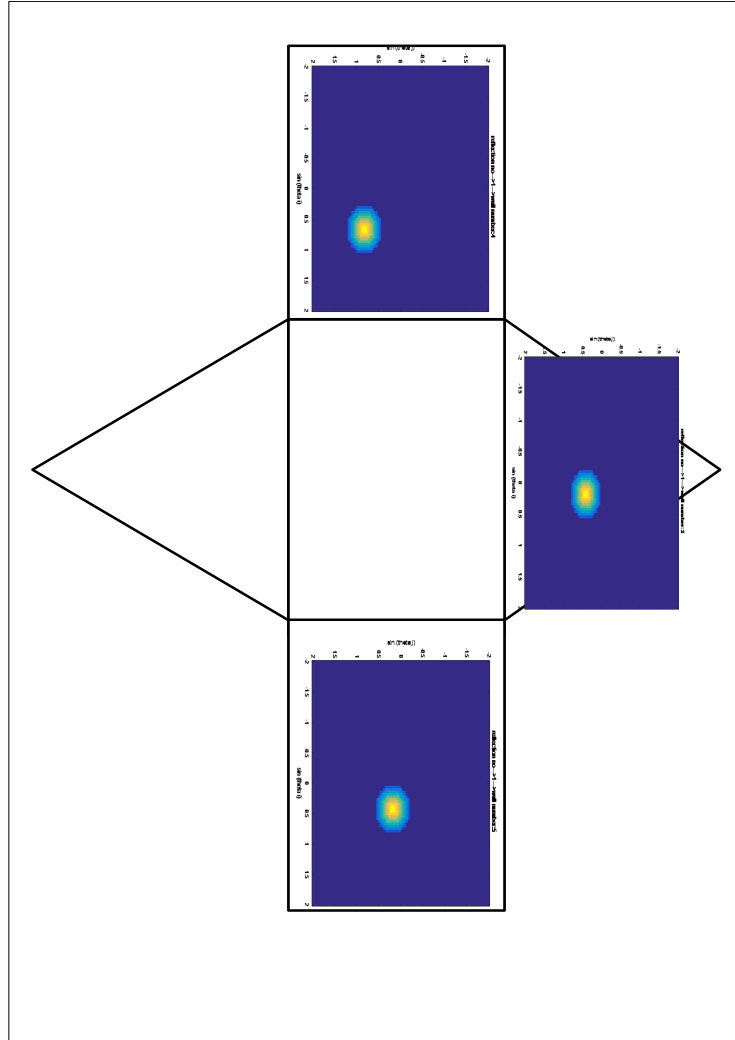


Figure 6.19: First order of reflection inside the dielectric prism

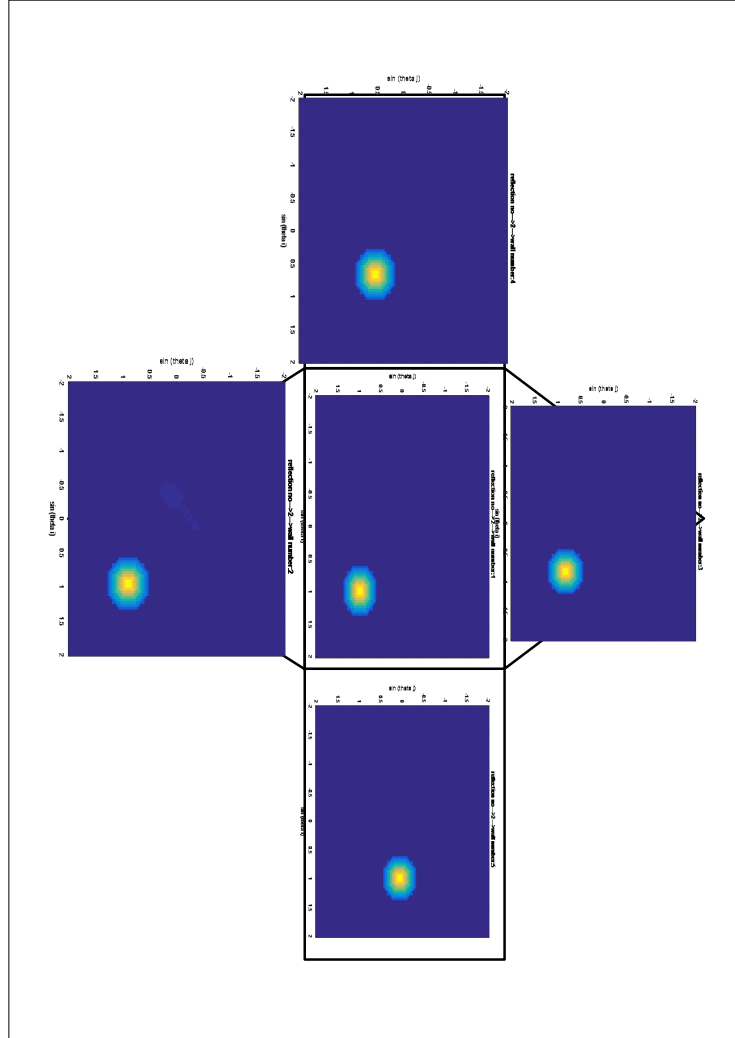


Figure 6.20: Second order of reflection inside the dielectric prism

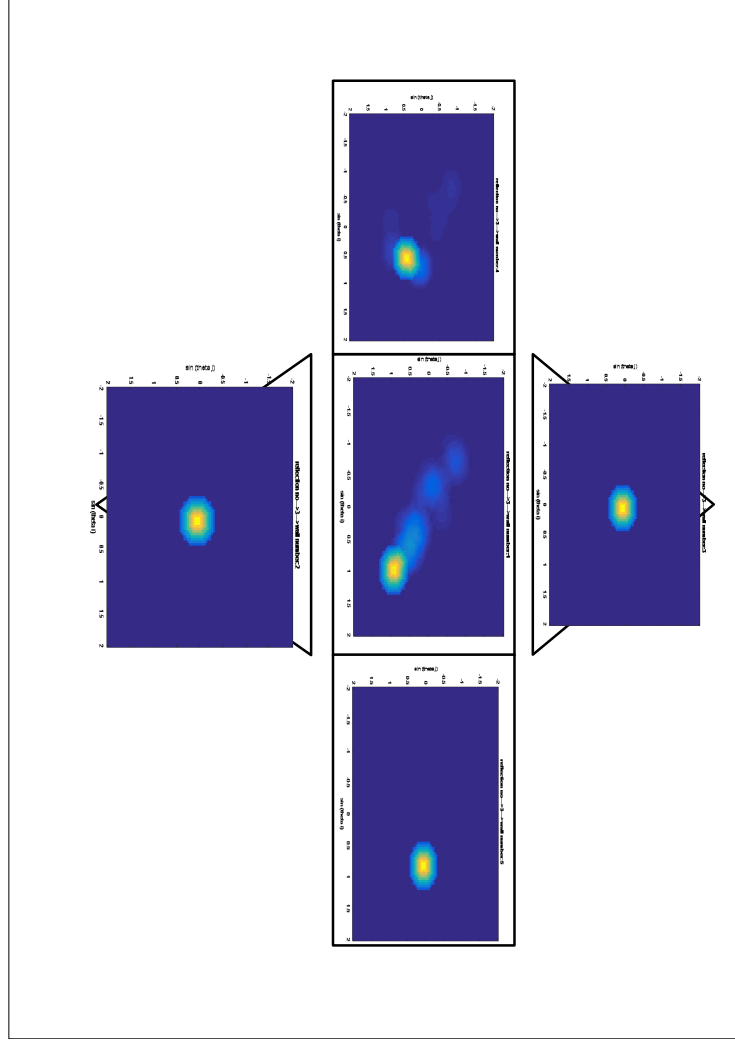


Figure 6.21: Third order of reflection inside the dielectric prism

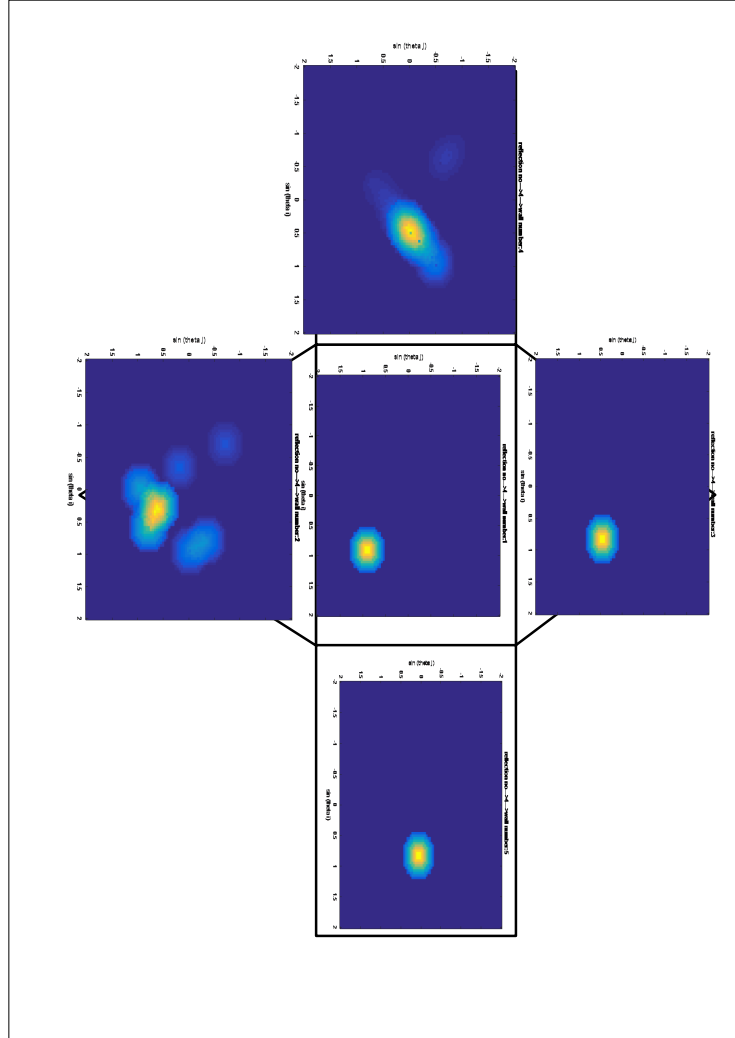


Figure 6.22: Fourth order of reflection inside the dielectric prism

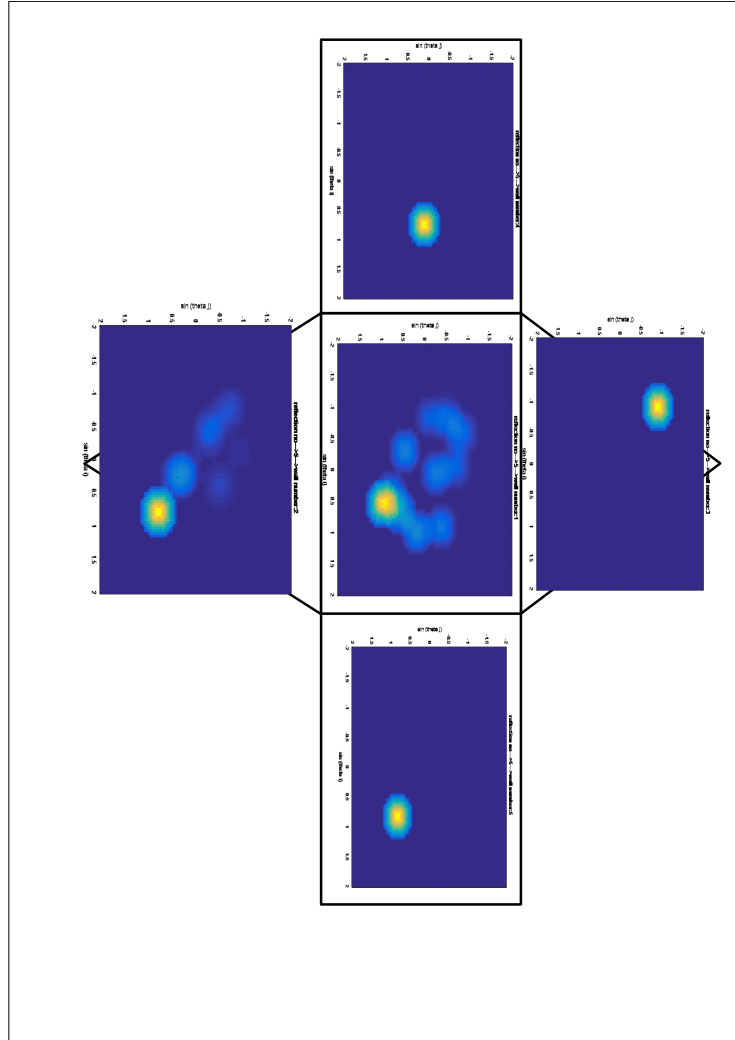


Figure 6.23: Fifth order of reflection inside the dielectric prism

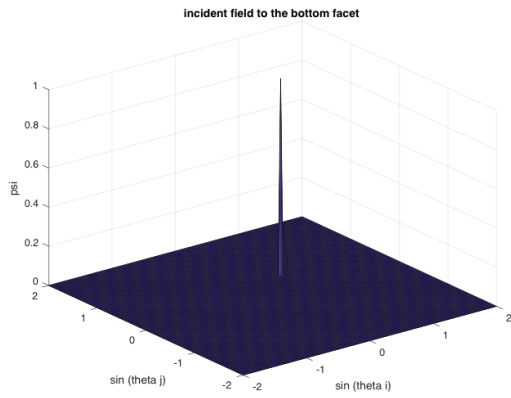


Figure 6.24: Total incident field in prism

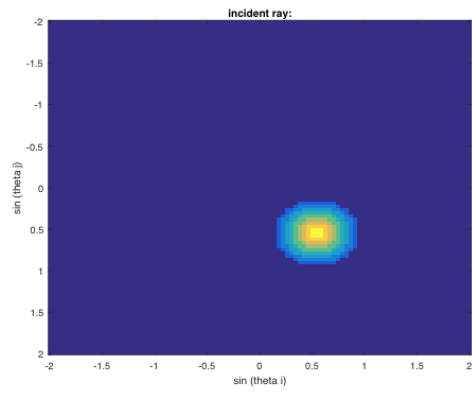


Figure 6.25: Total incident field in prism

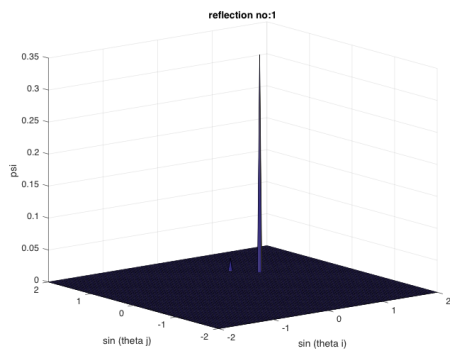


Figure 6.26: Field of 1st order of reflection in prism

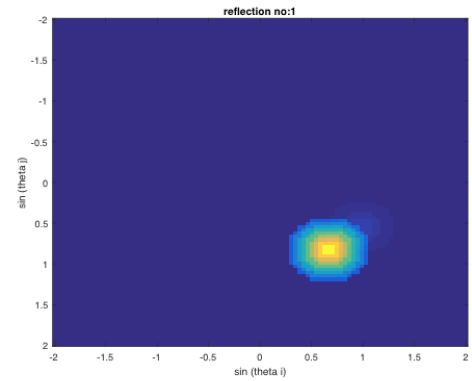


Figure 6.27: Field of 1st order of reflection in prism

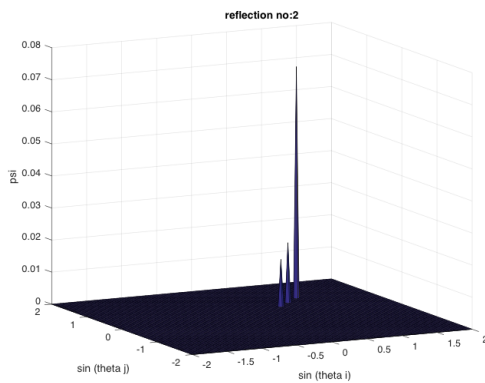


Figure 6.28: Field of 2nd order of reflection in prism

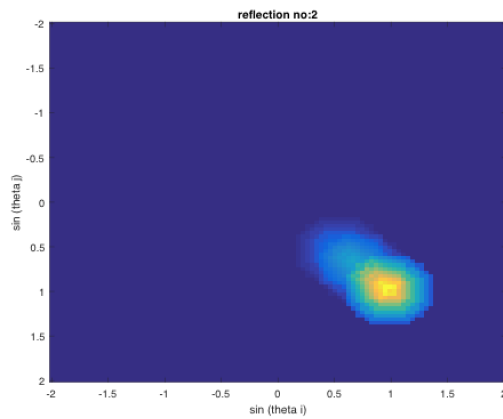


Figure 6.29: Field of 2nd order of reflection in prism

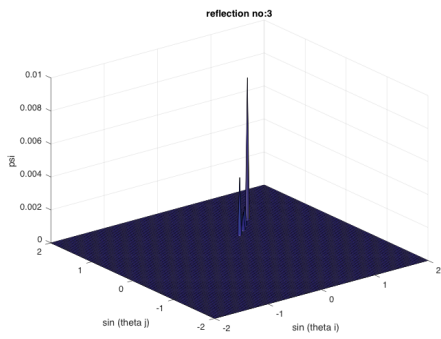


Figure 6.30: Field of 3rd order of reflection in prism

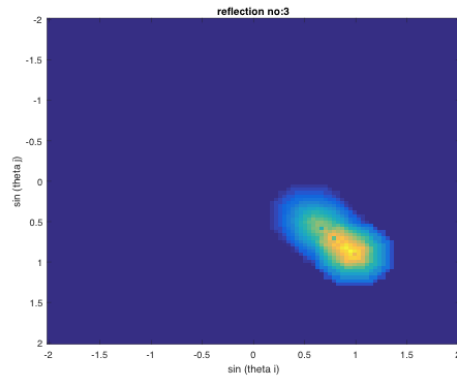


Figure 6.31: Field of 3rd order of reflection in prism

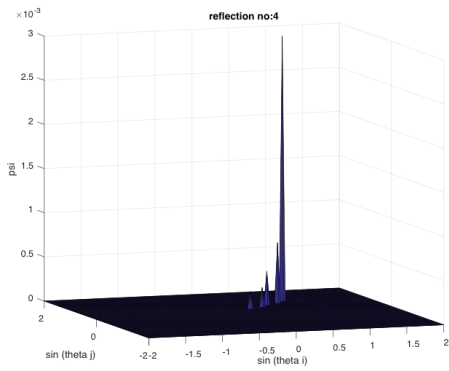


Figure 6.32: Field of 4th order of reflection in prism

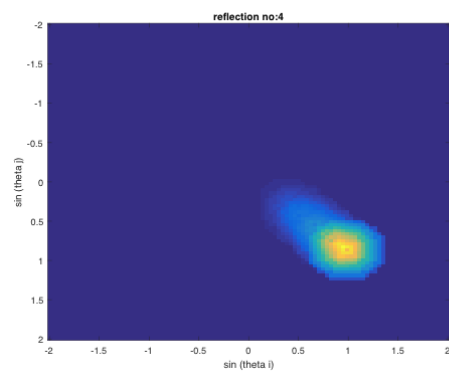


Figure 6.33: Field of 4th order of reflection in prism

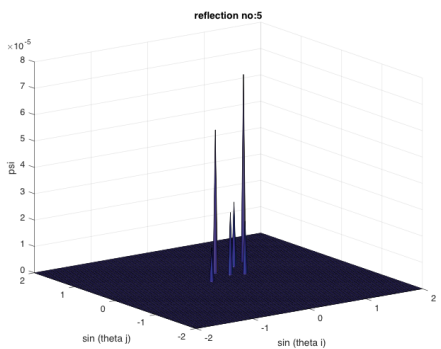


Figure 6.34: Field of 5th order of reflection in prism

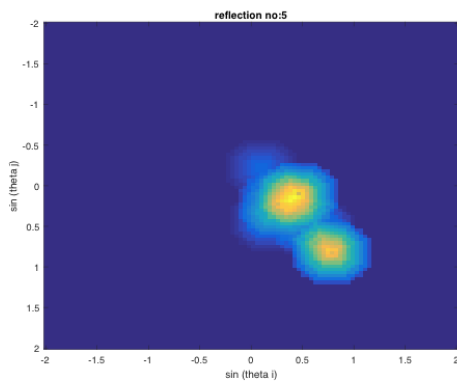


Figure 6.35: Field of 5th order of reflection in prism

The figures from 6.18 to 6.23 show the contour plot of the PO solution of the field FFT which show field shift locations from the incident field upto the fifth order of reflection inside the triangular prism. Figures 6.24 to 6.35 show the FFT of the total field magnitude for all facets with the shifts from the incident field until the fifth order reflection. It can be noted that the field magnitude decreases as the number of reflection increases and also the multiple shifts per reflections is noticed as the field is distributed in the facets. It is also worth mentioning that the field magnitude decreases as the number of reflection increases due to the scattered field outside the prism per reflection. After finding the PO solution, which shows the field locations and the magnitudes, the reaction theorem is going to be used in order to find the total scattered field.

6.3 3D ray-tracing and physical optics method for scattering by dielectric hexagonal prism ice crystal

6.3.1 Flowchart

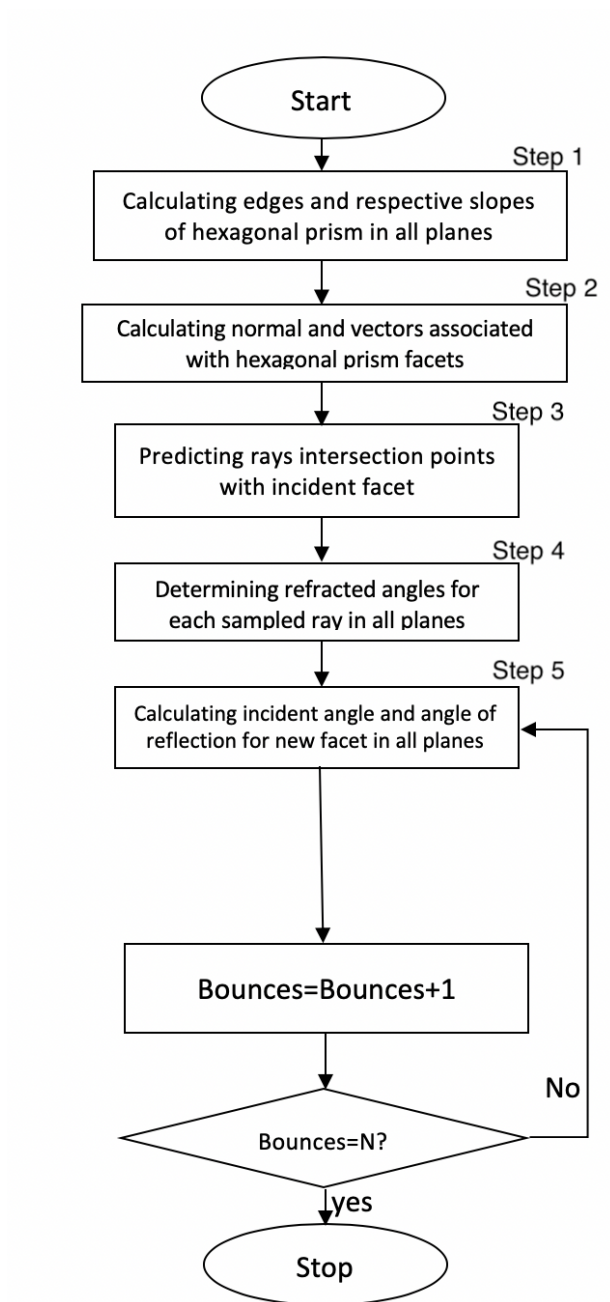


Figure 6.36: 3D ray-tracing by a hexagonal prism ice crystal (the steps are mapped to the algorithm used for the implementation)

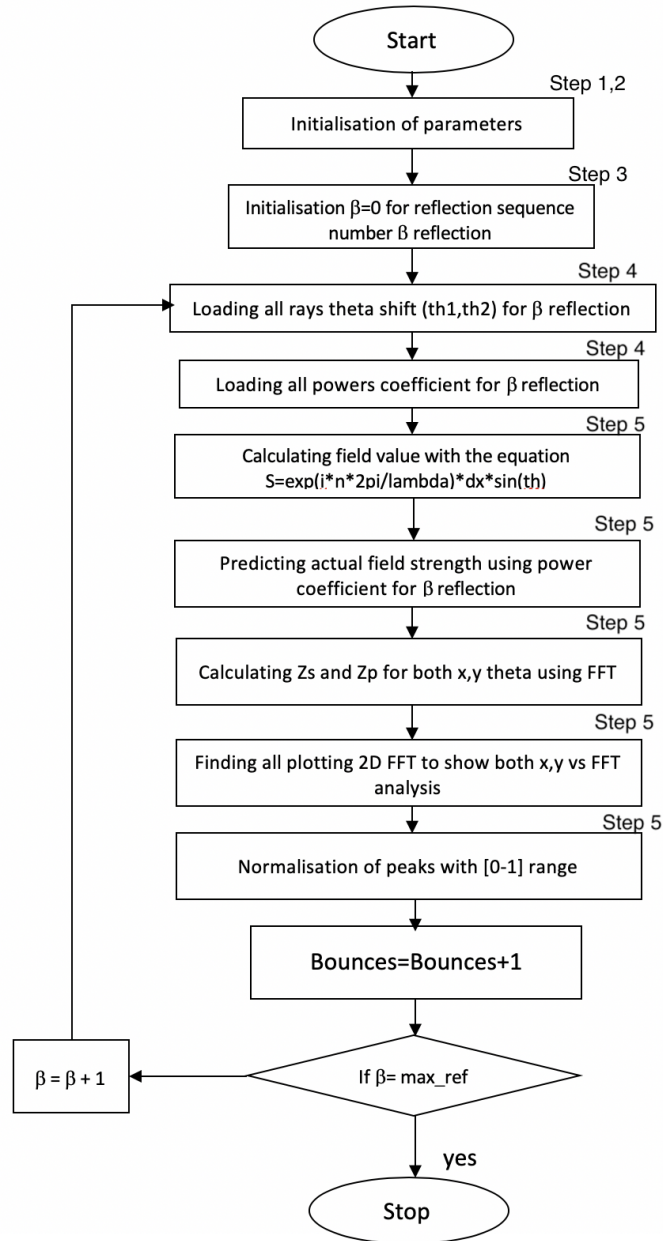


Figure 6.37: 3D PO by a hexagonal prism ice crystal (the steps are mapped to the algorithm used for the implementation)

6.3.2 Algorithm

The algorithm for the implementation of the ray-tracing and PO follows several steps: the first step is to implement the planes (hexagonal prism facets) that the rays intersects with. The method can be solved by finding the plane equations for each facet. Then, the rays will be generated and the spherical coordinate systems can be used to predict the direction of the refracted and reflected rays and taking the intersection points between the planes and lines into account. The main algorithms which show the steps taken to implement the ray-tracing and PO are as follows:

Algorithm 6.7 High-level pseudo code:

```
1: create_geometry: Generate the geometry
2: define_incident: Define plane wave including propagation direction, number
  of rays (num_ray), and maximum number of reflections that are considered
  (max_num_reflection)
3: for ( doi=1:num_ray)
4:   for ( do j=1:max_num_reflection)
5:     find_intersection
6:     find_inc_ref_trans_angle
7:     find_fresnel_coeff
8:     find_phase_delay
9:   end for
10: end for
11: find_field_at_fft_plane
12: 2d_fft
```

Algorithm 6.8 Step 1: predicting slopes for hexagonal prism facets

```
1:  $W_A = \{0, 60, 120, 0, 60, 120, 0, 0\}$ 
2: for  $i=1$  to  $i=W_A.\text{len}$  do
3:    $mw_i = \tan(W_{Ai})$ 
4: end for
5:  $WA_i$  represents the horizontal angle of  $i^{th}$  wall
6:  $mw_i$  denotes the slope of  $i^{th}$  wall
```

Algorithm 6.9 Step 2: predicting hexagonal prism walls vectors and constants

```
1: for  $i=1$  to  $i=Wpts.\text{len}$  do
2:    $P_{xyz} = W_{pts}[i, 1]$ 
3:    $Q_{xyz} = W_{pts}[i, 2]$ 
4:    $R_{xyz} = W_{pts}[i, 3]$ 
5:    $PQ_{vector} = Q_{xyz} - P_{xyz}$ 
6:    $PR_{vector} = R_{xyz} - P_{xyz}$ 
7:    $D = |PQ_{vector}|$ 
8:    $|PR_{vector}|$ 
9:    $a = D_{12} \times D_{23} - D_{22} \times D_{13}$ 
10:   $b = -1 \times D_{11} \times D_{23} - D_{21} \times D_{13}$ 
11:   $c = D_{11} \times D_{22} - D_{21} \times D_{12}$ 
12:   $const_i = -1 \times ((-1P_x a) + (-1P_y b) + (-1P_z c))$ 
13: end for
14: Where  $PQR$  are any three points from the plane
15:  $a, b$  &  $c$  are the perpendiculars of the plane
16:  $D$  is the matrix having two vectors  $PQ$  &  $PR$ 
17:  $Const_i$  is the constant for  $i^{th}$  plane equation
```

Algorithm 6.10 Step 3: generating rays and sampling points

```
1: k=1
2: for i=1 to i=rays do
3:   x = [ (Posx,d - Posx,I) / rays] x i
4:   for j=1 to j=rays do
5:     y = [ (Posy,d - Posy,I) / rays] x j
6:     z = Posz,I
7:     Raysk={x,y,z}
8:     k=k+1
9:   end for
10: end for
11: Where rays is the constant value given by user for number of samples to be taken for
    evaluating
12: Posx,d is the maximum value of x plane of bottom wall
13: Posx,I is the starting value of x plane of the bottom wall
```

Algorithm 6.11 Step 4: predicting first reflection and refraction of rays

```
1: for i=1 to i=rays do
2:    $\theta_1 = \sin^{-1}(m_1 * \sin(\theta_{i1}) / m_2)$ 
3:    $\theta_2 = \sin^{-1}(m_1 * \sin(\theta_{i2}) / m_2)$ 
4:   p =  $\theta_1$ ;
5:   t =  $\theta_2$ ;
6:   r = c;
7:   x = r * sin(p) * cos(t)
8:   y = r * sin(p) * sin(t)
9:   z = r * cos(p)
10:  dir_vect = pred_vect{[x,y,z],ptxyz}
11:  intercept = CIW[dir_vect,raysi]
12: end for
13:  $\theta_1$  and  $\theta_2$  are the theta's of rays in two different planes
14: m1 m2 are the reflective index for mediums
15: p t r are the variables to predict direction vector of ray
16: x y z are the points on the same ray having c distance from first intersection with
    hexagonal prism
17: pred_vect is the function to predict direction vector for ray
18: CIW is the function to check whether current ray going to meet with any wall inside
    the predefined limits, it gives true if ray condition meets and interests any wall in the
    hexagonal prism limit
```

Algorithm 6.12 Step 5: predicting multiple reflections in hexagonal prism

```
1: for i=1 to i =ref do
2:   ref_slope1 = tan-1 (pt1x - pt2x / pt1z - pt2z)
3:   ref_slope2 = tan-1(pt1y - pt2y / pt1z - pt2z)
4:   θ1i = tan-1( (mw - ref_slope1) / (1 + mw * ref_slope1))
5:   θ2i = tan-1( (mw - ref_slope2) / (1 + mw * ref_slope2))
6:   if θ1i < 0 then
7:     θ1i = | θ1i |
8:   end if
9:   if if θ2i < 0 then
10:    θ2i = | θ2i |
11:   end if
12:   θ1r = 180 + θ1i
13:   θ2r = 180 + θ2i
14:   p = θ1r
15:   t = θ2r
16:   r = c
17:   x = r * sin(p) * cos(t)
18:   y = r * sin(p) * sin(t)
19:   z = cos(p)
20:   dir_vect = pred_vect{[x,y,z],ptxyz}
21:   intercept = CIW[dir_vect,raysi]
22: end for
```

23: where ref_slope₁ and ref_slope₂ are the slopes of ray in two different planes
24: m_w is the slope for incident prism wall
25: θ_{1i} and θ_{2i} are the predicted incident angles in two different planes
26: θ_{1r} and θ_{2r} are the reflected angles in two different planes
27: p t r are the variable to predict direction vector of reflected ray at distance c from point of reflection
28: CIW is the function to check whether current ray going to meet with any wall inside the predefined limits, it gives true if ray condition meets and interests any wall in prism limit

Algorithm 6.13 For phase delay

- 1: find the distance between the two intersection points.
 - 2: $\text{phase_delay} = \exp(-j*k*\text{distance})$
-

Algorithm 6.14 To find `field_at_FFT` plane

- 1: **for** `i=1:num_ray` **do**
 - 2: **for** `j=1:max_num_reflections` **do**
 - 3: `find_intersection_at_FFT_plane`
 - 4: `find_distance_between_intersections_on_FFTplane_facet`
 - 5: `field=field_at_facet(i)*exp(-c1*k*distance)`
 - 6: **end for**
 - 7: **end for**
-

6.3.3 Results

The ray-tracing and PO results follows the same methodology as the triangular prism. The ray-tracing and PO results were made in a lossless case. The assumptions taken for the model were that the angle of incidence to the bottom facet of the 3D hexagonal prism ice ($\Theta_i=60^\circ$), ($\Theta_j=60^\circ$) as in 3D we have two shifting angles, as discussed in Section 6.1.2, where the spherical coordinate system was used to plot in 3D, the refractive index outside the hexagonal prism ($n_1=1$) and the refractive index of the hexagonal prism ($n_2=1.787$). The ray-tracing and PO results are shown in the following figures.

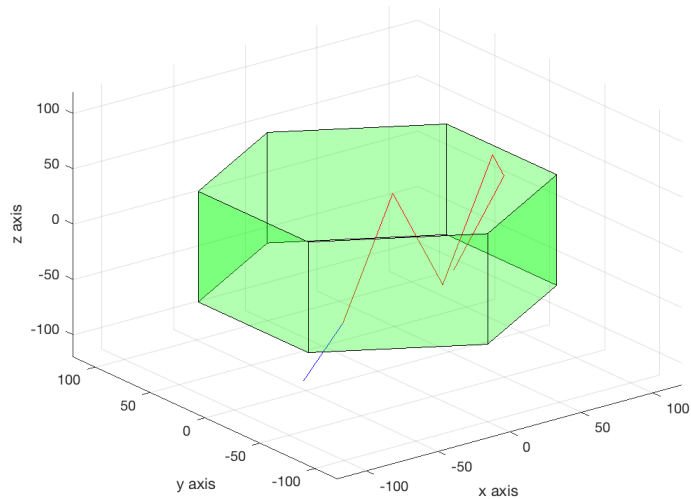


Figure 6.38: Single ray-tracing by a 3D hexagonal prism ice crystal

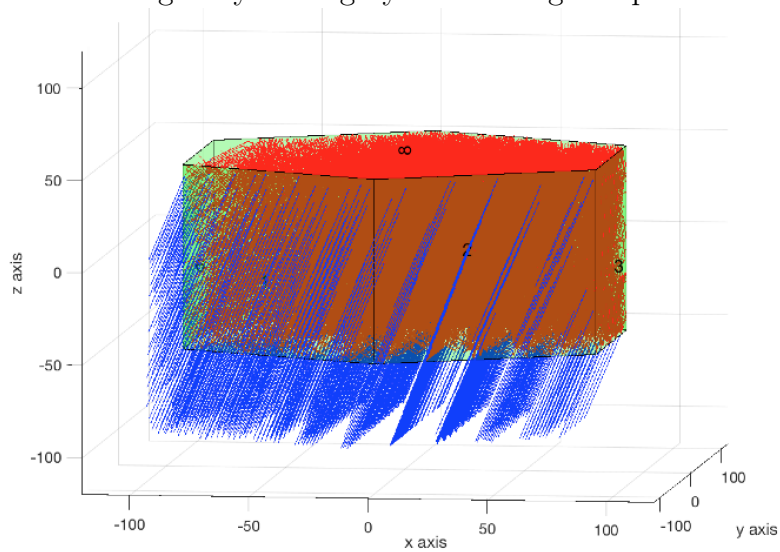


Figure 6.39: Multiple ray-tracing by a 3D hexagonal prism ice crystal

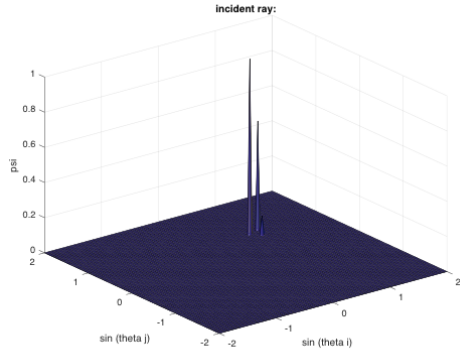


Figure 6.40: The incident field by hexagonal prism

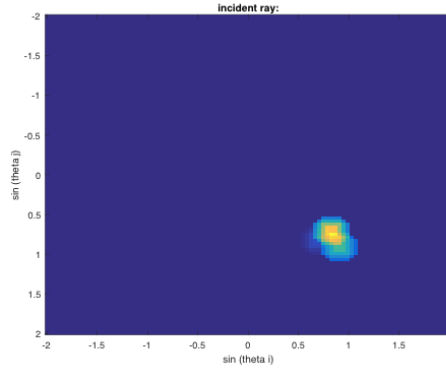


Figure 6.41: The incident field by hexagonal prism

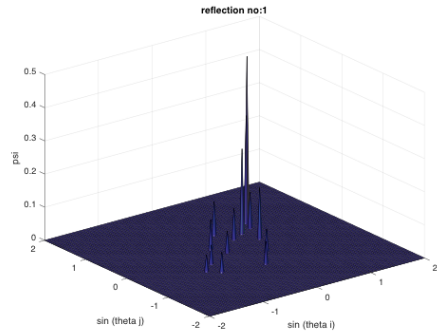


Figure 6.42: Field of 1st order of reflection in hexagonal prism

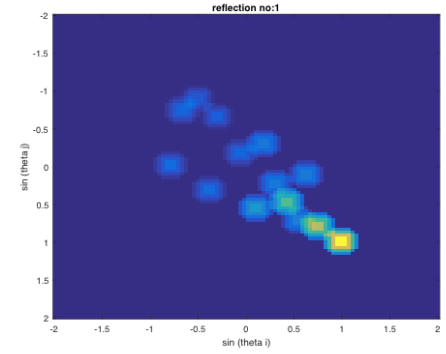


Figure 6.43: Field of 1st order of reflection in hexagonal prism

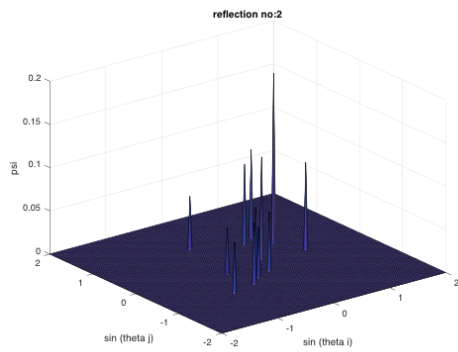


Figure 6.44: Field of 2nd order of reflection in hexagonal prism

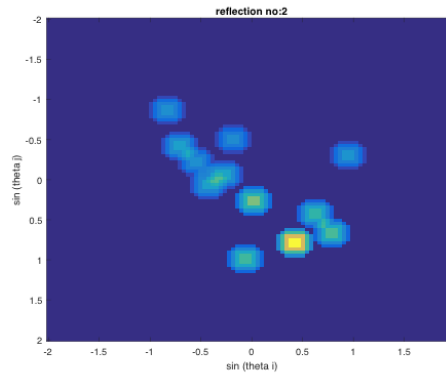


Figure 6.45: Field of 2nd order of reflection in hexagonal prism

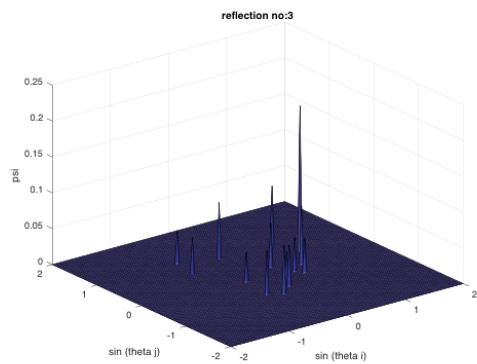


Figure 6.46: Field of 3rd order of reflection in hexagonal prism

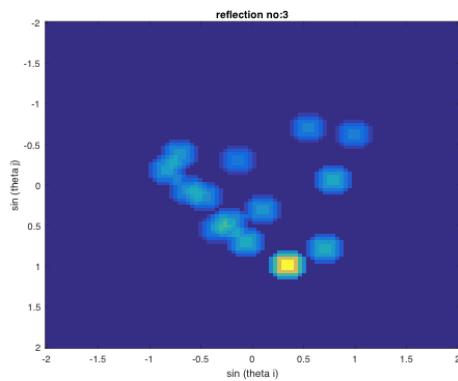


Figure 6.47: Field of 3rd order of reflection in hexagonal prism

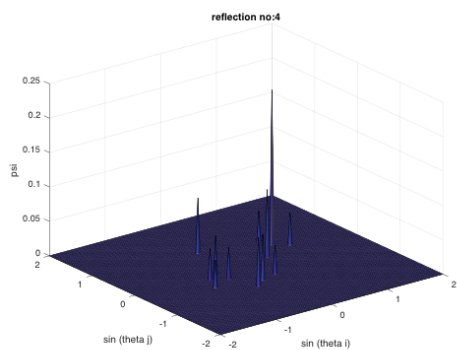


Figure 6.48: Field of 4th order of reflection in hexagonal prism

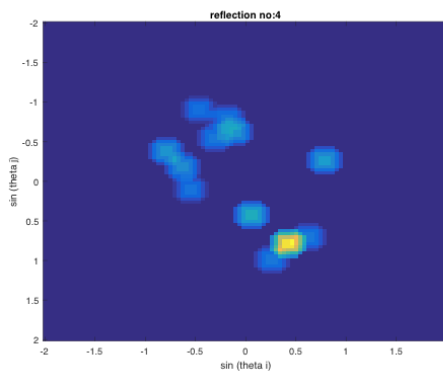


Figure 6.49: Field of 4th order of reflection in hexagonal prism

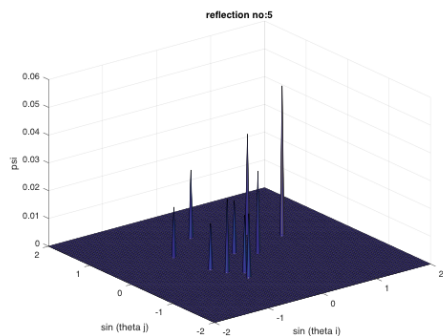


Figure 6.50: Field of 5th order of reflection in hexagonal prism

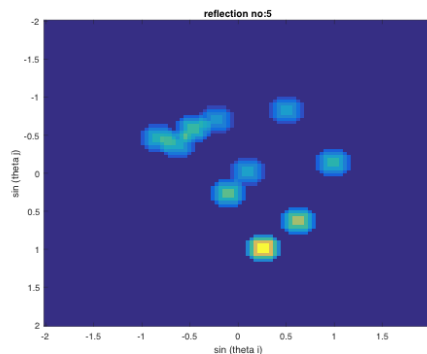


Figure 6.51: Field of 5th order of reflection in hexagonal prism

Figures 6.40 to 6.51 show the FFT of the total field magnitude for all facets with the shifts from the incident field until the fifth order reflection inside the hexagonal prism. Notably the field magnitude decreases as the number of reflection increases, also, the multiple shifts per reflections is more notable as the field is distributed in the facets. It is also worth mentioning that the field magnitude decreases as the number of reflection increases due to the scattered field outside the hexagonal prism per reflection. After finding the PO solution which shows the field locations and the magnitudes, the reaction theorem is going to be used in order to find the total scattered field.

6.4 3D ray-tracing and physical optics method for scattering by bullet shape ice crystals

6.4.1 Flowchart

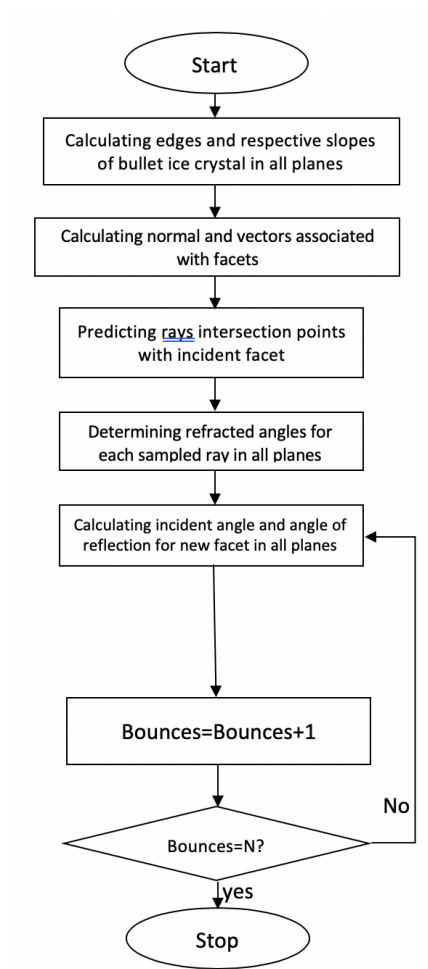


Figure 6.52: 3D ray-tracing by a bullet ice crystal flowchart

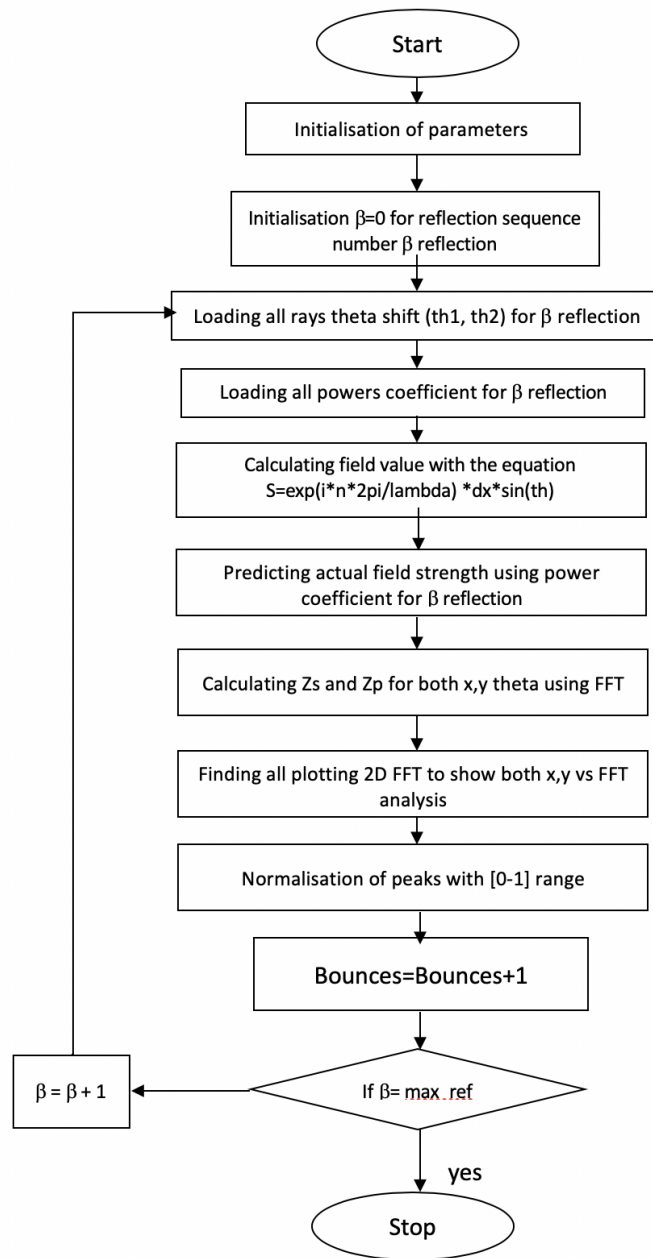


Figure 6.53: 3D PO by a bullet ice crystal flowchart

6.4.2 Results

The ray-tracing and PO results follow the same methodology as the triangular prism and hexagonal prism. The ray-tracing and PO results were made in a lossless case. The assumptions taken for the model were the angle of incidence to the bottom facet of the 3D hexagonal prism ice ($\Theta_i=30^\circ$), ($\Theta_j=30^\circ$) as in 3D we have two shifting angles, as discussed in Section 6.1.2, where the spherical coordinate system was used to plot in 3D, the refractive index outside the prism ($n_1=1$) and the refractive index of the hexagonal prism ($n_2=1.787$). The ray-tracing and PO results are shown in the following figures.

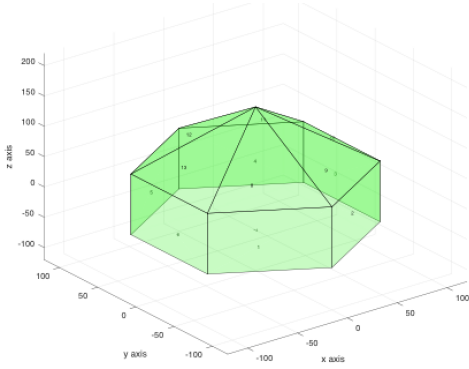


Figure 6.54: Bullet ice crystal

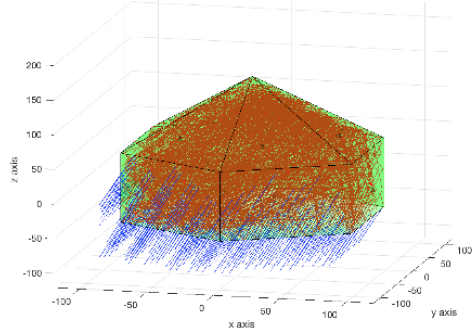


Figure 6.55: Multiple ray-tracing by a 3D bullet ice crystal

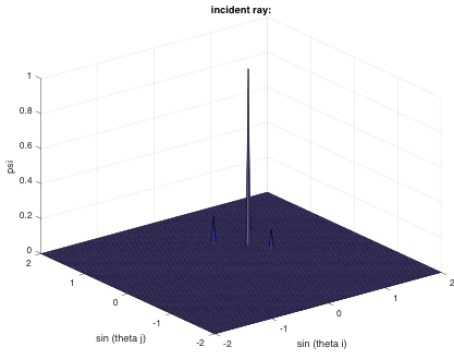


Figure 6.56: The incident field by bullet ice crystal

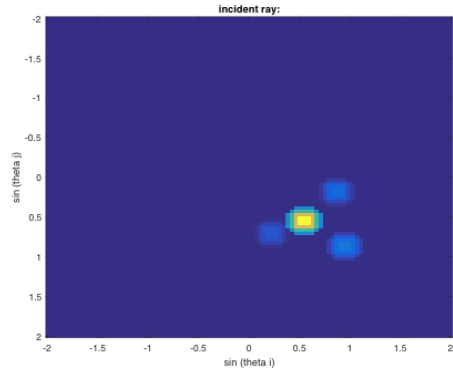


Figure 6.57: The incident field by bullet ice crystal

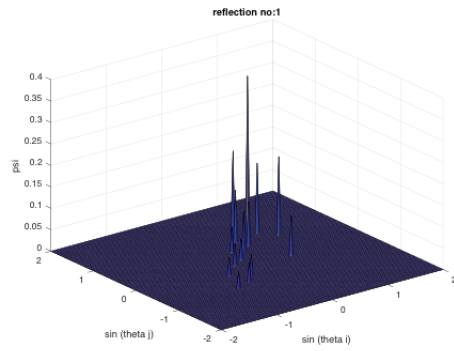


Figure 6.58: Field of 1st order of reflection in bullet ice crystal

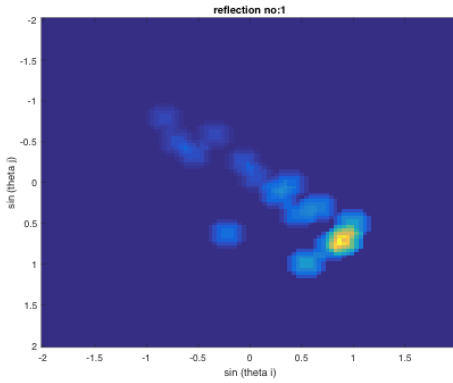


Figure 6.59: Field of 1st order of reflection in bullet ice crystal

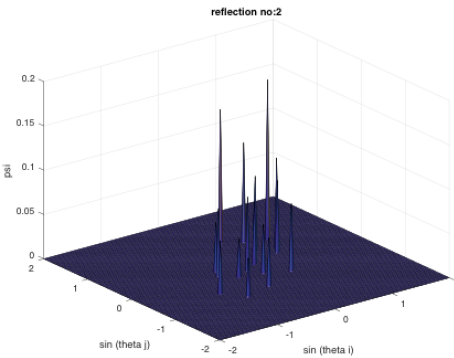


Figure 6.60: Field of 2nd order of reflection in bullet ice crystal

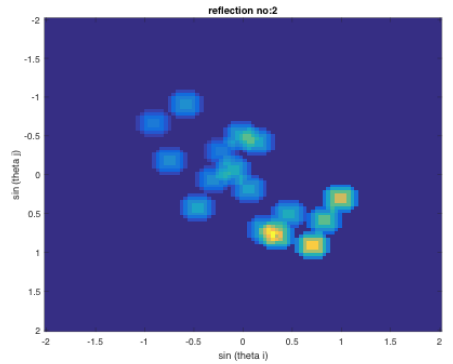


Figure 6.61: Field of 2nd order of reflection in bullet ice crystal

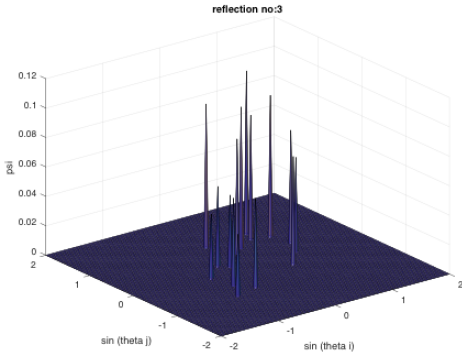


Figure 6.62: Field of 3rd order of reflection in bullet ice crystal

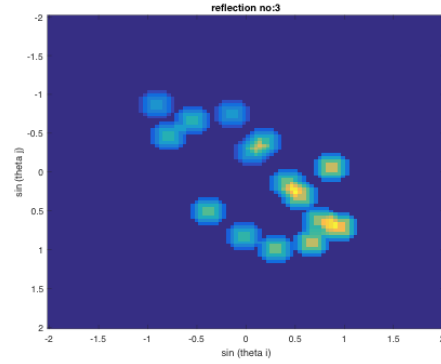


Figure 6.63: Field of 3rd order of reflection in bullet ice crystal

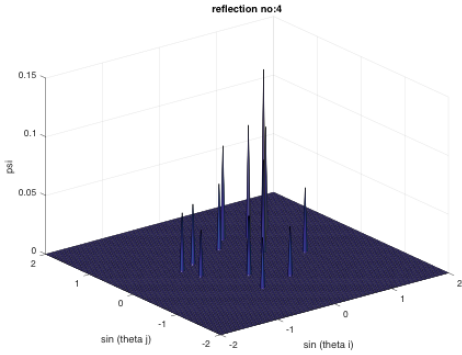


Figure 6.64: Field of 4th order of reflection in bullet ice crystal

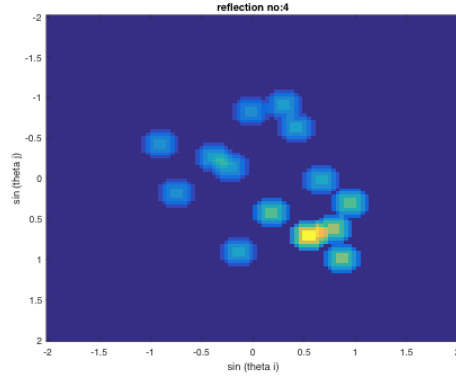


Figure 6.65: Field of 4th order of reflection in bullet ice crystal

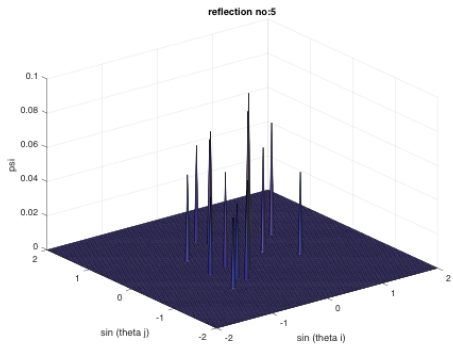


Figure 6.66: Field of 5th order of reflection in bullet ice crsytal

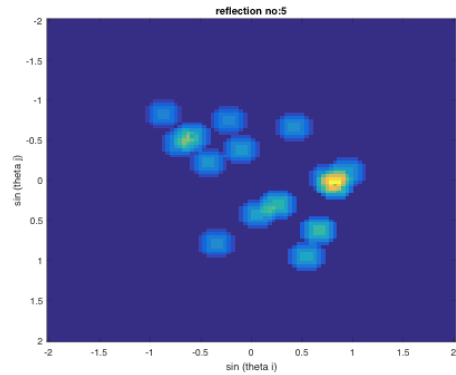


Figure 6.67: Field of 5th order of reflection in bullet ice crystal

Figures 6.56 to 6.67 show the FFT of the total field magnitude for all facets with shifts from the incident field until the fifth order reflection inside the bullet ice crystal. It can be noted that the field magnitude decreases as the number of reflections increases; also, the multiple shifts per reflections is more notable as the field is distributed in the facets. It is also worth mentioning that the field magnitude decreases as a number of reflection increases due to the scattered field outside the bullet ice crystal per reflection. After finding the PO solution, which shows the field locations and the magnitudes, the reaction theorem is going to be used in order to find the total scattered field.

6.5 Transformation of the volume integral to surface integral form

We consider the problem of computing the field scattering by a dielectric scatterer in some particular direction, in other words, to obtain the scattering amplitude. To motivate this, we imagine a distant receiving antenna, in which the scattered field causes a voltage V to be induced. Calibration of the antenna would enable us to deduce the amplitude of the wave scattered towards it. In our problem, we will be able to calculate the total scattered field by calculating the field inside the ice crystals.

If we suppose that a current I' impressed at the same time on the antenna terminals then there a reaction is said to exist between the received voltage and the current (that would independently cause the antenna to transmit), which is their direct product and has units of complex power. Reaction is a physical quantity, in principle measurable, and we can

consider I' as a ‘test’ current.

$$< V, I' > \quad (6.46)$$

In a scattering problem where the domain of interest involves only the scatterer and the antenna at ‘infinity’, within any arbitrary closed surface containing both entities, the total integrated reaction is zero. Given that there is no contribution in any volume element to the total reaction between two fields propagating in free space, it follows that the above quantity (6.46) is equal in value to a reaction integral involving the actual internal field of the scatterer and the field that would be radiated by the antenna due to I' .

Hence, when calculating the field scattered by a uniform dielectric obstacle in a particular direction, this can be achieved by evaluating the reaction between the electric component of the ‘test’ field that would have been present if radiated into free space by the receiving antenna and the polarisation current in the dielectric. In other words, an equality holds between the reactions.

$$\int_v E'(r) \bullet \frac{\partial}{\partial t} P(r) d^3r = - < V, I' > \quad (6.47)$$

Here, $P(r)$ is the polarization density in the dielectric that results from the field incident on it; $E'(r)$ is the field that the receiving antenna would radiate in the space occupied by the scatterer if it were not there, when a current I' was impressed on its terminals.

The artificial device of introducing a receiving antenna made to transmit a test field appears as somewhat artificial; however, in traditional approaches where the scattering amplitude involves a volume integral which has as the factor of an exponential wave solution prop-

agating in the opposite direction (i.e. inwards), leads to the correct answer but lacks a physical justification.

Instead, its justification arises through the application of a Fourier integral. From (6.47) it can be seen that we rely, in effect, on the Lorentz reciprocity theorem and the fact that the sum of the current in a volume enclosing both the scatterer and the antenna as a complete system is zero.

In a pure dialect with relative permittivity ϵ_r , the reaction integral (6.46) can further be simplified to

$$R_v = \int_V E'(r) \cdot (\epsilon_r - 1) \frac{\partial}{\partial t} E(r) d^3r \quad (6.48)$$

Now, consider a surface integral defined as

$$R_s = \int_s (E'(r) \times H(r) - E(r) \times H'(r)) \cdot dS \quad (6.49)$$

Where, again, primes denote the fields that would be present owing to the receiving antenna being driven by a current, and the unprimed fields being those which are included in and on the scatterer by the incident field. We can now apply the divergence theorem to convert the integral to a volume integral. Using the identity,

$$\nabla \cdot (F \times G) = G \cdot \nabla \times F - F \cdot \nabla \times G, \quad (6.50)$$

And then substituting for the curls using the appropriate Maxwell's equations, we have,

$$R_s = \int_V (E'(r) \cdot \frac{\partial D(r)}{\partial t} - R(r) \cdot \frac{\partial D'(r)}{\partial t}) d^3r$$

$$= \int_v (E'(r) \bullet (\epsilon_r - 1) \bullet \frac{\partial E(r)}{\partial t}) d^3r = R_v \quad (6.51)$$

In reaching this point, the magnetic scalar product terms cancel, and we assume that the scattered field and test field have the same time signature. The important point here is that the displacement for the primed field is what would apply in free space (but at locations which are interior to the scatterer) where the relative permittivity would be unity in the absence of the scatterer.

It is therefore seen that the surface integral (6.49) yields the same reaction integral as the volume integral, and therefore a knowledge of the electric and magnetic fields on the surface of a dielectric scatterer resulting in excitation by the incident field, which allows its scattering amplitude to be evaluated through an equivalent surface reaction integral, R_S involving the electric and magnetic components of a plane wave test field from a distant receive antenna. This, therefore, determines the scattering amplitude for the corresponding antenna polarisation. This formulation is equivalent to replacing the scatterer by a distribution of surface current elements that would give rise to the equivalent field internal, to the scatterer, but avoids having to introduce the dyadic Green's function. It is therefore more direct in applications involving physical optics where the emergent electric and magnetic fields are precisely what are calculated.

It is of interest to note that in that case, the reaction integral can be evaluated using either the fields on the internal surface of the scatterer (which must be the total fields, incident and reflected on the internal surface) or else the refracted field external to the surface. The boundary conditions in fact ensure that there will be continuity between the two reaction

integrals.

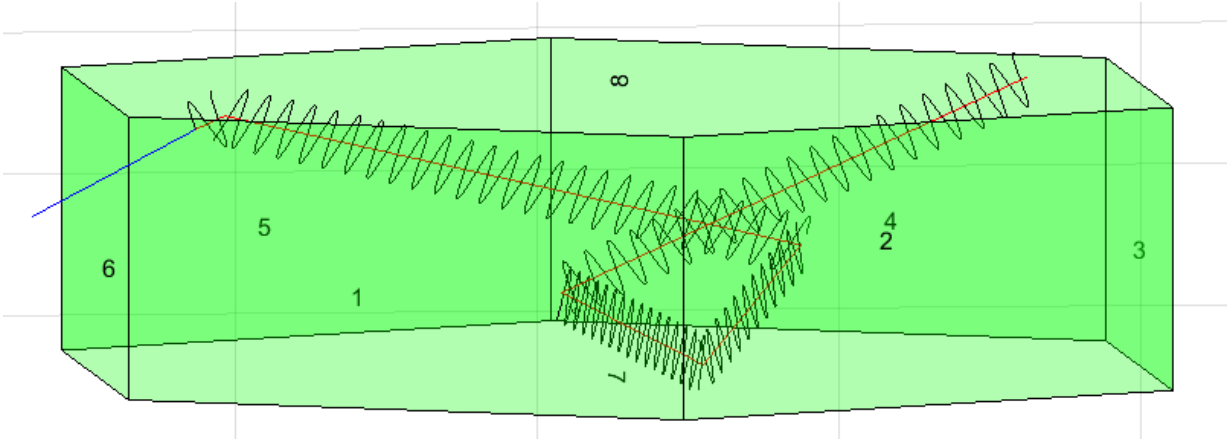


Figure 6.68: Wave vector components in hexagonal prism ice crystal

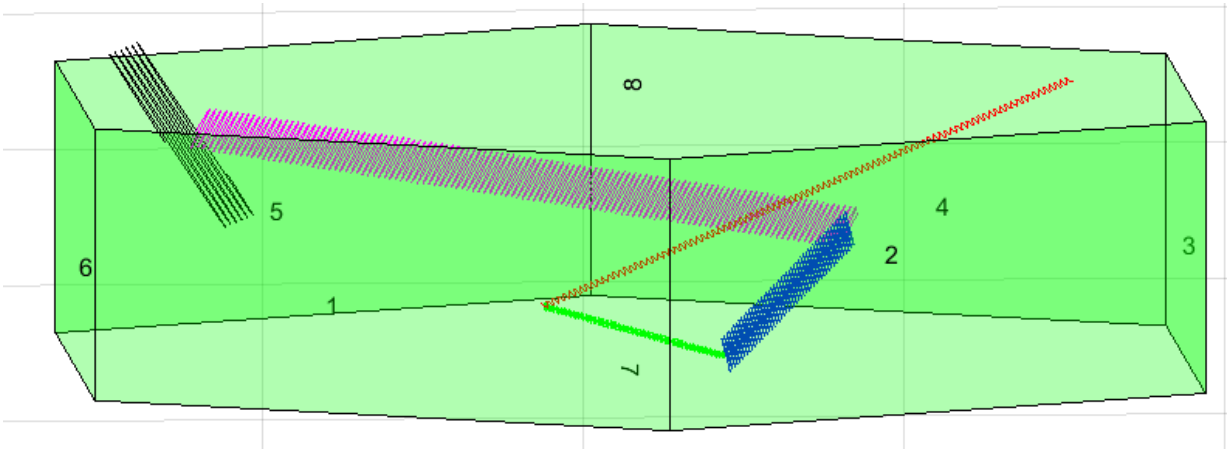


Figure 6.69: Wave vector components in hexagonal prism ice crystal

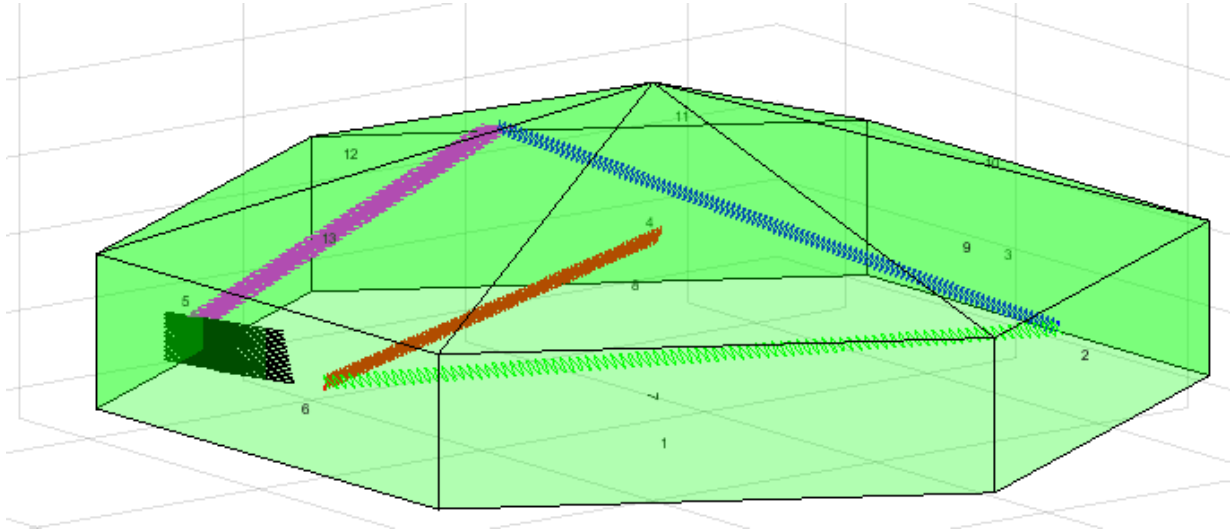


Figure 6.70: Wave vector components on bullet shape ice crystal

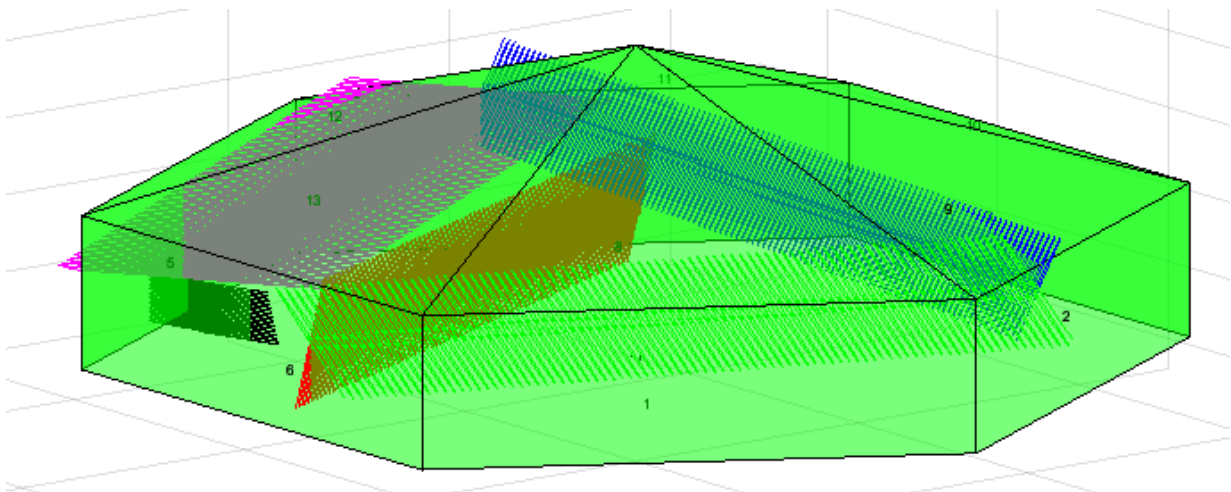


Figure 6.71: Wave vector components on bullet shape ice crystal

The figures above show the vector field that propagates through hexagonal prism and bullet ice crystal. After obtaining the vector field, the 2D FFT of the vector field will be represented and the reaction with different sources is analysed. In regards to the implementation, the reaction is between two fields and the total reaction, when evaluated as a surface integral, is between the total internal field as a result of the incident field and the field that would exist from an antenna at the point of observation.

If E and H are the internal fields and E' and H' are fields that would be emitted from the receiving antenna (as if it were emitting) then the reaction is:

$$R_S = \int (E \times H' - E' \times H) \cdot n \quad (6.52)$$

where n is the surface normal at each point on the facet. The reaction was done using the following psuedo code which shows the general algorithm of the reaction theorem implementation.

Algorithm 6.15 Reaction calculation

```
1: /incidence direction
2:  $\theta_2, \phi_2$  /theta and phi for incidence of the second plane wave (receiving antenna).
3:  $x = \sin(\theta_2) \cdot \cos(\phi_2)$ 
4:  $y = \sin(\theta_2) \cdot \sin(\phi_2)$ 
5:  $z = \cos(\theta_2)$ 
6: for  $i=1:\text{num\_ray}$  do
7:   for  $j=1:\text{max\_num\_reflections}$  do
8:     find the distance between points
9:      $E' = E_{\text{field}}(1 : 3) \times \exp(-jk * \text{distance})$ 
10:     $H' = H_{\text{field}}(1 : 3) \times \exp(-jk * \text{distance})$ 
11:     $V_1 = E \times H'$ 
12:     $V_2 = E' \times H$ 
13:     $\text{Reaction}_{\text{face}} = \text{Sum}(V_1 - V_2) \cdot \text{Normal}$ 
14:   end for
15: end for
```

The final results after applying the reaction theorem to compute the scattered field is shown in the next section. Also, the results were compared with other methods.

6.6 Scattering by a hexagonal prism results and comparisons

6.6.1 Problem statement

In this section, we analyse the scattering of an electromagnetic plane wave impinging on a hexagonal prism located in free-space (Figure 6.72). The prism basis is a regular hexagon with diameter d and its height is denoted with h . The prism is made of a lossless dielectric and non-magnetic material characterised by the refraction index n .

We introduce a Cartesian coordinate reference system having the z -axis aligned with the prism axis. A linearly and vertically polarised (i.e. directed along theta direction) plane wave impinges on the structure according to incidence angles (θ^i, ϕ^i) . A scattered field is produced inside the prism and in the surrounding space by the electromagnetic interaction phenomena.

We are interested in predicting the scattered far field at angles (θ, ϕ) and for the same polarisation of the incident field (co-polarisation VV).

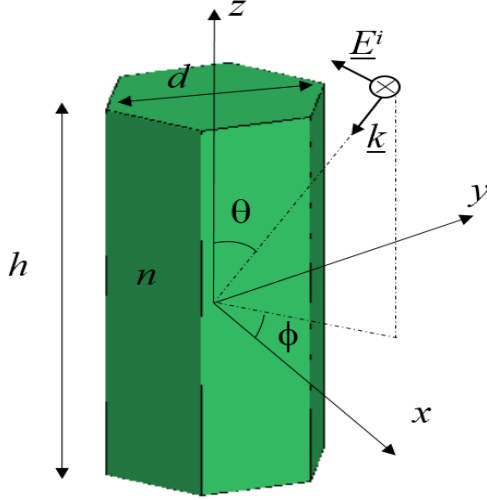


Figure 6.72: Geometry of the scattering problem

6.6.2 Solution approach

The goal of the study is to assess the accuracy of the physical optics (PO) solution proposed in this thesis. PO is an asymptotic method valid at high frequencies, i.e. when the characteristic size of the structure is much larger than the electromagnetic wavelength λ . Therefore, the analysis carried out mainly considers electrically large prisms.

The validation of the PO approach is accomplished by resorting to a numerical code implementing the Method of Moments (MoM) [134], [135]. It is well-known that MoM is a popular numerical technique used to determine the unknown current distributions (electric and/or magnetic) of radiating or scattering structures by solving proper integral equations. Depending on the method formulation, the current distribution can be superficial or volumetric. MoM is an exact method that provides a full-wave solution of Maxwell's integral

equations in the frequency domain. An advantage of the MoM over other ‘field methods’, such as Finite Element Method (FEM) or Finite Difference Time Domain (FDTD) technique, is that it is a ‘source method’, i.e. only the structure of interest is discretised.

Despite that, the application of MoM is computationally burdensome and even prohibitive when dealing with electrically large scattering structures. Therefore, some variants of the method have been developed attempting to reduce the computation effort of standard MoM approach. For instance, at high frequency, the MoM can be hybridised with PO [136], Geometrical Optics (GO) [137] or Uniform Theory of Diffraction (UTD) [138].

In this study, unless otherwise stated, we have considered as a reference solution that obtained with MoM combined with GO, where ray-launching and transmission, reflection and refraction theory is used to model the interaction between the dielectric region and the MoM. The method is referred to as ray launching GO (RL-GO).

6.6.3 Numerical results

In this section, we report the results of the numerical tests aimed to validate the PO solution for the scattering by a hexagonal prism. For the simulations, the plane wave incidence direction is fixed at $\theta^i=180^\circ$, i.e. the wave impinges normally on the bottom face of the prism. The electromagnetic wavelength is $\lambda=2\ \mu m$. The amplitude of the scattered field is evaluated over the planes $\phi=0^\circ, 90^\circ$ versus the elevation angle $\theta \in [-180^\circ, 180^\circ]$, where $\theta=0^\circ$ corresponds to the forward scattering direction.

We started by considering a dielectric prism characterised by a refraction index $n=1.787$, diameter $d=10\ \mu m$ and height $h=20\ \mu m$. The amplitude of the scattered field (normalised to the maximum) evaluated by the PO solution is compared with that provided by the RL-GO method in both elevation planes (Figures 6.73 and 6.74). It can be seen that both field patterns exhibit a radiation maximum when $\theta=0^\circ$. This result is physically intuitive since the scattered field is expected to have a maximum in the forward scattering direction for a wave normally incident on the bottom face of the prism. Moreover, the field patterns have some minor lobes and there is some significant scattering at angles $\theta=\pm 180^\circ$, i.e. in backscattering direction.

in figures 6.73 and 6.74, Both scattered field patterns confirm that the PO solution (blue curve) is in good agreement with that provided by RL-GO method (black curve) in the whole angular interval. Indeed, there are only slight differences on the sidelobes level. Such differences, probably imputable to computation errors, can be considered negligible from an engineering viewpoint.

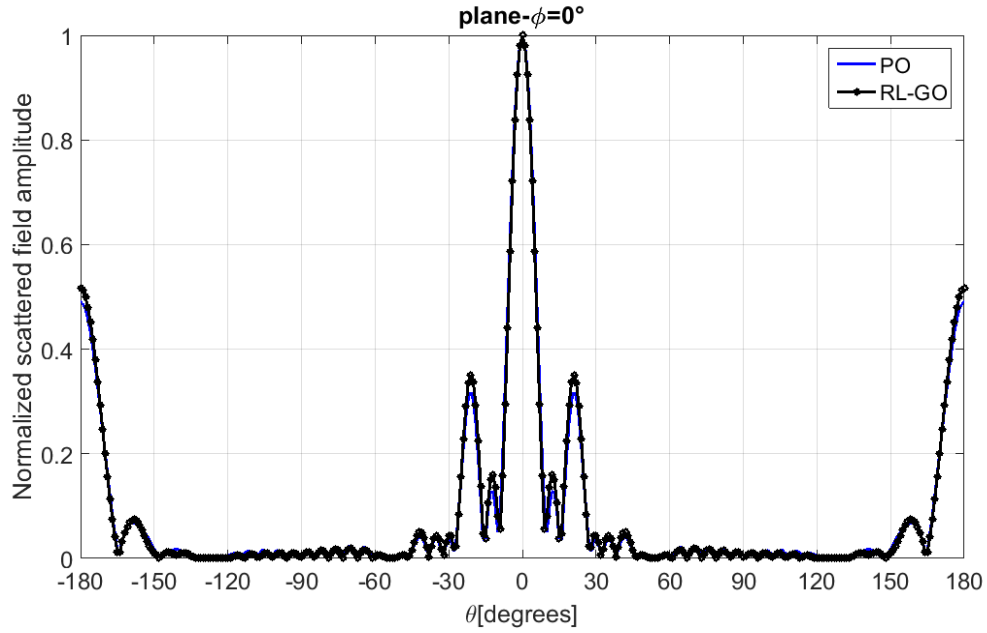


Figure 6.73: Relative amplitude of the scattered field at $\phi = 0^\circ$. Prism parameters: $n=1.787$, $d=10 \mu m$, $h=20 \mu m$, $\lambda = 2 \mu m$, estimated error=0.664%

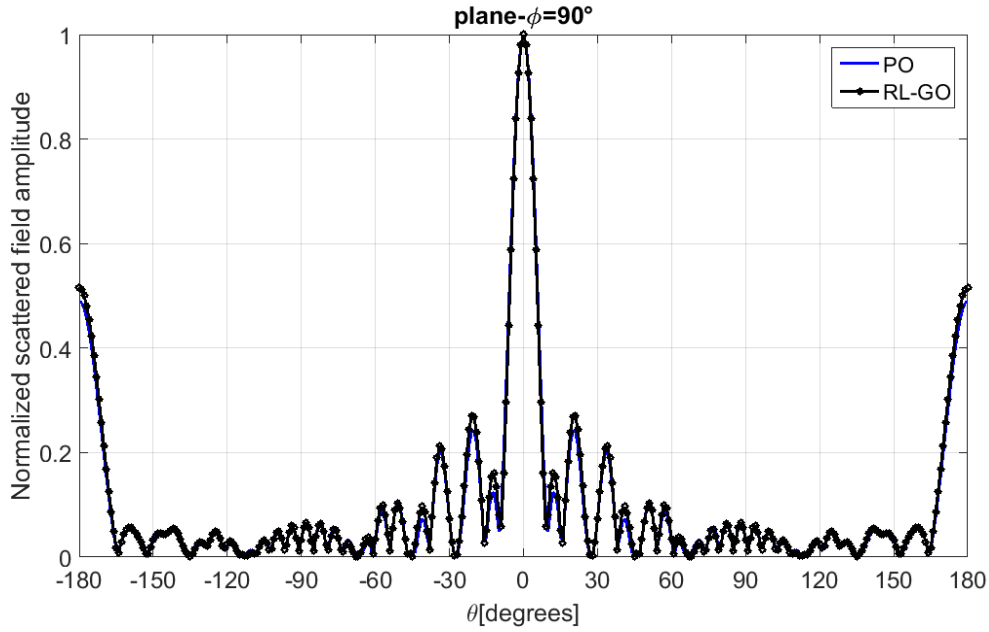


Figure 6.74: Relative amplitude of the scattered field at $\phi = 90^\circ$. Prism parameters: $n=1.787$, $d=10 \mu m$, $h=20 \mu m$, $\lambda = 2 \mu m$, estimated error= 3.745%

Next, we considered a hexagonal prism with a larger diameter ($d=20\ \mu m$) while the remaining parameters are those considered in the previous example. It is seen that both PO and RL-GO solutions are also in good agreement in this case (Figures 6.75 and 6.76). Most notably, it appears that the agreement between the two methods is good with error margin less than 5% (see the estimated error in the figures which shows the difference in percentage between PO and RL-GO), suggesting that PO and RL-GO methods perform more similarly for larger structures.

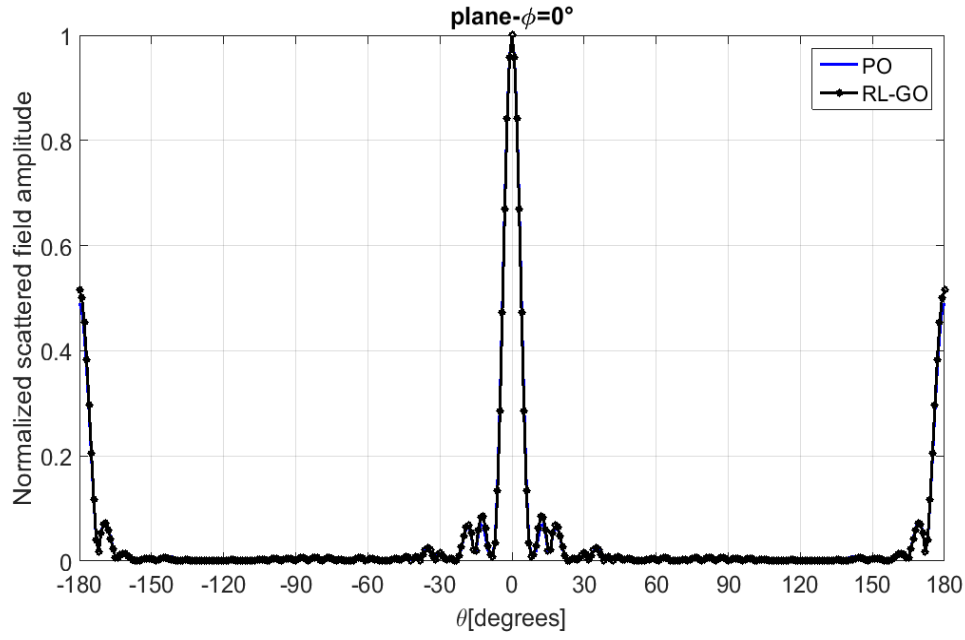


Figure 6.75: Relative amplitude of the scattered field at $\phi = 0^\circ$. Prism parameters: $n=1.787$, $d=20 \mu m$, $h=20 \mu m$, $\lambda = 2 \mu m$, estimated error=0.398%

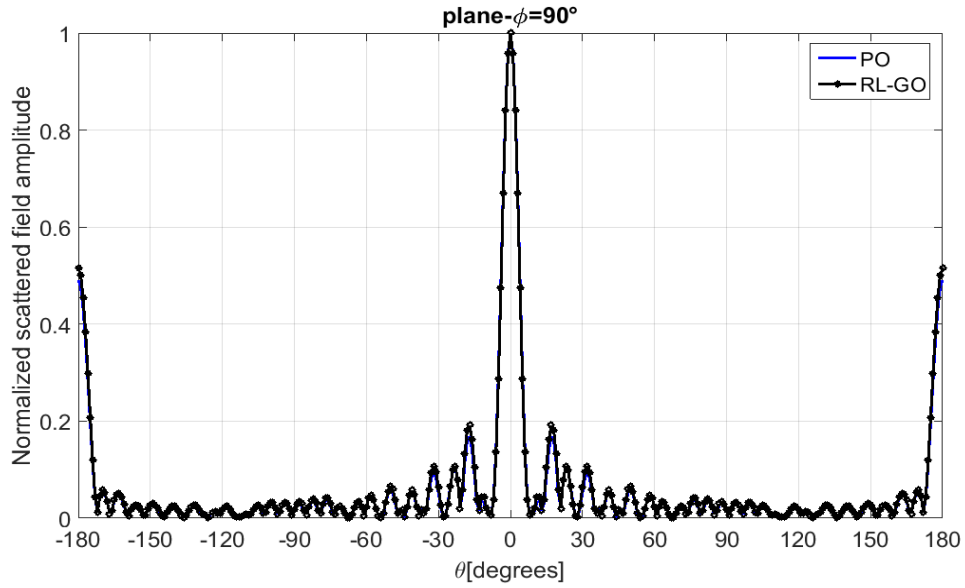


Figure 6.76: Relative amplitude of the scattered field at $\phi = 90^\circ$. Prism parameters: $n=1.787$, $d=20 \mu m$, $h=20 \mu m$, $\lambda = 2 \mu m$, estimated error=4.46%

The next example deals with a hexagonal prism that is smaller in size. The prism height $h=5\ \mu m$ and diameter $d=5\ \mu m$ are now comparable to the wavelength ($2\ \mu m$). We expect that both PO and RL-GO methods are less accurate because they are based on the ray approximation, which holds in the high frequency regime. Therefore, this test is interesting since it allows appreciation of the limits of applicability of the PO solution. In order to have a reliable reference solution for the considered case, the standard MoM method is applied and compared to PO and RL-GO as shown in Figures 6.77 and 6.78. As can be observed, the PO solution (blue curve) and the RL-GO one (black curve) look similar and are substantially different from the MoM solution (red dashed curve). Most notably, while the MoM pattern has a clear and well-defined radiation maximum in the forward scattering direction, PO and RL-GO have a more oscillatory behaviour with various lobes and have similar amplitude. In addition, the PO seems to provide a slightly better approximation than RL-GO as compared to MoM. However, as any asymptotic method, it is not reliable to predict the scattering by objects with size comparable to the wavelength.

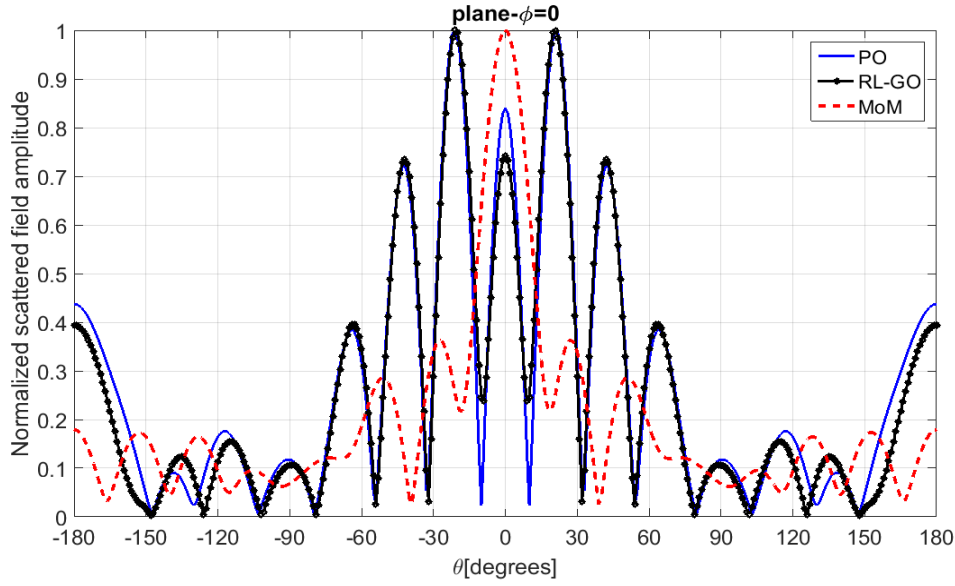


Figure 6.77: Relative amplitude of the scattered field at $\phi = 0^\circ$. Prism parameters: $n=1.787$, $d=5 \mu m$, $h=5 \mu m$, $\lambda=2 \mu m$

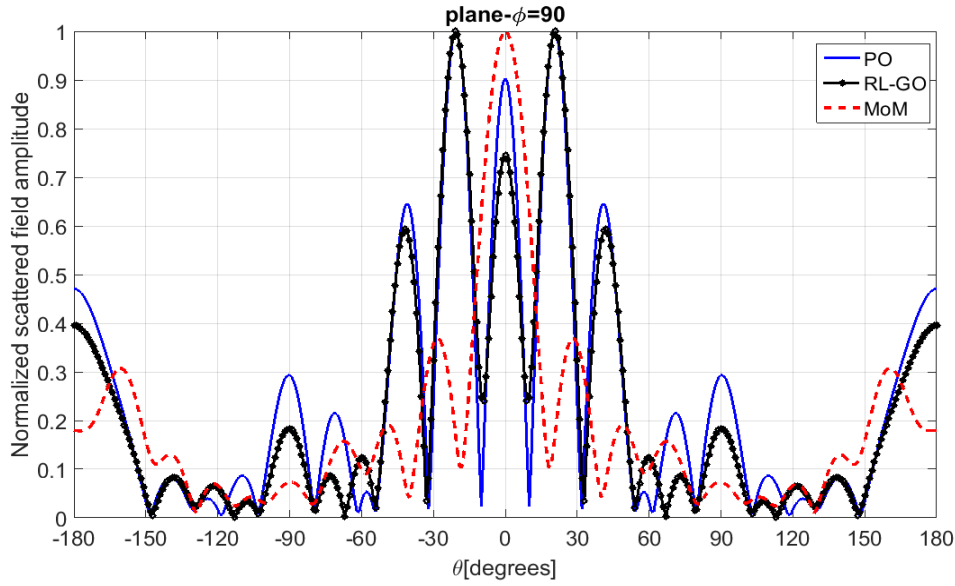


Figure 6.78: Relative amplitude of the scattered field at $\phi = 90^\circ$. Prism parameters: $n=1.787$, $d=5 \mu m$, $h=5 \mu m$, $\lambda=2 \mu m$

In the following, we analyse the response of the hexagonal prism for a different refractive index. In particular, we consider a hexagonal prism with a lower refraction index, characterised by the following parameters: $n=1.33$, $d=10\ \mu m$, $h=10\ \mu m$. The selected value of the refraction index has a physical justification since it allows simulation of the wave scattering by an ice crystal. As confirmed by Figures 6.79 and 6.80, a very good agreement between PO and RL-GO solution can also be observed in this case.

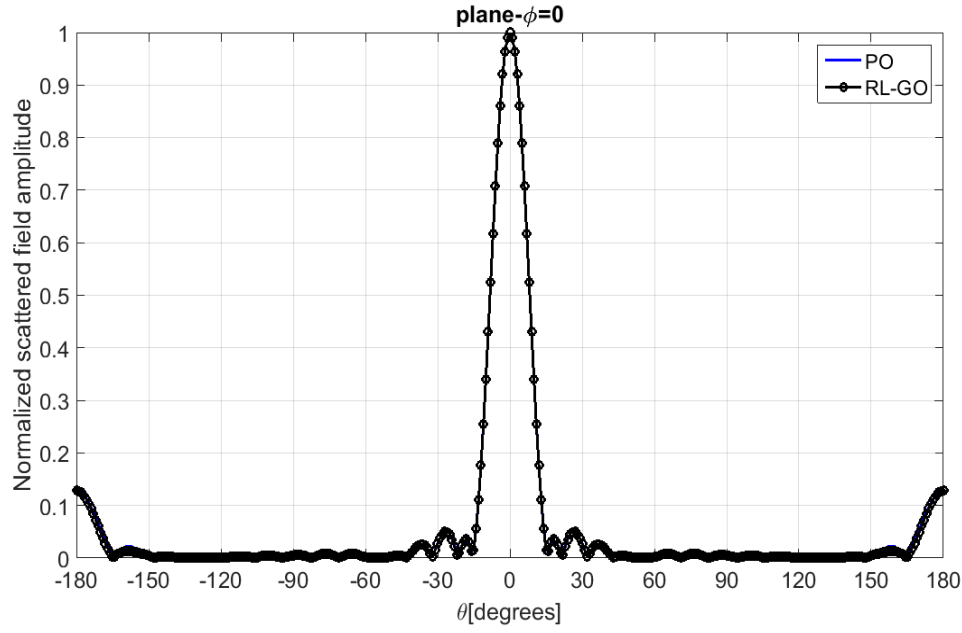


Figure 6.79: Relative amplitude of the scattered field at $\phi = 0^\circ$. Prism parameters: $n=1.33$, $d=10\text{ }\mu m$, $h=10\text{ }\mu m$, $\lambda=2\text{ }\mu m$, estimated error=2.06%

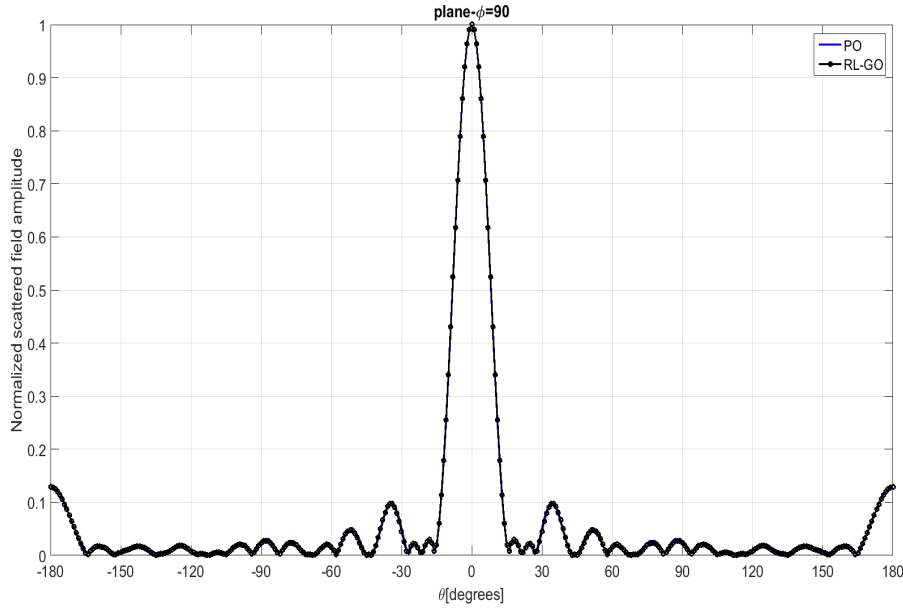


Figure 6.80: Relative amplitude of the scattered field at $\phi = 90^\circ$. Prism parameters: $n=1.33$, $d=10\text{ }\mu m$, $h=10\text{ }\mu m$, $\lambda=2\text{ }\mu m$, estimated error=0.41%

Finally, we conclude this experimentation by including an example of plane wave illumination at oblique incidence. We consider a thin prism with the following parameters: $n=1.33$, $d=10\text{ }\mu\text{m}$, $h=2\text{ }\mu\text{m}$. In this way, the propagation effects through lateral faces of the prism are minimised. The plane wave incidence direction is fixed at $\theta^i=160^\circ$, $\phi^i=0^\circ$. The curves plotted in Figure 6.81 show the comparison between the PO and RL-GO solution. It can be seen that the PO solution is very accurate in the forward scattering region (i.e. around $\theta=-20^\circ$) and similar to RL-GO at the specular reflection direction (around $\theta=-160^\circ$).

Finally, for sake of completeness, Figure 6.82 shows the 3D scattering pattern as achieved with the RL-GO method. The figure highlights that most radiation is concentrated in the forward scattering direction and a smaller part is associated with specular reflection.

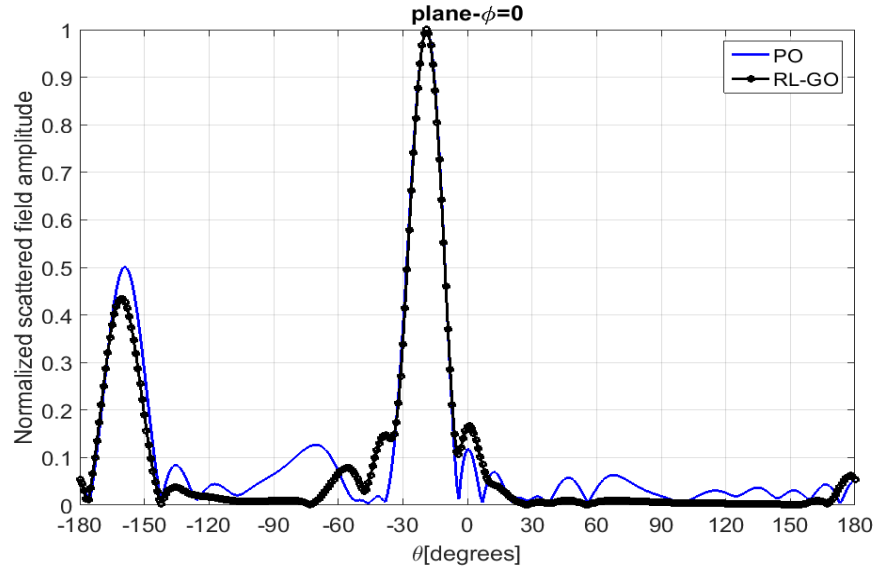


Figure 6.81: Relative amplitude of the scattered field at $\phi = 0^\circ$. Prism parameters: $n=1.33$, $d= 10 \mu m$, $h=2 \mu m$, $\lambda =2 \mu m$. Plane wave incidence direction: $\theta^i=160^\circ$, $\phi^i=0^\circ$, estimated error=14%

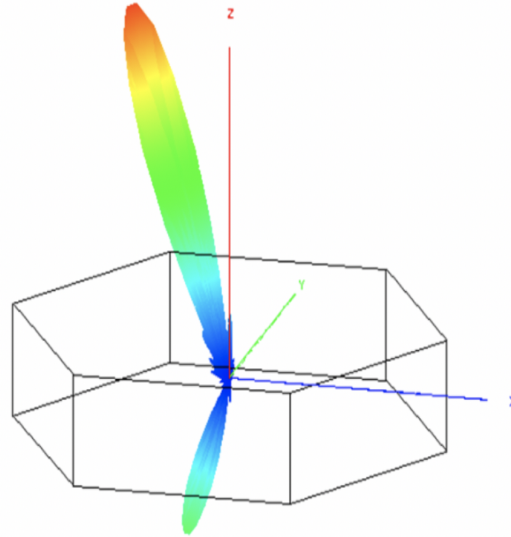


Figure 6.82: 3D scattering pattern obtained with RL-GO method

In summary, this section has provided an assessment of the accuracy of the PO solution for the scattering by a hexagonal dielectric prism. The PO solution has been compared to a reference solution based on a hybrid method combining the MoM and GO technique, referred as RL-GO. In a normal incidence case, the PO solution is accurate enough as the RL-GO one when the size of the structure is relatively large in terms of the wavelength. On the other hand, when the object size is comparable to the wavelength, both PO and RL-GO methods fail in providing a reliable scattered field pattern since ray approximation, at the basis of both methods, is no longer valid. At oblique incidence, the PO method is in good agreement with RL-GO in the neighbourhood of forward scattering and specular reflection directions.

7 — Conclusion and future work

An approach based on a PO model of electromagnetic scattering by pristine ice crystals at infrared wavelength has been presented. We consider that the scattered field depends entirely on the field distribution internally to the ice crystal. In addition, this model was implemented by considering that the scatterer is homogenous.

In order to solve the problem of scattering by ice crystals, we considered the classical problem of a wedge, which was used as a proof that the method is working in principle. The method was compared to ray-tracing in terms of field shifting. The results for both the physical optics method and ray-tracing is included in the thesis. Then, the complexity was increased proportionally by progressing on 3D PO and ray-tracing of both triangular prism, hexagonal prism and bullet shape ice crystals, which are also included in the thesis.

In summary, the process started with a plane wave which is incident to a crystal by treating every facet that the plane wave is incident on. Then, the transmission was calculated through that facet. In the first instance, certain amplitude comes through the ice crystals towards the other facets. This was done with individual rays. Then, the vector components that are parallel to the facets were considered as they are vector components that are normal to the facet. Then, the third component can be worked out because the square of the wave number is determined by the refractive index. The vector components on each facet act as sources of the field that propagates towards other facets. Since the

calculations for the rays vector components are modified by the rotation of different facets, the same method was used for the wave vector components that are part of the aperture distribution. On every pixel of a facet, there is a vector amplitude within that facet. Hence, the vector amplitudes on other facets can be calculated by the Fourier Transform method, which is needed. The Fourier method that is already known that it works. Also, k vector scaling was used which is already proven to work. Instead of using the scalar values (2D), the vector values is used (3D). The only difference is that instead of having scalar amplitudes, we are going to have vector amplitudes. So as it was done for individual ray components, it was also done for the vector components. Then, the total scattered field was evaluated by application of reaction theorem to a volume interval by determining the internal field distribution, which is converted to an integral over the equivalent surface current distribution.

Lastly, Section 6.6 provides insight into how accurate the proposed solution is with regards to scattering by a hexagonal dielectric prism. Furthermore, comparison is made between the PO solution and an alternative reference solution (RL-GO) that employs a hybrid approach integrating the MoM and GO technique. When faced with a standard incidence case and a relatively large wavelength, the PO solution is deemed sufficiently accurate. Furthermore, the PO solution corresponds with the RL-GO at oblique incidence when there forward scattering and specular reflection directions. Conversely, scattered field patterns are unreliable for both the PO solution and the RL-GO method when the wavelength and object size are similar. This is because ray approximation which supports both methods is not valid in such circumstances.

In regards to the future work, this method in principle can readily be modified to consider

rough surface realistically. Hence, the surface irregularities and perturbations could be considered. The rough surface model can be simplified as shown in the figure below.

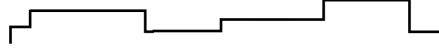


Figure 7.1: Rough surface schematic

The figure above shows an overview schematic of a rough surface. It can be noted that the rough surface model will play a major role in the variation of phase delay compared to the smooth model. Also, this work will allow the investigation of different roughness scales to different size parameters as it could be compared to the smooth surface case. We can test how roughness will reduce the prominent features of scattering by pristine shapes.

There are various studies which have mentioned the rough surface model including [10] and [139]. In these studies, The Guassian random surface was used where the height varies as a function of x and y . This method can be adopted to the rough surface model in future works.

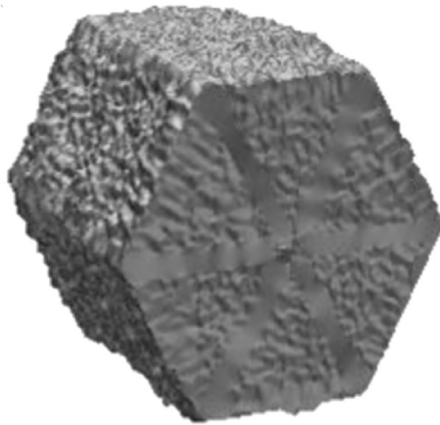


Figure 7.2: Rough surface model using Guassian Height Distribution [10]

Bibliography

- [1] Y. Takano and K. Liou, “Radiative transfer in cirrus clouds. part iii: Light scattering by irregular ice crystals,” *Journal of the atmospheric sciences*, vol. 52, no. 7, pp. 818–837, 1995.
- [2] WW2010, “Cirrus clouds,” 2010, available at: [http://ww2010.atmos.uiuc.edu/\(Gh\)/guides/mtr/cld/cldtyp/hgh/crs.rxml](http://ww2010.atmos.uiuc.edu/(Gh)/guides/mtr/cld/cldtyp/hgh/crs.rxml).
- [3] C. C. Atlas, “California community cloud atlas. a smile in the sky,” 2014, available at: <https://communitycloudatlas.wordpress.com/tag/california/>.
- [4] A. Lipson, S. G. Lipson, and H. Lipson, *Optical physics*. Cambridge University Press, 2010.
- [5] Hyperphysics, “Fraunhofer single-slit diffraction,” 2017, available at: <http://hyperphysics.phy-astr.gsu.edu/hbase/phyopt/sinslit.html>.
- [6] M. Born and E. Wolf, *Principles of optics: electromagnetic theory of propagation, interference and diffraction of light*. Cambridge university press, 1999.
- [7] T. Francis and X. Yang, *Introduction to optical engineering*. Cambridge University Press, 1997.

- [8] M. Frongillo, “Diffraction by dielectric wedges: high frequency and time domain solutions,” *PhD Thesis*, 2016.
- [9] G. Gennarelli and G. Riccio, “A uniform asymptotic solution for diffraction by a right-angled dielectric wedge,” *IEEE Transactions on Antennas and Propagation*, 2010.
- [10] E. Hesse, L. Taylor, C. T. Collier, A. Penttilä, T. Nousiainen, and Z. Ulanowski, “Discussion of a physical optics method and its application to absorbing smooth and slightly rough hexagonal prisms,” *Journal of Quantitative Spectroscopy and Radiative Transfer*, vol. 218, pp. 54–67, 2018.
- [11] E. Hesse, C. Collier, A. Penttilä, T. Nousiainen, Z. Ulanowski, and P. H. Kaye, “Modelling light scattering by absorbing smooth and slightly rough faceted particles,” *Journal of Quantitative Spectroscopy and Radiative Transfer*, vol. 157, pp. 71–80, 2015.
- [12] J. B. Keller, “Geometrical theory of diffraction,” *Journal of the Optical Society of America*, vol. 52, no. 2, pp. 116–130, 1962.
- [13] R. G. Kouyoumjian and P. H. Pathak, “A uniform geometrical theory of diffraction for an edge in a perfectly conducting surface,” *Proceedings of the IEEE*, vol. 62, no. 11, pp. 1448–1461, 1974.
- [14] M. Frongillo, G. Riccio, and G. Gennarelli, “Time domain diffraction coefficients for a lossless acute-angled wedge.”

- [15] Y. T. Liou, J. N. and P. Yang, “Light scattering and radiative transfer in ice crystal clouds: Applications to climate research,” *Light Scattering by Nonshperical Particles: Theory, Measurements, and Geophysical Applications*, no. 15, 1999.
- [16] K. Wyser and D. Mitchell, “Parameterization of the scattering and absorption properties of individual ice crystals,” *Journal of geophysical research*, vol. 105, no. D4, pp. 4699–4718, 2000.
- [17] P. C. Chang, R. J. Burkholder, R. J. Marhefka, and J. L. Volakis, “Diffraction coefficients for dielectric wedges and corners with application to monostatic building imaging,” *IEEE Transactions on Geoscience and Remote Sensing*, 2009.
- [18] G. Gennarelli and G. Riccio, “Plane-wave diffraction by an obtuse-angled dielectric wedge,” *JOSA A*, vol. 28, no. 4, pp. 627–632, 2011.
- [19] A. Macke, M. I. Mishchenko, and B. Cairns, “The influence of inclusions on light scattering by large ice particles,” *Journal of Geophysical Research: Atmospheres (1984–2012)*, vol. 101, no. D18, pp. 23311–23316, 1996.
- [20] A. J. Baran, “From the single-scattering properties of ice crystals to climate prediction: A way forward,” *Atmospheric Research*, vol. 112, pp. 45–69, 2012.
- [21] Z. Lou, “An analytical study of diffraction by dielectric wedges,” *Center for Computational Electromagnetics*, 2003.
- [22] J. Radlow, “Diffraction by a right-angled dielectric wedge,” *International Journal of Engineering Science*, vol. 2, no. 3, pp. 275–290, 1964.

- [23] A. J. Heymsfield, M. Krämer, A. Luebke, P. Brown, D. J. Cziczo, C. Franklin, P. Lawson, U. Lohmann, G. McFarquhar, Z. Ulanowski, *et al.*, “Cirrus clouds,” *Meteorological Monographs*, vol. 58, pp. 2–1, 2017.
- [24] W. M. Organization, *International cloud atlas*, vol. 1. World Meteorological Organization, 1956.
- [25] AMS, “Cirrus: Glossary of meteorology,” 2012, available at: <http://glossary.ametsoc.org/wiki/Cirrus>.
- [26] G. Ritter, “The growth and morphology of small ice crystals in a diffusion chamber,” *University of Hartfordshire*, 2015.
- [27] K. Sassen, Z. Wang, and D. Liu, “Global distribution of cirrus clouds from cloudsat/cloud-aerosol lidar and infrared pathfinder satellite observations (calipso) measurements,” *Journal of Geophysical Research: Atmospheres*, vol. 113, no. D00A12, 2008.
- [28] K. Eleftheratos, C. Zerefos, P. Zanis, D. Balis, G. Tselioudis, K. Gierens, and R. Sausen, “A study on natural and manmade global interannual fluctuations of cirrus cloud cover for the period 1984–2004,” *Atmospheric Chemistry and Physics*, vol. 7, no. 10, pp. 2631–2642, 2007.
- [29] P. Spichtinger, K. Gierens, and W. Read, “The global distribution of ice-supersaturated regions as seen by the microwave limb sounder,” *Quarterly Journal of the Royal Meteorological Society: A journal of the atmospheric sciences, applied meteorology and physical oceanography*, vol. 129, no. 595, pp. 3391–3410, 2003.

- [30] A. Guignard, C. Stubenrauch, A. Baran, and R. Armante, “Bulk microphysical properties of semi-transparent cirrus from airs: a six year global climatology and statistical analysis in synergy with geometrical profiling data from cloudsat-calipso,” *Atmospheric Chemistry and Physics*, vol. 12, no. 1, pp. 503–525, 2012.
- [31] A. K. Heidinger and M. J. Pavolonis, “Global daytime distribution of overlapping cirrus cloud from noaas advanced very high resolution radiometer,” *Journal of Climate*, vol. 18, no. 22, pp. 4772–4784, 2005.
- [32] A. Korolev, J. Strapp, and G. Isaac, “Evaluation of the accuracy of pms optical array probes,” *Journal of Atmospheric and Oceanic Technology*, vol. 15, no. 3, pp. 708–720, 1998.
- [33] J. A. Sellberg, C. Huang, T. A. McQueen, N. Loh, H. Laksmono, D. Schlesinger, R. Sierra, D. Nordlund, C. Hampton, and D. Starodub, “Ultrafast x-ray probing of water structure below the homogeneous ice nucleation temperature,” *Nature*, vol. 510, no. 7505, p. 381, 2014.
- [34] M. Matsumoto, S. Saito, and I. Ohmine, “Molecular dynamics simulation of the ice nucleation and growth process leading to water freezing,” *Nature*, vol. 416, no. 6879, p. 409, 2002.
- [35] L. S. Bartell, “Diffraction studies of clusters generated in supersonic flow,” *Chemical Reviews*, vol. 86, no. 3, pp. 491–505, 1986.
- [36] V. Buch*, B. Sigurd, J. Paul Devlin, U. Buck, and J. K. Kazimirski, “Solid water clusters in the size range of tens–thousands of h₂o: a combined computa-

- tional/spectroscopic outlook,” *International Reviews in Physical Chemistry*, vol. 23, no. 3, pp. 375–433, 2004.
- [37] C. Hoose, “Interactive comment on heterogeneous ice nucleation on atmospheric aerosols: a review of results from laboratory experiments by c. hoose and o. möhler,” *Atmospheric Aerosol Research, Karlsruhe Institute of Technology, Karlsruhe, Germany*, 2012.
- [38] B. Murray, D. O’sullivan, J. Atkinson, and M. Webb, “Ice nucleation by particles immersed in supercooled cloud droplets,” *Chemical Society Reviews*, vol. 41, no. 19, pp. 6519–6554, 2012.
- [39] G. Vali, “-ice nucleationa review,” in *Nucleation and Atmospheric Aerosols*, pp. 271–279, Elsevier, 1996.
- [40] C. S. Zender, R. Miller, and I. Tegen, “Quantifying mineral dust mass budgets: Terminology, constraints, and current estimates,” *Eos, Transactions American Geophysical Union*, vol. 85, no. 48, pp. 509–512, 2004.
- [41] J. D. Atkinson, B. J. Murray, M. T. Woodhouse, T. F. Whale, K. J. Baustian, K. S. Carslaw, S. Dobbie, D. Osullivan, and T. L. Malkin, “The importance of feldspar for ice nucleation by mineral dust in mixed-phase clouds,” *Nature*, vol. 498, no. 7454, p. 355, 2013.
- [42] C. Morris, D. Georgakopoulos, and D. Sands, “Ice nucleation active bacteria and their potential role in precipitation,” in *Journal de Physique IV (Proceedings)*, vol. 121, pp. 87–103, 2004.

- [43] N. Fukuta and B. Mason, “Epitaxial growth of ice on organic crystals,” *Journal of Physics and Chemistry of Solids*, vol. 24, no. 6, pp. 715–718, 1963.
- [44] G. M. McFarquhar and A. J. Heymsfield, “Parameterization of tropical cirrus ice crystal size distributions and implications for radiative transfer: Results from cepex,” *Journal of the atmospheric sciences*, vol. 54, no. 17, pp. 2187–2200, 1997.
- [45] G. M. McFarquhar, A. J. Heymsfield, J. Spinhirne, and B. Hart, “Thin and subvisual tropopause tropical cirrus: Observations and radiative impacts,” *Journal of the atmospheric sciences*, vol. 57, no. 12, pp. 1841–1853, 2000.
- [46] D. K. Lynch, K. Sassen, D. O. Starr, and G. Stephens, *Cirrus*. Oxford University Press, 2002.
- [47] Y. Furukawa, “Snow and ice crystal growth,” in *Handbook of Crystal Growth (Second Edition)*, pp. 1061–1112, Elsevier, 2015.
- [48] T. Kobayashi, “The growth of snow crystals at low supersaturations,” *Philosophical Magazine*, vol. 6, no. 71, pp. 1363–1370, 1961.
- [49] M. P. Bailey and J. Hallett, “A comprehensive habit diagram for atmospheric ice crystals: Confirmation from the laboratory, aircraft, and other field studies,” *Journal of the Atmospheric Sciences*, vol. 66, no. 9, pp. 2888–2899, 2009.
- [50] C. Magono, W. Chung, *et al.*, “Meteorological classification of natural snow crystals,” *Journal of the Faculty of Science, Hokkaido University. Series 7, Geophysics*, vol. 2, no. 4, pp. 321–335, 1966.

- [51] K. Kikuchi, T. Kameda, K. Higuchi, and A. Yamashita, “A global classification of snow crystals, ice crystals, and solid precipitation based on observations from middle latitudes to polar regions,” *Atmospheric research*, vol. 132, pp. 460–472, 2013.
- [52] A. J. Heymsfield, K. M. Miller, and J. D. Spinhirne, “The 27-28 october 1986 fire igo cirrus case study: Cloud microstructure,” *Monthly weather review*, vol. 118, no. 11, pp. 2313–2328, 1990.
- [53] A. Macke, “Scattering of light by polyhedral ice crystals,” *Applied Optics*, vol. 32, no. 15, pp. 2780–2788, 1993.
- [54] FIRE, “Feature on the first isccp regional experiment (fire),” vol. 118(x), (Mon), *Weather Rev*, 1990.
- [55] C. Krupp, “Holographische messungen an eiskristallen in cirruswolken während ice,” *Mater Thesis: Institute for Geophysics, University of Cologne, Germany*, 1991.
- [56] J. Edwards, S. Havemann, J.-C. Thelen, and A. Baran, “A new parametrization for the radiative properties of ice crystals: Comparison with existing schemes and impact in a gcm,” *Atmospheric research*, vol. 83, no. 1, pp. 19–35, 2007.
- [57] G. Mie, “Beiträge zur optik trüber medien, speziell kolloidaler metallösungen,” *Annalen der physik*, vol. 330, no. 3, pp. 377–445, 1908.
- [58] A. Macke, P. N. Francis, G. M. McFarquhar, and S. Kinne, “The role of ice particle shapes and size distributions in the single scattering properties of cirrus clouds,” *Journal of the atmospheric sciences*, vol. 55, no. 17, pp. 2874–2883, 1998.

- [59] G. W. Petty, *A first course in atmospheric radiation*. Sundog Pub, 2006.
- [60] P. Yang and K. Liou, “Single-scattering properties of complex ice crystals in terrestrial atmosphere,” *Beitrage zur Physik der Atmosphere-Contributions to Atmospheric Physics*, vol. 71, no. 2, pp. 223–248, 1998.
- [61] L. C-Labonnote, G. Brogniez, J.-C. Buriez, M. Doutriaux-Boucher, J.-F. Gayet, and A. Macke, “Polarized light scattering by inhomogeneous hexagonal monocrystals: Validation with adeos-polder measurements,” *Journal of Geophysical Research: Atmospheres*, vol. 106, no. D11, pp. 12139–12153, 2001.
- [62] A. J. Baran, R. Cotton, K. Furtado, S. Havemann, L.-C. Labonnote, F. Marengo, A. Smith, and J.-C. Thelen, “A self-consistent scattering model for cirrus. ii: The high and low frequencies,” *Quarterly Journal of the Royal Meteorological Society*, vol. 140, no. 680, pp. 1039–1057, 2014.
- [63] A. Macke, J. Mueller, and E. Raschke, “Single scattering properties of atmospheric ice crystals,” *Journal of the Atmospheric Sciences*, vol. 53, no. 19, pp. 2813–2825, 1996.
- [64] K.-N. Liou, “Influence of cirrus clouds on weather and climate processes: A global perspective,” *Monthly Weather Review*, vol. 114, no. 6, pp. 1167–1199, 1986.
- [65] G. L. Stephens, S.-C. Tsay, P. W. Stackhouse Jr, and P. J. Flatau, “The relevance of the microphysical and radiative properties of cirrus clouds to climate and climatic feedback,” *Journal of the atmospheric sciences*, vol. 47, no. 14, pp. 1742–1754, 1990.

- [66] Q. Fu and K. N. Liou, "Parameterization of the radiative properties of cirrus clouds," *Journal of the Atmospheric Sciences*, vol. 50, no. 13, pp. 2008–2025, 1993.
- [67] E. Raschke, J. Schmetz, and J. Heintzenberg, "The international cirrus experiment (ice). a joint european effort," *ESA Journal*, vol. 14, no. 2, pp. 193–199, 1990.
- [68] A. Ansmann, U. Wandinger, M. Riebesell, C. Weitkamp, and W. Michaelis, "Independent measurement of extinction and backscatter profiles in cirrus clouds by using a combined raman elastic-backscatter lidar," *Applied Optics*, vol. 31, no. 33, pp. 7113–7131, 1992.
- [69] A. Macke, J. Mueller, and E. Raschke, "Single scattering properties of atmospheric ice crystals," *Journal of the Atmospheric Sciences*, vol. 53, no. 19, pp. 2813–2825, 1996.
- [70] K.-N. Liou, "Radiation and cloud processes in the atmosphere. theory, observation, and modeling," *Oxford Monographs on Geology and Geophysics*, 1992.
- [71] R. F. Coleman and K.-N. Liou, "Light scattering by hexagonal ice crystals," *Journal of the Atmospheric Sciences*, vol. 38, no. 6, pp. 1260–1271, 1981.
- [72] Y. Takano and K.-N. Liou, "Solar radiative transfer in cirrus clouds. part i: Single-scattering and optical properties of hexagonal ice crystals," *Journal of the Atmospheric Sciences*, vol. 46, no. 1, pp. 3–19, 1989.
- [73] K.-D. Rockwitz, "Scattering properties of horizontally oriented ice crystal columns in cirrus clouds. part 1," *Applied optics*, vol. 28, no. 19, pp. 4103–4110, 1989.

- [74] M. I. Mishchenko, N. T. Zakharova, N. G. Khlebtsov, T. Wriedt, and G. Videen, “Comprehensive thematic t-matrix reference database: a 2013–2014 update,” *Journal of Quantitative Spectroscopy and Radiative Transfer*, vol. 146, pp. 349–354, 2014.
- [75] P. Yang and K. Liou, “Geometric-optics–integral-equation method for light scattering by nonspherical ice crystals,” *Applied Optics*, vol. 35, no. 33, pp. 6568–6584, 1996.
- [76] M. A. Yurkin and A. G. Hoekstra, “The discrete dipole approximation: an overview and recent developments,” *Journal of Quantitative Spectroscopy and Radiative Transfer*, vol. 106, no. 1-3, pp. 558–589, 2007.
- [77] E. Hesse and Z. Ulanowski, “Scattering from long prisms computed using ray tracing combined with diffraction on facets,” *Journal of Quantitative Spectroscopy and Radiative Transfer*, 2003.
- [78] L. Bi, P. Yang, G. W. Kattawar, Y. Hu, and B. A. Baum, “Scattering and absorption of light by ice particles: solution by a new physical-geometric optics hybrid method,” *Journal of Quantitative Spectroscopy and Radiative Transfer*, vol. 112, no. 9, pp. 1492–1508, 2011.
- [79] K. Muinonen, “Scattering of light by crystals: a modified kirchhoff approximation,” *Applied optics*, vol. 28, no. 15, pp. 3044–3050, 1989.
- [80] A. H. Sihvola, *Electromagnetic mixing formulas and applications*. No. 47 in *Electromagnetic Waves*, Institution of Engineering and Technology, 1999.
- [81] V. Ramanathan and W. Collins, “Thermodynamic regulation of ocean warming

- by cirrus clouds deduced from observations of the 1987 el nino,” *Nature*, vol. 351, no. 6321, p. 27, 1991.
- [82] H. Sandhu and G. Friedmann, “Refractive index of ice,” *American Journal of Physics*, vol. 33, no. 1, pp. 62–62, 1965.
- [83] M. N. Sadiku, “Refractive index of snow at microwave frequencies,” *Applied optics*, vol. 24, no. 4, pp. 572–575, 1985.
- [84] E. R. Pounder, *The physics of ice*. Elsevier, 2013.
- [85] P. V. Hobbs, *Ice physics*. Oxford university press, 2010.
- [86] P. S. Ray, “Broadband complex refractive indices of ice and water,” *Applied Optics*, vol. 11, no. 8, pp. 1836–1844, 1972.
- [87] K. S. Cole and R. H. Cole, “Dispersion and absorption in dielectrics i. alternating current characteristics,” *The Journal of chemical physics*, vol. 9, no. 4, pp. 341–351, 1941.
- [88] C. Zhang, K.-S. Lee, X. Zhang, X. Wei, and Y. Shen, “Optical constants of ice ih crystal at terahertz frequencies,” *Applied Physics Letters*, vol. 79, no. 4, pp. 491–493, 2001.
- [89] T. Matsuoka, S. Fujita, and S. Mae, “Effect of temperature on dielectric properties of ice in the range 5–39 ghz,” *Journal of Applied Physics*, vol. 80, no. 10, pp. 5884–5890, 1996.

- [90] A. H. Sihvola, “How strict are theoretical bounds for dielectric properties of mixtures?,” *IEEE transactions on geoscience and remote sensing*, vol. 40, no. 4, pp. 880–886, 2002.
- [91] F. A. Jenkins, “Harvey e. white, fundamentals of optics,” 1957.
- [92] E. W. Weisstein, “Fraunhofer, joseph von,” tech. rep., Wolfram Research, <http://scienceworld.wolfram.com/biography/Fraunhofer.html>, 2010.
- [93] W.-C. Wang, *Electromagnetic wave theory*. Wiley, New York, 1986.
- [94] O. S. Heavens and R. W. Ditchburn, *Insight into optics*. Wiley Chichester, West Sussex,, England, 1991.
- [95] E. Hecht, *Optics. Pearson Education*. No. 448, Addison-Wesley, 2002.
- [96] E. Hecht, *Optics. Pearson Education*. No. 529, Addison-Wesley, 2002.
- [97] E. Hecht, *Optics. Pearson Education*. No. 540, Addison-Wesley, 2002.
- [98] M. Abramowitz and I. A. Stegun, *Handbook of mathematical functions: with formulas, graphs, and mathematical tables*. No. 55, Courier Corporation, 1964.
- [99] Hyperphysics, “Fraunhofer single-slit diffraction,” 2017, available at: <http://hyperphysics.phy-astr.gsu.edu/hbase/phyopt/sinslit.html>.
- [100] C. A. Bennett, *Principles of physical optics*. Wiley, 2008.

- [101] M. Born, E. Wolf, A. B. Bhatia, P. Clemmow, *et al.*, *Principles of optics: electromagnetic theory of propagation, interference and diffraction of light*, vol. 4. Pergamon press Oxford, 1970.
- [102] G. Riccio, *Uniform asymptotic physical optics solutions for a set of diffraction problems*. INTECH Open Access Publisher, 2010.
- [103] P. S. Kumar and G. Ranganath, “Geometrical theory of diffraction,” *Pramana*, vol. 37, no. 6, pp. 457–488, 1991.
- [104] R. G. Kouyoumjian and P. H. Pathak, “A uniform geometrical theory of diffraction for an edge in a perfectly conducting surface,” *Proceedings of the IEEE*, vol. 62, no. 11, pp. 1448–1461, 1974.
- [105] R. Paknys, “Uniform theory of diffraction,” *Applied Frequency-Domain Electromagnetics*, pp. 268–316, 2016.
- [106] G. L. James, *Geometrical theory of diffraction for electromagnetic waves*. No. 1, IET, 1986.
- [107] W. D. Burnside and K. W. Burgener, “High frequency scattering by a thin lossless dielectric slab,” *IEEE Transactions on Antennas and Propagation*, vol. 31, pp. 104–110, 1983.
- [108] P. R. Rousseau and P. H. Pathak, “Time-domain uniform geometrical theory of diffraction for a curved wedge,” *IEEE Transactions on Antennas and Propagation*, vol. 43, no. 12, pp. 1375–1382, 1995.

- [109] P. Y. Ufimtsev, *Fundamentals of the physical theory of diffraction*. John Wiley & Sons, 2014.
- [110] T. Shijo, L. Rodriguez, and M. Ando, “The modified surface-normal vectors in the physical optics,” *IEEE Transactions on Antennas and Propagation*, vol. 56, no. 12, pp. 3714–3722, 2008.
- [111] Y. Z. Umul, “Modified theory of physical optics,” *Optics Express*, vol. 12, no. 20, pp. 4959–4972, 2004.
- [112] R. F. Harrington, *Time-harmonic electromagnetic fields*. McGraw-Hill, 1961.
- [113] C. Gennarelli, G. Riccio, and G. Pelosi, “Approximate diffraction coefficients for an anisotropic impedance wedge,” *Electromagnetics*, vol. 21, no. 2, pp. 165–180, 2001.
- [114] C. Gennarelli, G. Pelosi, C. Pochini, and G. Riccio, “Uniform asymptotic po diffraction coefficients for an anisotropic impedance half-plane,” *Journal of electromagnetic waves and applications*, vol. 13, no. 7, pp. 963–980, 1999.
- [115] C. Gennarelli, G. Pelosi, G. Riccio, and G. Toso, “Electromagnetic scattering by nonplanar junctions of resistive sheets,” *IEEE Transactions on Antennas and Propagation*, vol. 48, no. 4, pp. 574–580, 2000.
- [116] C. Gennarelli, G. Pelosi, G. Riccio, and G. Toso, “Diffraction by an anisotropic dielectric half-plane: a uniform asymptotic po solution,” *IEEE Transactions on Antennas and Propagation*, vol. 49, no. 12, pp. 1624–1627, 2001.

- [117] A. Petrin, *Wave Propagation in Materials for Modern Applications*. BoD–Books on Demand, 2010.
- [118] G. Gennarelli and G. Riccio, “Time domain diffraction by a right-angled penetrable wedge,” *IEEE Transactions on Antennas and Propagation*, vol. 60, no. 6, pp. 2829–2833, 2012.
- [119] S.-W. Lee and G. Deschamps, “A uniform asymptotic theory of electromagnetic diffraction by a curved wedge,” *IEEE transactions on antennas and propagation*, vol. 24, no. 1, pp. 25–34, 1976.
- [120] G. Gennarelli and G. Riccio, “Plane-wave diffraction by an obtuse-angled dielectric wedge,” *JOSA A*, vol. 28, no. 4, pp. 627–632, 2011.
- [121] G. Gennarelli, M. Frongillo, and G. Riccio, “High-frequency evaluation of the field inside and outside an acute-angled dielectric wedge,” *IEEE Transactions on Antennas and Propagation*, vol. 63, no. 1, pp. 374–378, 2015.
- [122] J. Richmond, “A reaction theorem and its application to antenna impedance calculations,” *IRE Transactions on Antennas and Propagation*, vol. 9, no. 6, pp. 515–520, 1961.
- [123] A. F. Peterson, S. L. Ray, R. Mittra, I. of Electrical, and E. Engineers, *Computational methods for electromagnetics*. IEEE press New York, 1998.
- [124] J. R. Carson, “Reciprocal theorems in radio communication,” *Proceedings of the Institute of Radio Engineers*, vol. 17, no. 6, pp. 952–956, 1929.

- [125] C. Krowne, “Electromagnetic theorems for complex anisotropic media,” *IEEE transactions on antennas and propagation*, vol. 32, no. 11, pp. 1224–1230, 1984.
- [126] D. Bebbington, “Draft research note of scattering by a transparent wedge,” *University of Essex*, 2016.
- [127] P. C. Chang, J. Walker, and K. Hopcraft, “Ray tracing in absorbing media,” *Journal of Quantitative Spectroscopy and Radiative Transfer*, vol. 96, no. 3, pp. 327–341, 2005.
- [128] M. Abramowitz and I. A. Stegun, *Handbook of mathematical functions: with formulas, graphs, and mathematical tables*, vol. 55. Courier Corporation, 1964.
- [129] B. G. Korenev, *Bessel functions and their applications*. CRC Press, 2003.
- [130] R. Snieder, “Extracting the greens function from the correlation of coda waves: A derivation based on stationary phase,” *Physical Review E*, vol. 69, no. 4, p. 046610, 2004.
- [131] K. Dinesh, *The Pearson Guide To Complete Mathematics For The Aieee, 4/E*. Pearson Education India, 2010.
- [132] A. W. Paeth, “A fast algorithm for general raster rotation,” in *Graphics Interface*, vol. 86, 1986.
- [133] A. W. Lohmann, “Image rotation, wigner rotation, and the fractional fourier transform,” *Journal of the Optical Society of America A*, vol. 10, no. 10, pp. 2181–2186, 1993.

- [134] C. A. Balanis, *Advanced engineering electromagnetics*. John Wiley & Sons, 1999.
- [135] R. F. Harrington, *Field computation by moment methods*. Wiley-IEEE Press, 1993.
- [136] U. Jakobus and F. M. Landstorfer, “Improvement of the po-mom hybrid method by accounting for effects of perfectly conducting wedges,” *IEEE Transactions on Antennas and Propagation*, vol. 43, no. 10, pp. 1123–1129, 1995.
- [137] J.-M. Jin, F. Ling, S. T. Carolan, J. M. Song, W. C. Gibson, W. C. Chew, C.-C. Lu, and R. Kipp, “A hybrid sbr/mom technique for analysis of scattering from small protrusions on a large conducting body,” *IEEE Transactions on Antennas and Propagation*, vol. 46, no. 9, pp. 1349–1357, 1998.
- [138] Ö. A. Çivi, P. H. Pathak, H.-T. Chou, and P. Nepa, “A hybrid uniform geometrical theory of diffraction–moment method for efficient analysis of electromagnetic radiation/scattering from large finite planar arrays,” *Radio Science*, vol. 35, no. 2, pp. 607–620, 2000.
- [139] S. Jamsa, J. Peltoniemi, and K. Lumme, “Thermal emission from a rough surface: ray optics approach,” *Astronomy and Astrophysics*, vol. 271, p. 319, 1993.

8 — Appendices

8.1 Rotational matrix facet construction

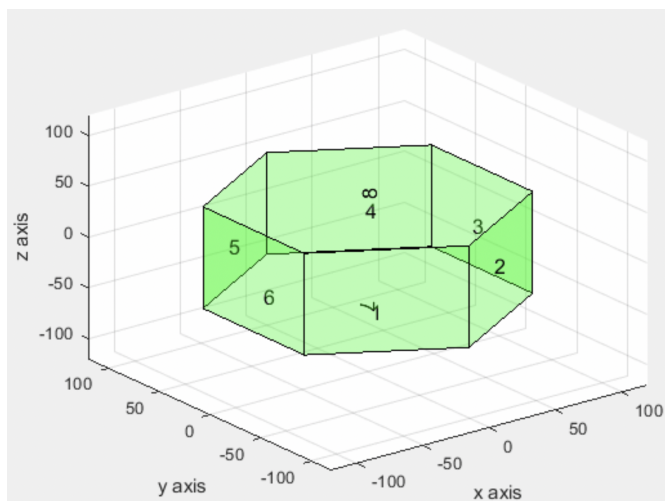


Figure 8.1: labelling the facets of the hexagonal prism shape

For the hexagonal prism shape, the rotation matrix for each plane are as follows:

Plane 1

$$R = \begin{bmatrix} -0.5 & 0.87 & 0 \\ -0.87 & -0.5 & 0 \\ 0 & 0 & 1 \end{bmatrix} \quad (8.1)$$

Original points:

Vertices=[p1,p2,p3,p4]

P1=(0.87,0.5,-0.5) P2=(0.87,0.5,0.5) P3=(0.87,-0.5,0.5) P4=(0.87,-0.5,-0.5)

Points after rotation

Vertices=[p1,p2,p3,p4]

P1=(-0.87,-0.5,-0.5) P2=(-0.87,-0.5,0.5) P3=(0,-1,0.5) P4=(0,-1,-0.5)

Plane 2

$$R = \begin{bmatrix} 0.5 & 0.87 & 0 \\ -0.87 & 0.5 & 0 \\ 0 & 0 & 1 \end{bmatrix} \quad (8.2)$$

Original points:

Vertices=[p1,p2,p3,p4]

P1=(0.87,0.5,-0.5) P2=(0.87,0.5,0.5) P3=(0.87,-0.5,0.5) P4=(0.87,-0.5,-0.5)

Points after rotation

Vertices=[p1,p2,p3,p4]

P1=(0,-1,0.5) P2=(0,-1,-0.5) P3=(0.87,-0.5,0.5) P4=(0.87,-0.5,-0.5)

Plane 3

$$R = \begin{bmatrix} 1 & 0 & 0 \\ 0 & 1 & 0 \\ 0 & 0 & 1 \end{bmatrix} \quad (8.3)$$

Original points:

Vertices=[p1,p2,p3,p4]

P1=(0.87,0.5,-0.5) P2=(0.87,0.5,0.5) P3=(0.87,-0.5,0.5) P4=(0.87,-0.5,-0.5) Points after rotation

Vertices=[p1,p2,p3,p4]

P1=(0.87,0.5,-0.5) P2=(0.87,0.5,0.5) P3=(0.87,-0.5,0.5) P4=(0.87,-0.5,-0.5)

Plane 4

$$R = \begin{bmatrix} 0.5 & -0.87 & 0 \\ 0.87 & 0.5 & 0 \\ 0 & 0 & 1 \end{bmatrix} \quad (8.4)$$

Original points:

Vertices=[p1,p2,p3,p4]

P1=(0.87,0.5,-0.5) P2=(0.87,0.5,0.5) P3=(0.87,-0.5,0.5) P4=(0.87,-0.5,-0.5)

Points after rotation

Vertices=[p1,p2,p3,p4]

P1=(0.87,0.5,-0.5) P2=(0.87,0.5,0.5) P3=(0,1,0.5) P4=(0,1,-0.5)

Plane 5

$$R = \begin{bmatrix} -0.5 & -0.87 & 0 \\ 0.87 & -0.5 & 0 \\ 0 & 0 & 1 \end{bmatrix} \quad (8.5)$$

Original points:

Vertices=[p1,p2,p3,p4]

P1=(0.87,0.5,-0.5) P2=(0.87,0.5,0.5) P3=(0.87,-0.5,0.5) P4=(0.87,-0.5,-0.5)

Points after rotation

Vertices=[p1,p2,p3,p4]

P1=(-0.87,0.5,-0.5) P2=(-0.87,0.5,0.5) P3=(0,1,0.5) P4=(0,1,-0.5)

Plane 6

$$R = \begin{bmatrix} -1 & 0 & 0 \\ 0 & -1 & 0 \\ 0 & 0 & 1 \end{bmatrix} \quad (8.6)$$

Original points:

Vertices=[p1,p2,p3,p4]

P1=(0.87,0.5,-0.5) P2=(0.87,0.5,0.5) P3=(0.87,-0.5,0.5) P4=(0.87,-0.5,-0.5)

Point after rotation

Vertices =[p1,p2,p3,p4]

$$P1=(-0.87,-0.5,-0.5) \quad P2=(-0.87,-0.5,0.5) \quad P3=(-0.87,0.5,-0.5) \quad P4=(-0.87,0.5,0.5)$$

Plane 7

$$R = \begin{bmatrix} 1 & 0 & 0 \\ 0 & 1 & 0 \\ 0 & 0 & 1 \end{bmatrix} \quad (8.7)$$

Original points:

$$\text{Vertices} = [p1, p2, p3, p4, p5, p6]$$

$$P1=(-0.87,-0.5,-0.5) \quad P2=(0,-1,-0.5) \quad P3=(0.87,0.5,-0.5) \quad P4=(0.87,-0.5,-0.5)$$

$$P5=(-0.87,0.5,-0.5) \quad P6=(0,1,-0.5)$$

Point after rotation

$$\text{Vertices} = [p1, p2, p3, p4, p5, p6]$$

$$P1=(-0.87,-0.5,-0.5) \quad P2=(0,-1,-0.5) \quad P3=(0.87,0.5,-0.5) \quad P4=(0.87,-0.5,-0.5)$$

$$P5=(-0.87,0.5,-0.5) \quad P6=(0,1,-0.5)$$

Plane 8

$$R = \begin{bmatrix} 1 & 0 & 0 \\ 0 & -1 & 0 \\ 0 & 0 & -1 \end{bmatrix} \quad (8.8)$$

Original points:

$$\text{Vertices} = [p1, p2, p3, p4, p5, p6]$$

$P1=(-0.87,-0.5,-0.5)$ $P2=(0,-1,-0.5)$ $P3=(0.87,0.5,-0.5)$ $P4=(0.87,-0.5,-0.5)$ $P5=(-0.87,0.5,-0.5)$ $P6=(0,1,-0.5)$

Points after rotation:

Vertexes=[p1,p2,p3,p4,p5,p6]

$P1=(-0.87,-0.5,0.5)$ $P2=(0,-1,0.5)$ $P3=(0.87,0.5,0.5)$ $P4=(0.87,-0.5,0.5)$

$P5=(-0.87,0.5,0.5)$ $P6=(0,1,0.5)$

Similarly, when the prism shape is considered as can be seen from the figure below,

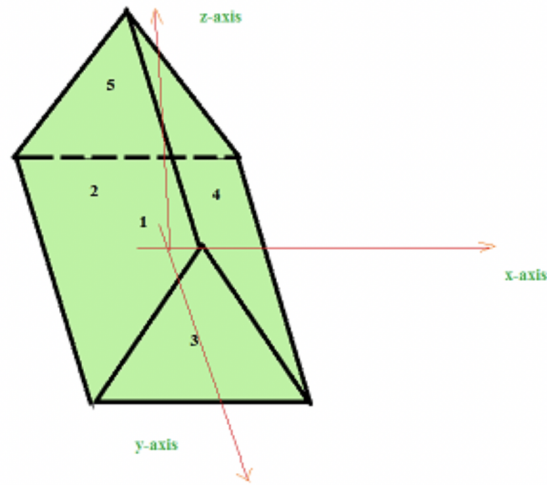


Figure 8.2: Triangular prism facets

In this shape, the normal vector was set for each plane as a rotation axis vector. When the rotation axis is a normal vector of it's plane, then the rotation angles can be set as zero. The coordinates axis and original points are the same as in the figure above. The rotation matrices for the prism shape were found as follows,

Plane 1 (rotation axis is y-axis)

$$R = \begin{bmatrix} 1 & 0 & 0 \\ 0 & 1 & 0 \\ 0 & 0 & 1 \end{bmatrix} \quad (8.9)$$

Original points:

Vertices =[p1,p2,p3,p4]

P1=(1,1,0) P2=(1,-1,0) P3=(-1,-1,0) P4=(-1,1,0)

Point after rotation

Vertices =[p1,p2,p3,p4]

P1=(1,1,0) P2=(1,-1,0) P3=(-1,-1,0) P4=(-1,1,0)

Plane 2

$$R = \begin{bmatrix} -0.71 & 0 & 0.71 \\ 0 & 1 & 0 \\ -0.71 & 0 & -0.71 \end{bmatrix} \quad (8.10)$$

Original points:

Vertices =[p1,p2,p3,p4]

P1=(0.71,1,0.71) P2=(0.5,1,-0.5) P3=(0.5,-1,-0.5) P4=(0.71,-1,0.71)

Point after rotation

Vertices =[p1,p2,p3,p4]

$$P1=(-1,1,0) \quad P2=(0,1,0.71) \quad P3=(0,-1,0.71) \quad P4=(-1,-1,0)$$

Plane 3 (rotation axis is z-axis)

$$R = \begin{bmatrix} 1 & 0 & 0 \\ 0 & 1 & 0 \\ 0 & 0 & 1 \end{bmatrix} \quad (8.11)$$

Original points:

$$\text{Vertices} = [p1, p2, p3]$$

$$P1=(-1,1,0) \quad P2=(1,1,0) \quad P3=(0,1,0.71)$$

Point after rotation

$$\text{Vertices} = [p1, p2, p3]$$

$$P1=(-1,1,0) \quad P2=(1,1,0) \quad P3=(0,1,0.71)$$

Plane 4 (rotation axis is y-axis)

$$R = \begin{bmatrix} -0.71 & 0 & -0.71 \\ 0 & 1 & 0 \\ 0.71 & 0 & -0.71 \end{bmatrix} \quad (8.12)$$

Original points:

$$\text{Vertices} = [p1, p2, p3, p4]$$

$$P1=(-0.71,1,-0.71) \quad P2=(0.5,1,-0.5) \quad P3=(0.5,-1,-0.5) \quad P4=(-0.71,-1,-0.71)$$

Point after rotation

Vertices =[p1,p2,p3,p4]

P1=(1,1,0) P2=(1,-1,0) P3=(0,-1,0.71) P4=(0,1,0.71)

Plane 5 (rotation axis is z-axis)

$$R = \begin{bmatrix} -1 & 0 & 0 \\ 0 & -1 & 0 \\ 0 & 0 & 1 \end{bmatrix} \quad (8.13)$$

Original points:

Vertices =[p1,p2,p3]

P1=(-1,1,0) P2=(1,1,0) P3=(0,1,0.71)

Point after rotation

Vertices =[p1,p2,p3]

P1=(1,-1,0) P2=(-1,-1,0) P3=(0,-1,0.71)

Then, for the bullet shape as can be seen in the figure below.

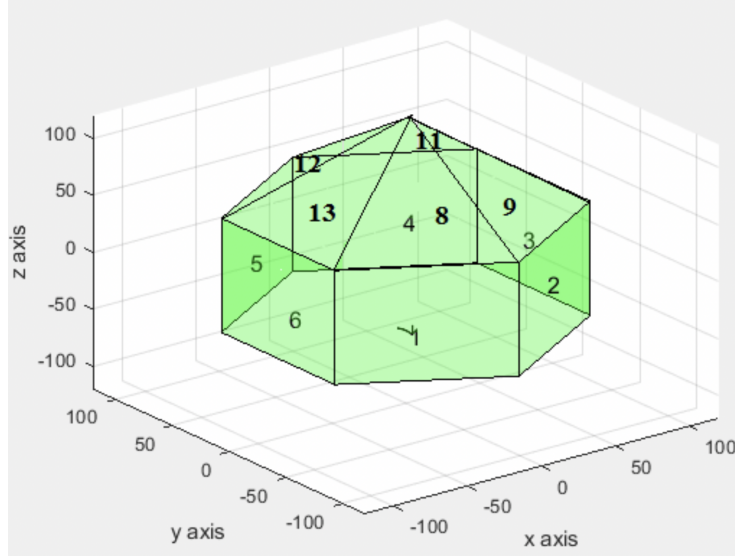


Figure 8.3: Labelling bullet crystals facets

In this shape, the rotation matrices are the same as for the hexagonal prism shape for planes 1 to 8. For planes 8 to 13, the normal vector for each plane was set as a rotation matrix. Therefore, the rotation matrix of each plane and vertices were found as follows.

Plane 1

$$R = \begin{bmatrix} -0.5 & 0.87 & 0 \\ -0.87 & -0.5 & 0 \\ 0 & 0 & 1 \end{bmatrix} \quad (8.14)$$

Original points:

Vertices=[p1,p2,p3,p4]

P1=(0.87,0.5,-0.5) P2=(0.87,0.5,0.5) P3=(0.87,-0.5,0.5) P4=(0.87,-0.5,-0.5)

Point after rotation

Vertices=[p1,p2,p3,p4]

P1=(-0.87,-0.5,-0.5) P2=(-0.87,-0.5,0.5) P3=(0,-1,0.5) P4=(0,-1,-0.5)

Plane 2

$$R = \begin{bmatrix} 0.5 & 0.87 & 0 \\ -0.87 & 0.5 & 0 \\ 0 & 0 & 1 \end{bmatrix} \quad (8.15)$$

Original points:

Vertices=[p1,p2,p3,p4]

P1=(0.87,0.5,-0.5) P2=(0.87,0.5,0.5) P3=(0.87,-0.5,0.5) P4=(0.87,-0.5,-0.5)

Point after rotation

Vertices=[p1,p2,p3,p4]

P1=(0,-1,0.5) P2=(0,-1,-0.5) P3=(0.87,-0.5,0.5) P4=(0.87,-0.5,-0.5)

Plane 3

$$R = \begin{bmatrix} 1 & 0 & 0 \\ 0 & 1 & 0 \\ 0 & 0 & 1 \end{bmatrix} \quad (8.16)$$

Original points:

Vertices=[p1,p2,p3,p4]

P1=(0.87,0.5,-0.5) P2=(0.87,0.5,0.5) P3=(0.87,-0.5,0.5) P4=(0.87,-0.5,-0.5)

Point after rotation

Vertices=[p1,p2,p3,p4]

P1=(0.87,0.5,-0.5) P2=(0.87,0.5,0.5) P3=(0.87,-0.5,0.5) P4=(0.87,-0.5,-0.5)

Plane 4

$$R = \begin{bmatrix} 0.5 & -0.87 & 0 \\ 0.87 & 0.5 & 0 \\ 0 & 0 & 1 \end{bmatrix} \quad (8.17)$$

Original points:

Vertices=[p1,p2,p3,p4]

P1=(0.87,0.5,-0.5) P2=(0.87,0.5,0.5) P3=(0.87,-0.5,0.5) P4=(0.87,-0.5,-0.5)

Point after rotation

Vertices=[p1,p2,p3,p4]

P1=(0.87,0.5,-0.5) P2=(0.87,0.5,0.5) P3=(0,1,0.5) P4=(0,1,-0.5)

Plane 5

$$R = \begin{bmatrix} -0.5 & -0.87 & 0 \\ 0.87 & -0.5 & 0 \\ 0 & 0 & 1 \end{bmatrix} \quad (8.18)$$

Original points:

Vertices=[p1,p2,p3,p4]

$$P1=(0.87,0.5,-0.5) \quad P2=(0.87,0.5,0.5) \quad P3=(0.87,-0.5,0.5) \quad P4=(0.87,-0.5,-0.5)$$

Point after rotation

$$\text{Vertices}=[p1,p2,p3,p4]$$

$$P1=(-0.87,0.5,-0.5) \quad P2=(-0.87,0.5,0.5) \quad P3=(0,1,0.5) \quad P4=(0,1,-0.5)$$

Plane 6

$$R = \begin{bmatrix} -1 & 0 & 0 \\ 0 & -1 & 0 \\ 0 & 0 & 1 \end{bmatrix} \quad (8.19)$$

Original points:

$$\text{Vertices}=[p1,p2,p3,p4]$$

$$P1=(0.87,0.5,-0.5) \quad P2=(0.87,0.5,0.5) \quad P3=(0.87,-0.5,0.5) \quad P4=(0.87,-0.5,-0.5)$$

Point after rotation

$$\text{Vertices}=[p1,p2,p3,p4]$$

$$P1=(-0.87,-0.5,-0.5) \quad P2=(-0.87,-0.5,0.5) \quad P3=(-0.87,0.5,-0.5) \quad P4=(-0.87,0.5,0.5)$$

Plane 7

$$R = \begin{bmatrix} 1 & 0 & 0 \\ 0 & 1 & 0 \\ 0 & 0 & 1 \end{bmatrix} \quad (8.20)$$

Original points:

Vertices =[p1,p2,p3,p4,p5,p6]

P1=(-0.87,-0.5,-0.5) P2=(0,-1,-0.5) P3=(0.87,0.5,-0.5) P4=(0.87,-0.5,-0.5)

P5=(-0.87,0.5,-0.5) P6=(0,1,-0.5)

Point after rotation

Vertices =[p1,p2,p3,p4,p5,p6]

P1=(-0.87,-0.5,-0.5) P2=(0,-1,-0.5) P3=(0.87,0.5,-0.5) P4=(0.87,-0.5,-0.5)

P5=(-0.87,0.5,-0.5) P6=(0,1,-0.5)

Plane 8 (rotation axis is z-axis)

$$R = \begin{bmatrix} 1 & 0 & 0 \\ 0 & 1 & 0 \\ 0 & 0 & 1 \end{bmatrix} \quad (8.21)$$

Original points:

Vertices =[p1,p2,p3]

P1=(-0.87,-0.5,-0.5) P2=(0,-1,-0.5) P3=(0,0,1.5)

Point after rotation

Vertices =[p1,p2,p3]

P1=(-0.87,-0.5,-0.5) P2=(0,-1,-0.5) P3=(0,0,1.5)

Plane 9 (rotation axis is z-axis angle is 60 degree)

$$R = \begin{bmatrix} 0.5 & -0.87 & 0 \\ 0.87 & 0.5 & 0 \\ 0 & 0 & 1 \end{bmatrix} \quad (8.22)$$

Original points:

Vertices =[p1,p2,p3]

P1=(-0.87,-0.5,-0.5) P2=(0,-1,-0.5) P3=(0,0,1.5)

Point after rotation

Vertices =[p1,p2,p3]

P1=(0.87,-0.5,-0.5) P2=(0,-1,-0.5) P3=(0,0,1.5)

Plane 10 (rotation angle is 120 degree)

$$R = \begin{bmatrix} -0.5 & -0.87 & 0 \\ 0.87 & -0.5 & 0 \\ 0 & 0 & 1 \end{bmatrix} \quad (8.23)$$

Original points:

Vertices =[p1,p2,p3]

P1=(-0.87,-0.5,-0.5) P2=(0,-1,-0.5) P3=(0,0,1.5)

Point after rotation

Vertices =[p1,p2,p3]

P1=(0.87,-0.5,-0.5) P2=(0.87,0.5,-0.5) P3=(0,0,1.5)

Plane 11 (rotation angle is 180 degree)

$$R = \begin{bmatrix} -1 & 0 & 0 \\ 0 & -1 & 0 \\ 0 & 0 & 1 \end{bmatrix} \quad (8.24)$$

Original points:

Vertices =[p1,p2,p3]

P1=(-0.87,-0.5,-0.5) P2=(0,-1,-0.5) P3=(0,0,1.5)

Point after rotation

Vertices =[p1,p2,p3]

P1=(0.87,0.5,-0.5) P2=(0,1,-0.5) P3=(0,0,1.5)

Plane 12 (rotation angle is 240 degree)

$$R = \begin{bmatrix} -0.5 & 0.87 & 0 \\ -0.87 & -0.5 & 0 \\ 0 & 0 & 1 \end{bmatrix} \quad (8.25)$$

Original points:

Vertices =[p1,p2,p3]

P1=(-0.87,-0.5,-0.5) P2=(0,-1,-0.5) P3=(0,0,1.5)

Point after rotation

Vertices =[p1,p2,p3]

P1=(0,1,-0.5) P2=(-0.87,0.5,-0.5) P3=(0,0,1.5)

Plane 13 (rotation angle is 300 degree)

$$R = \begin{bmatrix} 0.5 & 0.87 & 0 \\ -0.87 & 0.5 & 0 \\ 0 & 0 & 1 \end{bmatrix} \quad (8.26)$$

Original points:

Vertices =[p1,p2,p3]

P1=(-0.87,-0.5,-0.5) P2=(0,-1,-0.5) P3=(0,0,1.5)

Point after rotation

Vertices =[p1,p2,p3]

P1=(-0.87,0.5,-0.5) P2=(-0.87,-0.5,-0.5) P3=(0,0,1.5)

8.2 PO results for 3D triangular prism

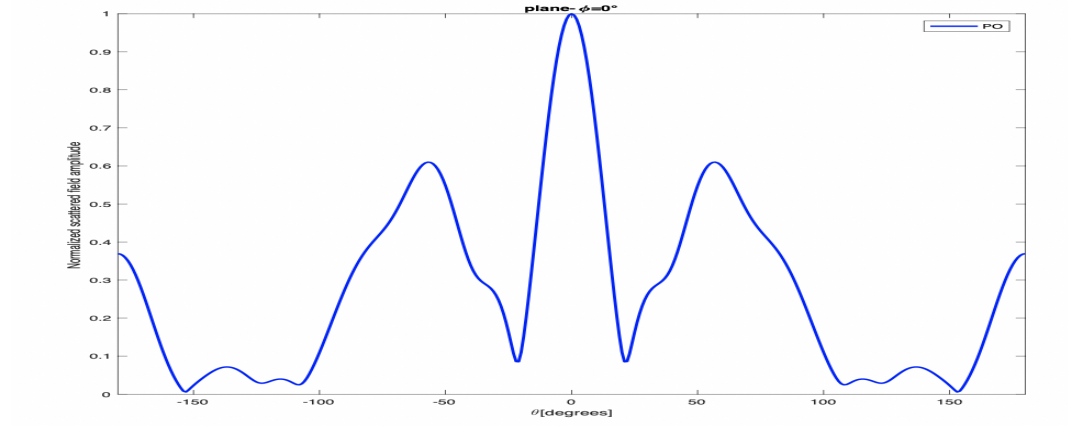


Figure 8.4: Relative amplitude of the scattered field at $\phi = 0^\circ$. Prism parameters: $n=1.787$, $d=10 \mu m$, $h=10 \mu m$, $\lambda = 2 \mu m$, normal incidence

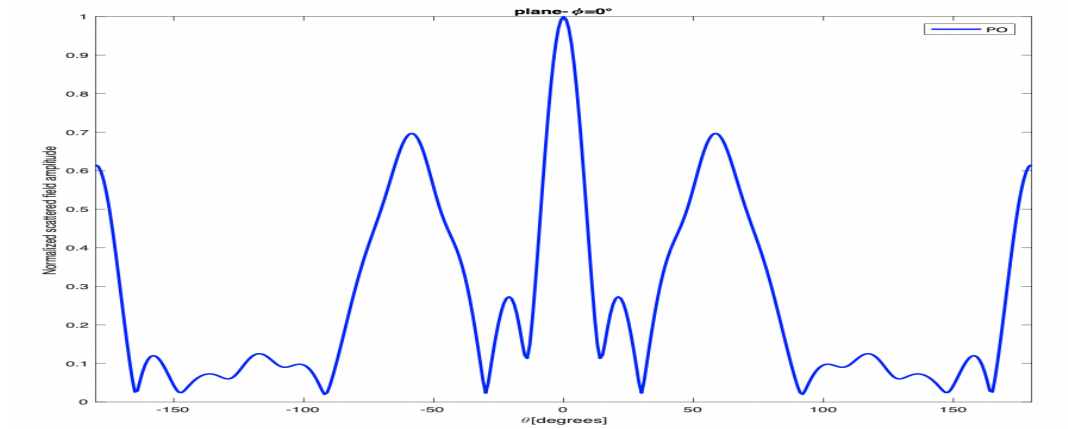


Figure 8.5: Relative amplitude of the scattered field at $\phi = 0^\circ$. Prism parameters: $n=1.787$, $d=15 \mu m$, $h=5 \mu m$, $\lambda = 2 \mu m$, normal incidence

8.3 Publications

Shaker, J. & Bebbington, D. Scatterings of Infrared by Pristine Cloud Ice Crystals , 2016 Progress in Electromagnetic Research Symposium (PIERS), Shanghai.

Shaker, J. & Bebbington, D. Scatterings of Infrared by Prismatic Cloud Ice Crystals 2017 Progress in Electromagnetic Research Symposium (PIERS), Singapore.

Shaker, J. & Bebbington, D. Modelling of Electromagnetic Scattering at Infrared Wavelengths by Pristine Ice Crystals accepted to be submitted to the journal of Electronics and Optoelectronics.